Structural Behavior of Lightweight Concrete Bridge Deck Slabs Reinforced with Basalt FRP Bars

BY

FADI ALSHARIF

B.S., The University of Jordan, Jordan, 2007

THESIS

Submitted as partial fulfillment of the requirements
for the degree of Master of Science in Civil Engineering
in the Graduate College of the
University of Illinois at Chicago, 2014

Chicago, Illinois

Defense Committee:

Mohsen A. Issa, Chair and Advisor
Krishna Reddy
Craig Foster

This thesis is dedicated to my magnificent loving and caring wife,

Isabella, who patiently supported me each step of the way.

A true blessing in my life.

ACKNOWLEDGEMENTS

First and foremost I offer my sincerest gratitude to my advisor and committee chair, Professor Mohsen A. Issa for giving me the opportunity to pursue my graduate studies under his supervision. He has supported me throughout my studies and thesis with his knowledge and patience whilst allowing me the room to work in my own way. I attribute the level of my master's degree to his encouragement and effort, without him this thesis would not have been completed. One simply could not wish for a better supervisor.

I would also like to sincerely thank the other two members of the defense committee, Professor Krishna Reddy and Professor Craig Foster for their support and insightful guidance.

In my daily work I have been blessed with a cheerful group of fellow students, my "labmates" Mustafa Ibrahim, Maen Farhat, Ibrahim Lotfy and Momenur Rahman. Without them, there is no way that I could have gotten through the stress and desperation that graduate studies sometimes entail. Each has done more than I can individually thank them for. Thank you Mustafa and Maen for the late night and weekends hard work, mixed with humor and fun. Thank you Ibrahim for all your help and effort, for without you nothing would have moved from its place! And thank you Momen for your contribution and kind encouragement.

I could not continue this acknowledgement without giving thanks to the immense help of the undergraduate students that offered their support. Thank you Chris Naegele, Steve Kwon and Marcos Alencar. I wish you all the best in your studies and may you have great success in the future.

Last, but definitely not least, I owe so much of my gratitude to my parents and their love. They are the ones who raised me to be the man that I am today. I am also grateful to my sister and younger brother for continuously lifting up my spirits and being there for me. Finally, I thank my eldest brother Hani and uncle Bilal for their endless encouragement and motivation from the very beginning before any of this even began.

Sincerely,
Fadi Alsharif

Table of Contents

Chapter 1: INTRODUCTION **1**
1.1 Background **1**
1.2 Research Significance **3**
1.3 Research Objective **5**
Chapter 2: LITERATURE REVIEW **6**
2.1 FRP Composites **6**
2.2 BFRP Bars **7**
2.2.1 Mechanical Properties 7
2.2.2 Durability Properties 8
2.3 Flexural Behavior and Capacity of BFRP Reinforced Concrete Beams and Slabs **9**
2.4 Serviceability of FRP Reinforced Beams **16**
Chapter 3: EXPERIMENTAL PROGRAM **21**
3.1 Materials **21**
3.1.1 BFRP Reinforcing Bars 21
3.1.2 Lightweight Concrete (LWC) 22
3.2 Fabrication **27**
3.2.1 Formworks 27
3.2.2 Strain Gages 30
3.3 Experimental Parameters **32**
3.4 Experimental Setup **38**
3.4.1 Simply Supported BFRP Reinforced Slabs 38
3.4.2 Two-Span Continuous BFRP Reinforced Slabs 41
Chapter 4: EXPERIMENTAL RESULTS 47
4.1 Simply Supported BFRP Reinforced Slabs **47**
4.2 Two-Span Continuous BFRP Reinforced Slabs **63**
Chapter 5: DISCUSSION AND ANALYSIS **72**
5.1 Simply Supported Slabs **72**
5.1.1 Slabs SS1 and SS2 72
5.1.2 Slabs From Continuous Specimens 75

5.2 Two-Span Continuous Slabs **78**
5.3 Prediction of Ultimate Moment Capacity and Effective Moment of Inertia **80**
5.3.1 Ultimate Moment Capacity 81
5.3.2 Effective Moment of Inertia 83
Chapter 6: FINITE ELEMENT ANALYSIS **90**
6.1 Materials **90**
6.1.1 Concrete 90
6.1.2 BFRP Rebars 91
6.2 Supports and Loading Plates **91**
6.3 Loading and Boundary Conditions **92**
6.4 Finite Element Results **93**
6.4.1 Simply Supported Slabs SS1 and SS2 93
6.4.2 Continuous Slabs CS1 and CS2 98
Chapter 7: Conclusion **103**
References **105**
VITA **109**

LIST OF TABLES

TABLE 3.1. MECHANICAL PROPERTIES OF BFRP BARS 22

TABLE 3.2. MIX PROPORTIONS OF LIGHTWEIGHT CONCRETE 23

TABLE 3.3. COMPRESSIVE, FLEXURAL AND SPLITTING TENSILE STRENGTH OF THE LWC MIX 24

TABLE 3.4. TYPES OF STRAIN GAGES USED IN THE EXPERIMENTAL PROGRAM 32

TABLE 3.5. REINFORCEMENT AND SPAN LENGTH DETAILS FOR BRIDGE DECK SPECIMENS 34

TABLE 3.6. NOMINAL AND ULTIMATE MOMENT CAPACITIES FOR THE SLABS 38

TABLE 5.1 EXPERIMENTAL AND PREDICTED NOMINAL MOMENT CAPACITIES FOR BFRP REINFORCED SLABS 87

LIST OF FIGURES

FIGURE 2.1. STRESS-STRAIN RELATIONSHIP FOR STEEL AND DIFFERENT FRP BARS 7
FIGURE 3.1. CASTING THE CYLINDRICAL AND PRISM SPECIMENS 24
FIGURE 3.2. COMPRESSIVE STRENGTH TEST (ASTM C39) 25
FIGURE 3.3. SPLITTING TENSILE STRENGTH TEST (ASTM C496) 25
FIGURE 3.4. FLEXURAL STRENGTH TEST OF CONCRETE BEAMS (ASTM C78) 26
FIGURE 3.5. MODULUS OF ELASTICITY TEST FIXTURE - ASTM C469 27
FIGURE 3.6 STRESS-STRAIN RELATIONSHIP FOR LWC (ASTM C469) 28
FIGURE 3.7. FINALIZED FORMWORKS FOR SIMPLY SUPPORTED SPECIMENS SS1 AND SS2 29
FIGURE 3.8. FORMWORK FOR 2-SPAN CONTINUOUS SLABS CS1 AND CS2 30
FIGURE 3.9. CASTING OF THE SLABS 31
FIGURE 3.10. INSTALLATION PROCESS OF BFRP STRAIN GAGE 32
FIGURE 3.11. CROSS-SECTION AND DETAILS FOR SPECIMENS SS1 AND SS2 34
FIGURE 3.12. CROSS-SECTION AND DETAILS FOR SPECIMENS CS1, SS3-CS1 AND SS5-CS1 35
FIGURE 3.13. CROSS-SECTION AND DETAILS FOR SPECIMENS CS2, SS4-CS2 AND SS6-CS2 35
FIGURE 3.14. TESTING SETUP FOR SIMPLY SUPPORTED SPECIMENS 39
FIGURE 3.15. LABORATORY SETUP FOR SIMPLY SUPPORTED SLABS 40
FIGURE 3.16. INSTRUMENTS FOR SPECIMENS SS1 AND SS2 41
FIGURE 3.17. INSTRUMENTS FOR SPECIMENS SS3-CS1 AND SS5-CS1 42
FIGURE 3.18. INSTRUMENTS FOR SPECIMENS SS4-CS2 AND SS6-CS2 42
FIGURE 3.19. TESTING SETUP FOR 2-SPAN CONTINUOUS SLABS, CS1 AND CS2 43
FIGURE 3.20. LABORATORY SETUP FOR TESTING CONTINUOUS SLABS CS1 AND CS2 44
FIGURE 3.21. INSTRUMENTATION FOR SLABS CS1 AND CS2 45
FIGURE 3.22. DATA LOGGER AND RECORDING SYSTEM 46
FIGURE 3.23. STRAIN GAGE AND HORIZONTAL LVDT TO MEASURE THE COMPRESSIVE STRAIN IN CONCRETE 46
FIGURE 3.24. VERTICAL LVDT FOR DEFLECTION MEASUREMENT AND HORIZONTAL LVDT TO MEASURE THE TENSILE STRAIN IN CONCRETE 47

FIGURE 4.1. FLEXURAL SHEAR FAILURE OF SPECIMEN SS1 49

FIGURE 4.2. (A) FLEXURAL SHEAR FAILURE OF SPECIMEN SS2 50
FIGURE 4.3. LOAD-DEFLECTION CURVE FOR SPECIMEN SS1 51
FIGURE 4.4. LOAD-STRAIN CURVE FOR BOTTOM REINFORCEMENT - SPECIMEN SS1 52
FIGURE 4.5. LOAD-STRAIN CURVE FOR CONCRETE IN COMPRESSION - SPECIMEN SS1 53
FIGURE 4.6. LOAD-STRAIN CURVE FOR CONCRETE IN TENSION - SPECIMEN SS1 53
FIGURE 4.7. LOAD-DEFLECTION CURVE FOR SPECIMEN SS2 53
FIGURE 4.8. LOAD-STRAIN CURVE FOR BOTTOM REINFORCEMENT - SPECIMEN SS2 54
FIGURE 4.9. LOAD-STRAIN CURVE FOR CONCRETE IN COMPRESSION - SPECIMEN SS2 54
FIGURE 4.10. LOAD-STRAIN CURVE FOR CONCRETE IN TENSION - SPECIMEN SS2 55
FIGURE 4.11. SHEAR FAILURE OF SPECIMEN SS3-CS1 56
FIGURE 4.12. SHEAR FAILURE OF SPECIMEN SS4-CS2 56
FIGURE 4.13. LOAD-DEFLECTION CURVE FOR SPECIMEN SS3-CS1 57
FIGURE 4.14. LOAD-STRAIN CURVE FOR BOTTOM REINFORCEMENT - SPECIMEN SS3-CS1 58
FIGURE 4.15. LOAD-STRAIN CURVE FOR CONCRETE IN COMPRESSION - SPECIMEN SS3-CS1 58
FIGURE 4. 16. LOAD-DEFLECTION CURVE FOR SPECIMEN SS4-CS2 59
FIGURE 4.17. LOAD-STRAIN CURVE FOR BOTTOM REINFORCEMENT - SPECIMEN SS4-CS2 59
FIGURE 4.18. LOAD-STRAIN CURVE FOR CONCRETE IN COMPRESSION - SPECIMEN SS4-CS2 ..... **ERROR! BOOKMARK NOT DEFINED.**
FIGURE 4.19. SHEAR FAILURE OF SPECIMEN SS5-CS1 61
FIGURE 4.20. SHEAR FAILURE OF SPECIMEN SS6-CS2 61
FIGURE 4.21. LOAD-DEFLECTION CURVE FOR SPECIMEN SS5-CS1 62
FIGURE 4.22. LOAD-STRAIN CURVE FOR BOTTOM REINFORCEMENT - SPECIMEN SS5-CS1 62
FIGURE 4.23. LOAD-STRAIN CURVE FOR CONCRETE IN COMPRESSION - SPECIMEN S54-CS1 63
FIGURE 4.24. LOAD-DEFLECTION CURVE FOR SPECIMEN SS6-CS2 63
FIGURE 4.25. LOAD-STRAIN CURVE FOR BOTTOM REINFORCEMENT - SPECIMEN SS6-CS2 64
FIGURE 4.26. LOAD-STRAIN CURVE FOR CONCRETE IN COMPRESSION - SPECIMEN SS6-CS2 64
FIGURE 4.27. FLEXURAL SHEAR FAILURE OF SPECIMEN CS1 66
FIGURE 4.28. FLEXURAL SHEAR FAILURE OF SPECIMEN CS2 67
FIGURE 4.29. LOAD-DEFLECTION CURVE FOR SPECIMEN CS1 67
FIGURE 4.30. LOAD-STRAIN CURVE FOR TOP REINFORCEMENT AT MID-SUPPORT- SPECIMEN CS1 68

FIGURE 4.31.LOAD-STRAIN CURVE FOR CONCRETE IN COMPRESSION AT MID-SUPPORT- SPECIMEN CS1 68
FIGURE 4.32. LOAD-STRAIN CURVE FOR CONCRETE IN TENSION AT MID-SUPPORT- SPECIMEN CS1 69
FIGURE 4.33. LOAD-DEFLECTION CURVE FOR SPECIMEN CS2 69
FIGURE 4.34. LOAD-STRAIN CURVE FOR TOP REINFORCEMENT AT MID-SUPPORT- SPECIMEN CS2 70
FIGURE 4 35. LOAD-STRAIN CURVE FOR CONCRETE IN COMPRESSION AT MID-SUPPORT- SPECIMEN CS2 71
FIGURE 4.36. LOAD-STRAIN CURVE FOR CONCRETE IN TENSION AT MID-SUPPORT- SPECIMEN CS2 71
FIGURE 4.37. DEFLECTED SHAPE AND CRACKS FOR SLAB SS2 72
FIGURE 4.38. LEFT SPAN CRACKING AND DEFLECTION OF SLAB CS1 72
FIGURE 4. 39. DEFLECTION AND FLEXURAL SHEAR CRACKS FOR CONTINUOUS SLAB CS2 73
FIGURE 4.40. ELASTIC BEHAVIOR OF SLAB SS2 AS THE LOAD WAS RELEASED (TOP TO BOTTOM) 74

FIGURE 5.1. LOAD-DEFLECTION CURVE FOR SS1 AND SS2 76
FIGURE 5.2. LOAD-STRAIN CURVE FOR BFRP BARS IN TENSION AT MIDSPAN FOR SS1 AND SS2 . 77
FIGURE 5. 3.LOAD-STRAIN CURVE FOR CONCRETE IN COMPRESSION (AT MIDSPAN) FOR SS1 AND SS2 77
FIGURE 5.4. LOAD-DEFLECTION CURVE FOR SS3-CS1 AND SS4-CS2 78
FIGURE 5.5. LOAD-DEFLECTION CURVE FOR SS5-CS1 AND SS6-CS2 79
FIGURE 5.6. LOAD-STRAIN CURVE FOR BFRP BARS IN TENSION (7.25 IN. FROM MIDSPAN) FOR SS3-CS1 AND SS4—CS2 80
FIGURE 5.7. LOAD-STRAIN CURVE FOR BFRP BARS IN TENSION (19 IN. FROM MIDSPAN) FOR SS5-CS1 AND SS6—CS2 80
FIGURE 5.8. LOAD-DEFLECTION CURVE FOR CS1 AND CS2 82
FIGURE 5.9. LOAD-STRAIN CURVE FOR BFRP BARS IN TENSION (AT MID-SUPPORT) FOR CS1 AND CS2 83
FIGURE 5.10. LOAD-STRAIN CURVE FOR CONCRETE IN COMPRESSION (AT MID-SUPPORT) FOR CS1 AND CS2 83

FIGURE 5.11. EFFECTIVE MOMENT OF INERTIA VS. M_A / M_{CR} FOR SPECIMEN SS1 91
FIGURE 5.12. EFFECTIVE MOMENT OF INERTIA VS. M_A / M_{CR} FOR SPECIMEN SS2 91
FIGURE 5. 13. EFFECTIVE MOMENT OF INERTIA VS. M_A / M_{CR} FOR SPECIMEN SS3-CS1 92
FIGURE 5.14. EFFECTIVE MOMENT OF INERTIA VS. M_A / M_{CR} FOR SPECIMEN SS4-CS2 92
FIGURE 5.15. EFFECTIVE MOMENT OF INERTIA VS. M_A / M_{CR} FOR SPECIMEN SS5-CS1 93
FIGURE 5.16 EFFECTIVE MOMENT OF INERTIA VS. M_A / M_{CR} FOR SPECIMEN SS6-CS2 93

FIGURE 6. 1. HALF SYMMETRY MODEL FOR SIMPLY SUPPORTED SLABS 96
FIGURE 6. 2. QUARTER SYMMETRY MODEL FOR CONTINUOUS SLABS 97
FIGURE 6.3. LOAD-DEFLECTION CURVE - SS1 & SS2 (EXPERIMENTAL VS. FINITE ELEMENT) 98
FIGURE 6.4. LOAD-STRAIN CURVE FOR BFRP REBARS - SS1 & SS2 (EXPERIMENTAL VS. FINITE ELEMENT 99
FIGURE 6.5. LOAD-STRAIN CURVE FOR CONCRETE IN COMPRESSION - SS1 & SS2 (EXPERIMENTAL VS. FINITE ELEMENT) 99
FIGURE 6.6. LOAD-STRAIN CURVE FOR CONCRETE IN TENSION - SS1 & SS2 (EXPERIMENTAL VS. FINITE ELEMENT) 100
FIGURE 6.7. DEFLECTION (IN.) OF SLAB SS1 - FINITE ELEMENT ANALYSIS 100
FIGURE 6.8. CRACKING MAP FOR SLAB SS1 AT (A) CRACK INITIATION (B) 50% ULTIMATE LOAD (C) ULTIMATE LOAD 101
FIGURE 6.9. DEFLECTION (IN.) OF SLAB SS2 - FINITE ELEMENT ANALYSIS 101
FIGURE 6.10. CRACKING MAP FOR SLAB SS2 AT (A) CRACK INITIATION (B) 50% ULTIMATE LOAD (C) ULTIMATE LOAD 102
FIGURE 6.11. LOAD-DEFLECTION CURVE - CS1 & CS2 (EXPERIMENTAL VS. FINITE ELEMENT) . 104
FIGURE 6.12. LOAD-STRAIN CURVE FOR BFRP REBARS - CS1 & CS2 (EXPERIMENTAL VS. FINITE ELEMENT)..... 104
FIGURE 6.13. LOAD-STRAIN CURVE FOR CONCRETE IN COMPRESSION - CS1 & CS2 (EXPERIMENTAL VS. FINITE ELEMENT)..... 105
FIGURE 6.14. LOAD-STRAIN CURVE FOR CONCRETE IN TENSION - CS1 & CS2 (EXPERIMENTAL VS. FINITE ELEMENT)..... 105
FIGURE 6.15. DEFLECTION (IN.) OF SLAB CS1 - FINITE ELEMENT ANALYSIS..... 106

FIGURE 6.16. CRACKING MAP FOR SLAB CS1 AT (A) CRACK INITIATION (B) 50% ULTIMATE LOAD (C) ULTIMATE LOAD 106
FIGURE 6. 17. DEFLECTION (IN.) OF SLAB CS2 - FINITE ELEMENT ANALYSIS 107
FIGURE 6.18. . CRACKING MAP FOR SLAB CS1 AT (A) CRACK INITIATION (B) 50% ULTIMATE LOAD (C) ULTIMATE LOAD..... 107

NOTATION

A_f = area of FRP reinforcement, in.^{2} (mm^2)

$A_{f,bar}$ = area of one FRP bar, in.^{2} (mm^2)

A_s = area of tension steel reinforcement, in.^{2} (mm^2)

a = depth of equivalent rectangular stress block, in. (mm)

b = width of rectangular cross section, in. (mm)

C = spacing or cover dimension, in. (mm)

c = distance from extreme compression fiber to the neutral axis, in. (mm)

c_b = distance from extreme compression fiber to neutral axis at balanced strain condition, in. (mm)

d = distance from extreme compression fiber to centroid of tension reinforcement, in. (mm)

d_b = diameter of reinforcing bar, in. (mm)

d_c = thickness of concrete cover measured from extreme tension fiber to center of bar or wire location closest thereto, in. (mm)

E_c = modulus of elasticity of concrete, psi (MPa)

E_f = design or guaranteed modulus of elasticity of FRP defined as mean modulus of sample of test specimens, psi (MPa)

Es = modulus of elasticity of steel, psi (MPa)

f_c' = specified compressive strength of concrete, psi (MPa)

f_f = stress in FRP reinforcement in tension, psi (MPa)

h = overall height of flexural member, in. (mm)

I = moment of inertia, in.^{4} (mm^4)

I_{cr} = moment of inertia of transformed cracked section, in.^{4} (mm^4)

I_e = effective moment of inertia, in.^{4} (mm^4)

I_g = gross moment of inertia, in.^{4} (mm^4)

$K1$ = parameter accounting for boundary conditions

k = ratio of depth of neutral axis to reinforcement depth

L = span length, ft. (m)

M_a = maximum moment in member at stage deflection is computed, lb-in. (N-mm)

M_{cr} = cracking moment, lb-in. (N-mm)

M_n = nominal moment capacity, lb-in. (N-mm)

M_u = factored moment at section, lb-in. (N-mm)

n_f = ratio of modulus of elasticity of FRP bars to modulus of elasticity of concrete

β_1 = factor taken as 0.85 for concrete strength f_c' up to and including 4000 psi (28 MPa). For strength above 4000 psi (28 MPa), this factor is reduced continuously at a rate of 0.05 per each 1000 psi (7 MPa) of strength in excess of 4000 psi (28 MPa), but is not taken less than 0.65

β_d = reduction coefficient used in calculating deflection

ε_c = strain in concrete

ε_{cu} = ultimate strain in concrete

ε_f = strain in FRP reinforcement

ε_{fu} = design rupture strain of FRP reinforcement

η = ratio of distance from extreme compression fiber to centroid of tension reinforcement (d) to overall height of flexural member (h)

ρ' = ratio of steel compression reinforcement, $\rho' = A_s'/bd$

ρ_b = steel reinforcement ratio producing balanced strain conditions

ρ_f = FRP reinforcement ratio

ρ_f' = ratio of FRP compression reinforcement

ρ_{fb} = FRP reinforcement ratio producing balanced strain conditions

ϕ = strength reduction factor

SUMMARY

The implementation of Basalt Fiber Reinforced Polymers (BFRP) in bridge decks supported on girders, where deflection is not an issue, has the potential to offer an efficient solution that is corrosion resistant, durable and cost effective. However, due to the lack of research studies conducted on this material, the current FRP design guidelines do not encompass sufficient specifications to describe and regulate its design and utilization. Therefore, in this paper, the structural behavior of Lightweight Concrete (LWC) bridge decks, reinforced with BFRP reinforcing bars, was studied.

The research program included experimental testing of eight LWC bridge deck specimens reinforced with BFRP reinforcing bars. The cross section of the specimens was 18 x 8 in. with a length to height ratio (L/H) equal to 9, 10, and 13. The purpose of testing program was to study the structural behavior of bridge decks supported on girders, in addition to the pre-cracking and post-cracking behavior till the failure of the specimens. Two of the specimens were simply supported with a span length of 6.67 ft. and a length to height ratio (L/H) equal to 10; and were reinforced with 5 BFRP bars of diameter 0.625 in. and 5 BFRP bars of diameter 0.5 in. at the bottom, respectively. The ratio of the bottom to the balanced reinforcement areas (ρ_f/ρ_{fb}) were 4.1 and 2.6, respectively. Top reinforcement consisted of 5 BFRP bars of 0.375 in. for both specimens.

Two additional specimens were continuously supported with two spans of 8.67 ft. each, (L/H) ratio of 13, and were tested for positive and negative moment capacities. The two continuous specimens were reinforced with 5 BFRP bars of diameter 0.625 in. and 5 BFRP bars of diameter

0.5 in. at the bottom with (ρ_f/ρ_{fb}) equal to 4.1 and 2.6, respectively. The specimens were reinforced at the

SUMMARY (continued)

top with 6 BFRP bars of 0.625 in. diameter and 6 BFRP bars of 0.5 in. diameter with (ρ_f/ρ_{fb}) equal to 5.1 and 3.2, respectively. The four other specimens were simply supported reinforced as the two continuous decks, with a varying span of 6 and 8 ft., and (L/H) equal to 9 and 12 respectively.

The nominal moment capacities (M_n) were accurately predicted by the specifications of the ACI 440.1R (2006), however the ultimate moment capacities (ϕM_n) were conservative due to a lower strength reduction factor (ϕ). The deflections of the BFRP reinforced deck specimens were high due to the relatively lower modulus of elasticity of BFRP bars.

CHAPTER 1

INTRODUCTION

1.1 Background

It has been more than a century since iron and steel were first used as reinforcement materials for concrete. Steel has dominated the construction field since then, despite its well-known disadvantages. Corrosion is the most common source of structural deterioration of bridges, particularly in severe weather conditions where deicing salts are required or structures located by seawater. Within the 600,000 bridges in the United States, half were built between 1950 and 1994 and cost approximately 8.3 billion USD annually in repairs or replacement, including highways (NACE, 2002). The I-35 Bridge in Minnesota, USA, which was built in 1964, completely collapsed in 2007 after suffering from corrosion in one of the gusset plates (NTSB, 2008). Epoxy-coated steel bars appeared to be a feasible solution, however, ACI 440.1R (2006) reported that when it was implemented in harsh weather conditions, these bars still corroded. Moreover, a study in 2005 estimates that iron ore reserves will only last for 64 years, based on a modest assumption of 2% annual consumption growth (USGS, 2005).

Researchers sought solution to the aforementioned problems through the utilization of Fiber Reinforced Polymers (FRP) composites. FRP is a brittle elastic material which behave linearly until it fails. Carbon FRP (CFRP), Aramid FRP (AFRP) and Glass FRP (GFRP) have been introduced to civil-engineering applications in the last three decades, offering higher ultimate strength and lighter weight compared to steel; better resistance to corrosion and chemical attacks; as well as being more environmentally friendly and sustainable. AFRP and GFRP also have low thermal and electrical conductivity (Nanni et al, 1993). Basalt FRP (BFRP) is the most recent

addition to this group of materials. Compared to E-Glass fibers, Basalt fibers possess higher strength and modulus of elasticity, better alkali resistance, good insulation, the functionality in a broader range of temperatures, and a failure strain greater than the more expensive Carbon fibers. These advantages over other FRP composites rendered BFRP more promising for applications like aerospace, transportation, construction, automobile and fire protection (Lopresto et al, 2011). However, the limited available research combined with the lack of an adopted civil-engineering design guidelines in the United States are delaying the use of BFRP and taking advantage of its superior properties. High initial cost associated with the fabrication of BFRP bars is also another issue that hinders the widespread use, although Patnaik (2009) reported that the new wet layup fabrication process will significantly reduce the manufacturing costs.

Currently, the guidelines provided by ACI Committee 440 only cover the use of CFRP, AFRP and GFRP through two application methods. The first is strengthening concrete structures through externally bonded FRP systems, such as fiber sheets. Ever since its first use in the 1980s, it has been employed to strengthen beams, columns, joints, trusses and other structural elements as an alternative to traditional approaches which used steel plates or columns. The second method comprises of reinforcing concrete with FRP bars. Manufacturing of the three common FRP composites involves embedding the fibers in resins, such as epoxy, vinylesters and polyesters which are categorized as thermoset resins (ACI 440.1R (2006) and ACI 440.2R (2008). This group of resins provides excellent resistance to heat, corrosion and chemicals. In addition, thermoset resins exhibit high fatigue strength and adhesion and are available commercially at low costs, which made them the most commonly used resins in the manufacturing process of FRP composites. The other group is thermoplastic resins, which differs from the thermoset resins in its much higher impact resistance and the ability to be reshaped after

curing through heat and the higher cost. However, Bakis et al (1998b) stated that bending FRP bars causes stress concentration in the fibers and necessitates reducing the design strength by 40 to 50%.

On the other hand, FRP composites have disadvantages which constrain their use in certain applications and completely inhibit it in others. For instance, the lack of ductile behavior limit their use in seismic applications. Likewise, utilizing FRP bars in compression is inadvisable as compressive strengths drop to as low as 20% of the tensile strength for AFRP, 55% for GFRP and 78% for CFRP (Mallick, 1988 and Wu, 1990). Furthermore, FRP reinforcement has low transverse strength; its strength depends on load direction relative to the fibers direction. Additionally, the low modulus of elasticity results in greater deflections and crack widths than those experienced with steel. It is also reported that GFRP and AFRP have low alkali resistance. Moreover, the fire resistance of all FRP composites depend mainly on the type of resin used in the reinforcement bars and the concrete cover provided in the structural element. (ACI 440.1R, 2006) Finally, higher initial cost resulting from raw materials or fabrication process is yet another obstacle facing these alternative materials.

1.2 Research Significance

Until today, steel remains the most commonly used reinforcing material in the construction industry. Significant amount of research was done in order to fully understand the structural behavior of steel, and in attempts to overcome its major shortcoming which threatens the integrity of structures; corrosion. Corrosion is the product of attacks caused by chemicals containing chloride ions. Such chemicals are found by seawater or induced internally into concrete structures through aggregates contaminated with chloride, or externally through deicing salts. Chloride ions de-passivate the protective layer which protects the steel from deep

corrosion. Consequently, the regions of exposed steel corrode and the bond between steel and concrete is weakened. Corrosion causes volume expansion, which leads to what is known as corrosion stresses. These stresses eventually cause cracks, concrete spalls, loss of reinforcement area, and ultimately, an overall reduction of the structure's service life and aesthetics (Cabrera, 1996, and Fang et al, 2004)

Several practices are implemented to provide a protective coating for steel, including galvanizing, PVC or Nylon coating, stainless-steel clad and epoxy coating, with the latter being the one mainly used for steel reinforcement. However, even epoxy-coated bars suffered from corrosion after few years in service. The Canadian Strategic Highway Research Program (C-SHRP) conducted a study on 19 structures including 3000 samples of epoxy-coated bars taken from highway decks and barrier walls, jobsites and manufacturers. The samples unveiled cracks in the coating, contamination beneath its surface and loss of adhesion. Given the quality of the rebars at jobsites, C-SHRP concluded that epoxy coating can only extend their service life by 3 to 6 years compared to uncoated rebars. According to the article published in Civil Engineering Journal (1993), considering manufacturer's quality rebars in best cases, the service life would be extended 8 to 11 years.

The need for non-corrosive reinforcement emerged from the increasing demand for eliminating of the corrosion issue faced by concrete structures, which causes direct costs of multibillion dollars and tenfold this figure in indirect costs. Considering the advantages of BFRP over other FRP composites, it is evident that it would provide the best choice to replace steel in several applications. Bridge decks exposed to deicing salts and concrete structures in marine environments would benefit the most if reinforced with BFRP rebars. However, in order to

advance in the use of this relatively new material, it needs to be supported by research and design recommendations leading to a widely adopted code.

1.3 Research Objective

The primary objective of this research is to evaluate the practicality of adopting the use of BFRP rebars as flexural reinforcement for structural concrete elements, with emphasis on bridge deck slabs. Achieving this requires investigating the strength and serviceability aspects of BFRP reinforced slabs, and comparing the results to the design guidelines provided by ACI 440.1R (2006) for other FRP rebars. The study is performed by testing eight lightweight air-entrained concrete slabs; six of which are simply supported and two continuous ones, reinforced with different ratios and spanning over different lengths. For all specimens, the following tasks are to be achieved in order to accomplish the primary objective of this research:

- Determining the ultimate load at failure
- Investigating the mode of failure
- Studying the load-deflection behavior
- Measuring the strains for BFRP bars and concrete at critical locations
- Comparing the experimental cracking and ultimate moments with the calculated values.

CHAPTER 2

Literature Review

2.1. FRP Composites

FRP composites are anisotropic materials consisting of two major components; the reinforcing fibers and the matrix. The characteristics of a composite material depend on the aspects of its constituents; the strength and stiffness properties are governed by the type of continuous fibers used, fiber volume ratio, and fiber directionality. The latter directly affects the anisotropy of the composite material; the better orientation of fibers, the more anisotropic is the material and the lower is the probability of failure. On the other hand, the matrix protects the fibers and transfers the local stress between them. In some FRP composites, a small fraction of additives is added to help control the failure mechanism. (Daniel and Ishai, 1994)

FRP bars are unidirectional composites in which all fibers are oriented in the same direction. While the constituting fibers possess much higher elastic moduli and ultimate strengths than those for steel, their corresponding FRP bars retain only a fraction of those values, due to the lower strength and modulus of the matrix used in the manufacturing process. For example, the ultimate tensile strength and Young's modulus of Glass fibers are 224.8 and 12,330 ksi, respectively, whereas these values drop to as low as 70 and 5,100 ksi respectively, for GFRP bars. (Kaw, 2006, and ACI 440.1R, 2006). With densities of one-fourth to one-third that of steel, CFRP, GFRP and AFRP bars share the same linearly elastic tensile behavior when loaded in

tension, exhibiting no yielding or ductility until their failure, which is characterized by rupture of fibers.

2.2 BFRP Bars

2.2.1 Mechanical Properties

Basalt fibers are naturally acquired from melting volcanic basalt rocks and processing the product through small nozzles. The end product is continuous basalt fibers with no need for additional constituents, hence reducing the cost by limiting the manufacturing to a single process. Both its modulus of elasticity and tensile strength are greater than E-Glass fibers, in addition to a higher ultimate strain than Carbon fibers. Figure 2.1 below illustrates the behavioral differences between steel and other FRP fibers. (Sim et al, 2005)

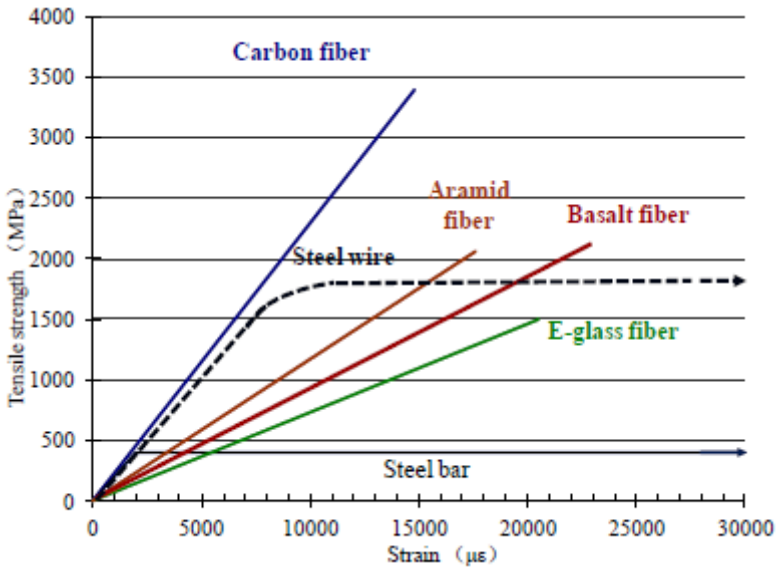

Figure 2.1. Stress-Strain Relationship for Steel and Different FRP Bars

Ovitigala (2012) sought to determine the mechanical properties of BFRP bars by testing 5 specimens of each of the 5 different bar sizes: 6 mm, 10 mm, 13 mm, 16 mm and 25 mm. The tensile strength slightly decreased as the bar diameter increased, with values of 160.2 ksi, 162.6 ksi and 156.9 ksi for the 6 mm, 10 mm, and 13 mm bars, respectively. All bar diameters exhibited brittle failure by rupture of the fibers. Similarly, the modulus of elasticity of each bar size was also determined and found to decrease with the increase of the bar diameter, except for the 6 mm bars. The minimum value of 7260 ksi was obtained from the 25 mm bars, while the 8 mm bars had the greatest modulus of 8022 ksi. As expected, the linear stress-strain curve continued until failure for all specimens. The ultimate strain at failure was as high as 20588 με for the 13 mm bars and 21171 με for the 6 mm bars. Moreover, Ovitigala (2012) investigated the development length of the BFRP bars through two experimental methods: the flexural bond test and the pullout bond test. In the first test method, a total of twenty specimens were tested, representing five different BFRP bar sizes and three bonding lengths. He reported that by using a bond length ten times the bar diameter, the BFRP bars had better performance than GFRP bars, and quite similar results to steel. When the bond length was increased to twenty times the bar diameter, all specimens failed by rupture; thus it was considered as the acceptable development length for BFRP bars. The pullout bond test confirmed these results through testing a total of twenty four specimens representing four bar sizes and three bond lengths.

2.2.2 Durability Properties

The long-term durability of basalt fibers was investigated by Sim et al (2005) and compared to that of glass and carbon fibers. His study consisted of experiments to evaluate resistance to alkali, weathering, autoclave, and thermal stability. The alkali-resistance study involved immersing all three types of fibers in Sodium Hydroxide solution for 28 days. The eroded

amount of each specimen was measured by observing the volumetric change at 7, 14, 21 and 28 days, which indicated the loss of strength. The results for basalt and glass fibers were similar; both lost half their strength at 7 days and four-fifths at 28 days. Carbon fibers, on the other hand, retained 87% of its strength after 28 days and showed less deterioration than the other two.

The three fibers were also tested for weathering resistance according to the Japanese Industrial Standards (JIS A 1415: Recommended practice for accelerated artificial exposure of plastics building materials). The fibers were subjected to 4000 hours of ultra-violet exposure, representing 20 years of natural sunshine. The results revealed almost no reduction in the tensile strength of carbon fibers, while the rate of strength reduction in glass fibers was double that for basalt fibers. The thermal stability was investigated by measuring the tensile strength and visually inspecting the three fibers after having them subjected to temperatures of 100, 200, 400, 600 and 1200 ºC. The samples showed no significant change in the strength until 200 ºC. At higher temperatures, all fibers suffered from strength reduction, however, basalt fibers were the least affected. At 600 ºC, the tensile strength for carbon and glass fibers was reduced by more than 40%, while basalt merely lost 10% of its strength. At 2 hours of 1200 ºC, a condition that simulates exposure to fire, carbon fibers completely melted and glass fibers were partially molten. In contrast, basalt fibers exhibited higher volumetric stability and was able to sustain the elevated temperature while maintaining its shape and strength. In conclusion, basalt fibers proved to have superior thermal stability compared to carbon and glass fibers.

2.3 Flexural Behavior and Capacity of BFRP Reinforced Concrete Beams and Slabs

According to ACI 440.1R (2006), the approach for the flexural design of concrete beams reinforced with FRP bars is quite similar to that of traditional beams reinforced with steel bars. The assumptions presumed for steel also hold for FRP, and are summarized as follows:

- Concrete bonds perfectly with FRP reinforcing bars.
- The tensile stress-strain relationship for FRP reinforcement is linear until failure.
- The maximum usable concrete strain is 3000 με
- The strain in both concrete and FRP bars can be proportionally calculated based on the distance from the neutral axis. This is established from the assumption that a plane section remains plane after loading. Sections perpendicular to the axis of bending that are before and after bending remain plane.

Depending on the reinforcement ratio (the ratio of reinforcement area to the cross sectional area of the beam), which determines the failure mode, reinforced concrete beams are divided into three categories: Under-reinforced, over-reinforced, and balanced. In the case of balanced section of concrete beam reinforced with steel bars, the yielding of the steel in the tension zone occurs simultaneously with the concrete strain reaching 3000 με. If the reinforcement area is reduced, the section becomes under-reinforced and the steel reinforcement reaches the yield strain before the concrete reaches the maximum usable strain in the compression zone. This case represents the desirable design approach for concrete beams reinforced with steel bars. Steel behaves in a ductile manner after it yields and signs of failure gradually occur, resulting in a safe mode of failure. To ensure that this kind of failure takes place and to avoid disastrous failure by lack of reinforcement, a minimum reinforcement ratio is used. Over-reinforced case occurs in sections with reinforcement ratio higher than that in balanced condition. The strain in concrete reaches 3000 με before the steel yielding is initiated. The brittle failure is then caused by the crushing of the concrete in the compression zone. ACI 318 (2011) prohibits this failure by enforcing a minimum strain in steel reinforcement enough to utilize its ductile behavior after yielding.

The discussion above pertains to steel reinforcement. In the case of FRP, the reinforcing bars do not yield. Instead, they exhibit a linearly elastic behavior until a sudden failure occur by rupture without warning. If the beam is in the balanced condition, failure of the FRP bars occurs at the same time that concrete reaches 3000 με in the compression region. Similar to steel, the failure occurs in the reinforcing bars first. However, the FRP bars would fail suddenly in a very brittle manner causing a catastrophic failure. If the beam is over-reinforced, the failure would first occur in concrete, which is considered by Bank (2006) to be less brittle than the rupture of FRP bars. In fact, Nanni (1993) indicated that designing for a failure mode of concrete crushing is preferable over rupture of FRP bars. On the contrary, ACI 440.1R (2006) adopted both failure modes for the design of flexural members reinforced with FRP bars, as long as the strength and serviceability requirements are met.

Researchers established different approaches to insure that the failure is not caused by rupture of FRP bars. (Faza and Rao, 1993a) suggested that the allowable tensile stress for GFRP bars shall be limited to 80% of the ultimate strength. Nanni (1993) recommended to lower the strength reduction factor (ϕ) to 0.7, instead of 0.9 which is used for steel. His reasoning was the lack of plasticity in FRP bars. Moreover, he indicated that only a minimum reinforcement limit shall be set, not a maximum one. Thus, he suggested to limit the stress in the reinforcement to two-third the ultimate strength, and the minimum reinforcement ratio to the larger of 1.33 the balanced ratio (1.33 ρ_{bal}) or $24\sqrt{f_c'}/f_{pu}$. However, Ovitigala and Issa (2012) stated that an upper limit must be established, not only to avoid an undesirable failure mode due to shear, but also to maintain economical design and to comply with other limitations such as spacing between bars and aggregate size. Their suggested limit was that the strain in BFRP reinforcing bars shall be at

least 5000 με. They also stated that the strength reduction factor (ϕ) could be increased to 0.74 for BFRP reinforced beams designed to fail by concrete crushing.

In one of the GFRP-reinforced concrete studies, Alsayed et al (2000) attempted to adjust the moment capacity equation in ACI 318 (1992) which is used to calculate the nominal moment capacity for steel-reinforced concrete beams. In the modified equation, (Eq. 2.1), they introduced what they called pseudo yield tensile strength (f_{py}) for GFRP bars to replace the yielding strength of steel (f_y), and suggested that (f_{py}) shall equal two-thirds the ultimate tensile strength (f_{pu}). In other words, they included a factor of safety of 1.5. However, the moment capacity in Eq. 2.1 is based on the rupture of GFRP bars, which is more brittle compared to a compressive failure. Thus, they proposed an expression (Eq. 2.2) to calculate the nominal moment capacity based on the failure in compression zone of concrete.

$$M_n = A_p f_{py} d\left(1 - 0.59\rho_p \frac{f_{py}}{f_c'}\right) \qquad Eq.2.1$$

$$M_n = A_p f_{ps}\left(d - \frac{a}{2}\right) \qquad Eq.2.2$$

M_n = nominal moment capacity of a section, N.mm

A_p = area of GFRP reinforcement bars in tension region, mm^2

f_{py} = pseudo yield tensile strength of GFRP reinforcement bars = 0.67 f_{pu}, MPa

f_{ps} = the computed stress of GFRP bars, MPa ($\leq f_{py}$)

d = distance from extreme compression fiber to centroid of tension reinforcement, mm

ρ_p = ratio of tension reinforcement = A_p / bd

f_c' = compressive strength of concrete, MPa

b = width of concrete section, mm

a = depth of equivalent rectangular stress block, mm

c = distance from extreme compression fiber to the neutral axis, mm

A compression failure implies that the strain in the GFRP bars (ε_{ps}) is less than the pseudo strain yield limit (ε_{py}). In a similar manner to steel reinforced concrete, the strain in the GFRP bars is calculated using Eq. 2.3 and the stress in the bars is found from the linear relationship as shown in Eq. 2.4. E_p represents the modulus of elasticity of GFRP bars.

$$\varepsilon_{ps} = \varepsilon_{cu}\frac{(d-c)}{c} \qquad Eq.2.3$$

$$f_{ps} = E_p\varepsilon_{ps} \qquad Eq.2.4$$

The distance is calculated from the following expression:

$$c = \left[\sqrt{m\rho_p + \left(\frac{m\rho_p}{2}\right)^2} - \frac{m\rho_p}{2}\right]d \qquad Eq.2.5$$

Where parameter m depends on the properties of concrete and reinforcement, and is equal to $(E_p\epsilon_{cu})/(0.85\beta_1 f_c')$.

ACI 440.1R (2006) also recognized two flexural design approaches for FRP reinforced concrete members; tensile failure of FRP bars and compressive failure of concrete. The mode of failure is governed by the FRP reinforcement ratio compared to the balanced reinforcement ratio (ρ_f/ρ_{fb}), where ρ_{fb} is calculated using Eq. 2.6:

$$\rho_{fb} = 0.85\beta_1 \frac{f_c'}{f_{fu}} \frac{E_f \varepsilon_{cu}}{E_f \varepsilon_{cu} + f_{fu}} \qquad Eq.2.6$$

In the case where $\rho_f > \rho_{fb}$, the concrete reaches the usable strain of 3000 με, so crushing of the concrete causes the failure. The nominal moment capacity is derived from in Eq. 2.7 and the depth of the concrete stress block, *a*, is calculated as shown in Eq. 2.8.

$$M_n = A_f f_f \left(d - \frac{a}{2}\right) \qquad Eq.\ 2.7$$

$$a = \frac{A_f f_f}{0.85 f_c' b} \qquad Eq.\ 2.8$$

Since the FRP bars are linearly elastic, the stress of the reinforcement at failure f_f can be found from Eq. 2.9.

$$f_f = E_f \varepsilon_{cu} \frac{(\beta_1 d - a)}{a} \qquad Eq.2.9$$

Another expression is given for f_f by substituting *a* from Eq. 2.8 into Eq. 2.9, as presented in Eq. 2.10. The calculated stress shall be less than the ultimate design stress f_{fu}.

$$f_f = \sqrt{\frac{\left(E_f \varepsilon_{cu}\right)^2}{4} + \frac{0.85\beta_1 f_c'}{\rho_f} E_f \varepsilon_{cu}} - 0.5 E_f \varepsilon_{cu} \qquad Eq.2.10$$

In the other case of failure when $\rho_f < \rho_{fb}$, the failure is governed by the rupture of FRP bars as the stress reaches its ultimate value. The code argues that since the strain in concrete doesn't reach 3000 με, the rectangular concrete stress block theory cannot be applied. The analysis in this case involves two unknowns; the strain in the concrete at failure ε_c, and the depth to the neutral axis *c*. To overcome this, a conservative method is suggested by using the depth to the neutral axis in the balanced condition c_b which corresponds to a concrete strain of 3000

με, although this is not the actual case. The nominal moment capacity is then calculated from Eq. 2.11 and Eq. 2.12.

$$M_n = A_f f_{fu}\left(d - \frac{\beta_1 c_b}{2}\right) \qquad Eq.\ 2.11$$

$$c_b = \left(\frac{\varepsilon_{cu}}{\varepsilon_{cu} + \varepsilon_{fu}}\right) d \qquad Eq.\ 2.12$$

Adhikary (2009) studied 13 simply supported beams, sized 8 x 7 x 84 in., two of which were steel reinforced and the remaining were reinforced with different ratios of BFRP bars, using small sizes of 3, 5 and 7 mm. Some of the beams had flexural capacities less than the nominal capacities expected by ACI 440.1R.

Ovitigala and Issa (2012) tested eight simply-supported lightweight concrete beams reinforced with BFRP utilizing four different relative reinforcement ratios (ρ_f/ρ_{fb}); two under-reinforced, one balanced and one over-reinforced. In addition, eight simply-supported normal weight concrete beams were tested, all of which are over-reinforced ($\rho_f/\rho_{fb} > 1$), each with a different reinforcement area. All beams had 8x12 in. cross-section with 10 ft. span length. The mode of failure was predicted using ACI 440.1R (2006). As expected, all under-reinforced and balanced beams failed by the rupture of BFRP bars, while the two over-reinforced ones failed by crushing of concrete. The ultimate moment capacity of the BFRP over-reinforced beams was higher than that of steel-reinforced LWC beams having double the reinforcement area of BFRP beams. Moreover, they reported that the observed ultimate moment capacity was double the factored moment predicted by ACI 440.1R, due to the conservative strength reduction factor of 0.65 for beams failing by concrete crushing. However, the nominal capacity ranged between 77 and 86% of the experimental moment. Their tests also confirmed that all normal-weight concrete (NWC)

beams failed by crushing of concrete at the mid-span. They stated that ACI 440.1R gave better estimate of the nominal capacity of NWC beams than LWC beams, with values ranging between 82% and 93% of the experimental moment capacity. The ultimate moment capacity, however, was conservatively 53-61% of the experimental capacity. Furthermore, after comparing their results with 9 other studies, they concluded that the equations in ACI 440.1R were able to accurately predict the nominal moment capacities for under and over-reinforced beams. They also suggested that equation 8-4a in ACI 440.1R (2006) (Eq. 2.7 herein) is capable of precisely predicting the nominal capacity for both cases. Additionally, based on results from 72 out of 73 specimens in 10 studies, they recommended increasing the strength reduction factor to 0.74.

2.4 Serviceability of FRP Reinforced Beams

Whether the reinforcement is provided by steel or FRP bars, serviceability is considered a major factor in determining the structural design of concrete beams. The two parameters of serviceability, deflection and size of cracks, are essential in providing sound and economical cross-sections. For steel reinforced beams and slabs, ACI 318 (2011) provides a guiding table to limit the deflection within the acceptable values, by specifying maximum span-to-depth ratio of the member. Alternatively, the short-term deflection is directly calculated and compared to the maximum allowable values provided in the code. However, this procedure requires determining the effective moment of inertia of the flexural concrete element, which is calculated in ACI 318 (2011) using the empirically-derived Branson's equation (Eq. 2.13) for steel reinforced concrete.

$$I_e = \left(\frac{M_{cr}}{M_a}\right)^3 I_g + \left[1 - \left(\frac{M_{cr}}{M_a}\right)^3\right] I_{cr} \leq I_g \qquad Eq.\ 2.13$$

Alsayed et al. (2000) studied the flexural capacity and deflection of GFRP reinforced beams. They tested the specimens under service loads and used the results to modify the cubic form of

Branson's formula into an expression that depends on the power "*m*", as shown in Eq. 2.14. The modified equation is best correlated with service loads when the value of *m* equaled 5.5. Furthermore, they developed a new set of equations (Eq. 2.15 and 2.16) to calculate the effective moment of inertia.

$$I_e = \left(\frac{M_{cr}}{M_a}\right)^m I_g + \left[1 - \left(\frac{M_{cr}}{M_a}\right)^m\right] I_{cr} \leq I_g \qquad Eq.2.14$$

Where $m = \dfrac{log\left(\frac{I_e - I_{cr}}{I_g - I_{cr}}\right)}{log\left(\frac{M_{cr}}{M_a}\right)}$

The results of the same specimens were also utilized to develop a new equation, as shown in the equations below:

$$I_e = \alpha I_{cr} \text{ for } 1.0 < \frac{M_a}{M_{cr}} < 3.0 \qquad Eq.2.15$$

$$I_e = I_{cr} \text{ for } \frac{M_a}{M_{cr}} > 3.0 \qquad Eq.2.16$$

Where $\alpha = 1.4 - \dfrac{2}{15}\left(\dfrac{M_a}{M_{cr}}\right)$

Gao et al. (1998a) recommended a modified version of Branson's equation, as shown in Eq. 2.17. Their study concluded that the effect of tension stiffening (defined as the increase in stiffness of cracked concrete member due to the development of tensile stresses between cracks), is less in FRP reinforced members than steel reinforced elements. They introduced the factor β_d to Branson's formula in order to reduce the effect of tension stiffening based on the

ratio (ρ_f/ρ_{fb}) as stated by Toutanji and Saafi (2000) and Yost et al. (2003). ACI 440.1R (2006) simplified the equation suggested by Gao et al. (1998a) to calculate β_d. The committee's recommended equation is shown in Eq. 2.18.

$$I_e = \left(\frac{M_{cr}}{M_a}\right)^3 \beta_d I_g + \left[1 - \left(\frac{M_{cr}}{M_a}\right)^3\right] I_{cr} \leq I_g \qquad Eq.\ 2.17$$

$$\beta_d = \frac{1}{5}\left(\frac{\rho_f}{\rho_{fb}}\right) \leq 1.0 \qquad Eq.2.18$$

The moment of inertia for the cracked section I_{cr} is calculated using elastic analysis similar to that for steel-reinforced sections, which neglects the concrete in tension. The equations are presented below:

$$I_{cr} = \frac{bd^3}{3}k^3 + n_f A_f d^2(1-k)^2 \qquad Eq.2.19$$

$$\text{Where } k = \sqrt{2\rho_f n_f + (\rho_f n_f)^2} - \rho_f n_f \qquad Eq.2.20$$

Bischoff (2005) assessed some of the common methods used to consider the tension stiffening factor in calculating the short-term deflection for beams and slabs. He stated that Branson's equation overestimates the stiffness of flexural members (represented by the effective moment of inertia) with steel reinforcement ratios less than 1%, and so the calculated deflection is underestimated for such members. He also pointed out that this is even more evident in FRP-reinforced members where the ratio I_g / I_{cr} is very large. He then proposed a new expression to calculate the effective moment of inertia, given in Eq. 2.21.

$$I_e = \frac{I_{cr}}{1 - \eta\left(\frac{M_{cr}}{M_a}\right)^2} \leq I_g \qquad Eq.2.21$$

Where $\eta = (1 - \frac{I_{cr}}{I_g})$

For validation, Bischoff (2005) used this expression to study the relationship between the applied moment and deflection for eight simply supported steel-reinforced one-way slabs and compared the results with Branson's equation. The reinforcement ratio of the eight slabs ranged between 0.18 and 1%. Four of them had a span length of 3,500 mm and were tested under a concentrated load applied at the midspan. The other four slabs had a 2000 mm span length and were subjected to two point loads at third span. The comparison indicated that Branson's expression underestimated the deflection for slabs with low reinforcement ratios, while it provided better estimation for slabs with higher reinforcement ratios. On the other hand, Bischoff's equation was more accurate in estimating the deflection over the full range of reinforcement ratios.

Bischoff (2007) investigated the deflection of reinforced concrete beams and slabs. He restated that Branson's formula underestimates the deflection for FRP reinforced flexural members and those reinforced with low steel reinforcement ratios. Moreover, he proposed an expression to calculate the stiffness of continuous beams using an averaged moment of inertia, $I_{e,avg}$, as shown in Eq. 2.22.

$$I_{e,avg} = \frac{KI_{em}}{1 + 0.1\beta_{M1}\beta_{I1} + 0.1\beta_{M2}\beta_{I2}} \qquad Eq.\,2.22$$

$$Where\ \beta_{M1,2} = \frac{M_{a1,2}}{M_m}\ and\ \beta_{I1,2} = \frac{I_{em}}{I_{e1,2}}$$

$I_{e,avg}$: averaged effective moment of inertia

$I_{e1,2}$: effective moment of inertia at first and second supports, respectively.

I_{ec} : effective moment of inertia at continuous end

I_{em} : effective moment of inertia at midspan

I_g : gross moment of inertia

K : beam deflection coefficient, $K = 1 + 0.1(M_{a1} + M_{a2})/M_m$

M_a : applied service load moment

M_{a1} : support moment at first support

M_{a2} : support moment at second support

M_m : midspan moment

For a simply supported beam, Eq. 2.22 gives $I_{e,avg} = I_{em}$.

Bischoff noted that this proposed equation greatly underestimates the deflection if the stiffness at the midspan is more than double the stiffness at the end supports, which makes it inapplicable for fixed-end cantilevers.

Ovitigala and Issa (2012) compared the experimental deflections of eight simply supported BFRP-reinforced beams with the deflections calculated using the equations in ACI 440.1R (2006) and Bischoff (2007), given in Eq. 2.17 and 2.21, respectively. At ultimate load, the predicted deflections of both models were similar (72 to 87% of the experimental deflection), since I_e is equal to I_{cr}. At 60% and 40% of the ultimate load, the ratio changes to 78-87% and 60-81% for ACI's model, compared to 79-91% and 76-91% for Bischoff's model, respectively. It is evident that the latter was able to predict the deflection more precisely at the range of service loads; however, both estimations underestimated the deflection for all cases. For this reason, Ovitigala and Issa (2012) recommended multiplying the predicted deflections by a factor of 1.5 for Bischoff's model, and a higher factor when using the model in ACI 440.1R (2006).

CHAPTER 3
EXPERIMENTAL PROGRAM

3.1 Materials

3.1.1 BFRP Reinforcing Bars

Basalt fibers are a product of a naturally available resource in the earth's crust. This resource is a volcanic rock known as basalt. The process of extracting basalt and producing basalt fibers has minimum impact on the environment, making it a green material in comparison to other construction materials. The manufacturing process of the continuous basalt fibers starts with quarrying and crushing the basaltic rocks. The crushed rocks are then heated to 3000 º F until it completely melts. After that, the molten rocks are continuously stirred for 6 hours to attain a perfectly homogeneous liquefied basalt glass. It is then drawn into special ceramic fixtures with as many as 1600 holes. The resulting fibers are stretched to form an aligned molecular structure with the required diameter. Finally, a cooling agent is added to the fibers, not only to cool the fibers but also to speed up the process of applying the epoxy coat. The BFRP bars are manufactured through the pultrusion process, where the basalt fibers are impregnated with resin through a bath which is connected to the small dies until the desired diameter is obtained and the resin transforms to a solid. The type of resin plays a vital role in the durability of the rebars by

protecting them from the severe environmental conditions. Moreover, it provides the shear strength for the rebars, because basalt fibers are uniaxial and weak in the transverse direction

This research used BFRP bars with diameters of 10, 13 and 16 mm. Ovitigala and Issa (2012) tested these rebars at UIC laboratories to obtain their mechanical properties. The results are shown in Table 3.1 and are compared with values from the manufacturer. For the 10 and 13 mm bars, five specimens were tested; two using steel anchorage and three concrete anchorage. The 16mm bars were all tested using concrete anchorage, however, the ultimate stress could not be obtained as the pullout load exceeded the bond strength between the bar and the anchorage. All bars exhibited a linearly elastic behavior until failure by rupture of the fibers.

Bar Diameter (mm)	**Ultimate Stress (ksi)**		**Modulus of Elasticity (ksi)**		**Ultimate Strain (με)**	
	Experimental	Manufacturer	Experimental	Manufacturer	Experimental	Manufacturer
10 (#3)	162.6	168	8022	8122	20269	20684
13 (#4)	156.9	167	7621	7977	20588	20935
16 (#5)	N/A	162	7778	7541	N/A	21482

Table 3.1. Mechanical Properties of BFRP Bars

3.1.2 Lightweight Concrete (LWC)

Lightweight concrete is characterized by its reduced self-weight and high strength-to-weight ratio, which justifies the additional cost compared to NWC. Its application is most beneficial in structures where self-weight of the structural elements constitutes a significant portion of the total loads, such as bridge decks and bridge girders. Despite the fact that all major codes nowadays include guidelines for the structural design of LWC members, Lim et al. (2006) pointed out that these guidelines originated either from research done five decades ago, or

unpublished work that is not available to the public. The use of LWC is limited due to the shortage in understanding its structural performance and the inadequacy of design guidelines supported by recent research. The research conducted by Ovitigala and Issa (2012) is the only available work for LWC flexural members reinforced with FRP bars. Both LWC and FRP material are brittle compared to NWC and steel.

The LWC used in the current work utilizes "Water–Cooled Expanded Blast Furnace Slag" as lightweight aggregate. The concrete had a water to cementitious materials ratio of 0.47 and required the use of both normal and high-range water-reducing admixtures, especially with the use of slag in a ratio of 22.5% of the total weight of cementitious materials. The mix proportions are detailed in Table 3.2. Air-entraining admixture was also added to the mix to simulate the requirements of bridge decks. The unit weight of the fresh mix was 126 lb/ft^3, while its slump and air-content were 8 in. and 7.25%, respectively.

Ingredient	**Units**	**Quantity**
Type I Cement	lb/yd^3	520.0
Lightweight Coarse Aggregate	lb/yd^3	746.7
Fine Aggregate	lb/yd^3	1587.3
Slag	lb/yd^3	148.3
Potable Water	lb/yd^3	314.0
Air-Entraining Admixture (MB-AE90)	oz	2.17
Normal-Range Water-Reducing Admixture (Pozzolith 80)	oz	20.01
High-Range Water-Reducing Admixture (PS1583)	oz	20.01
Water/Cementitious Materials	-	*0.47*

Table 3.2. Mix Proportions of Lightweight Concrete

At the day of casting, 6 x 12 in. concrete cylinders were cast to measure the compressive and splitting tensile strengths using ASTM C39 and ASTM C496, respectively. In addition, 6 x 6 x

21 in. prisms were cast to measure the flexural strength of the LWC according to ASTM C78. Figure 3.1 shows the preparation of the specimens while the three tests are shown in Figure 3.2 to 3.4.

Specimen Age	ASTM C39				ASTM C 78			ASTM C496		
	Compressive Strength of Cylindrical Concrete Specimens (psi)				Flexural Strength of Concrete Beams (psi)			Splitting Tensile Strength of Cylindrical (psi)		
	Spec. 1	Spec. 2	Spec. 3	Avg.	Spec. 1	Spec. 2	Avg.	Spec. 1	Spec. 2	Avg.
3 Days	3350	3250	3490	3363	488	542	515	344	300	322
7 Days	4410	4380	4450	4413	617	587	602	401	386	393
14 Days	5330	5350	5360	5347	701	667	684	504	495	499

Table 3.3. Compressive, Flexural and Splitting Tensile Strength of the LWC Mix

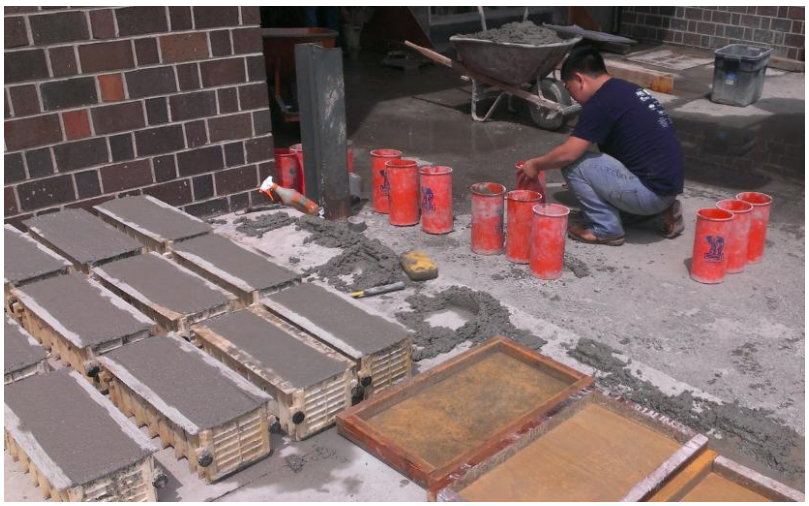

Figure 3.1. Casting the Cylindrical and Prism Specimens

Figure 3.2. Compressive Strength Test (ASTM C39)

Figure 3.3. Splitting Tensile Strength Test (ASTM C496)

Figure 3.4. Flexural Strength Test of Concrete Beams (ASTM C78)

In addition, the static modulus of elasticity was measured for three specimens according to ASTM C469 using the compressometer fixture shown in Figure 3.5. The test yielded a Young's modulus of elasticity of 3,480 ksi at 40% of the ultimate compressive strength corresponding to 5500 psi being the minimum of three tests. The stress-strain plot for the specimen is displayed in Figure 3.6. The failure was brittle at the ultimate stress, as expected for high strength LWC.

Figure 3.5. Modulus of Elasticity Test Fixture - ASTM C469

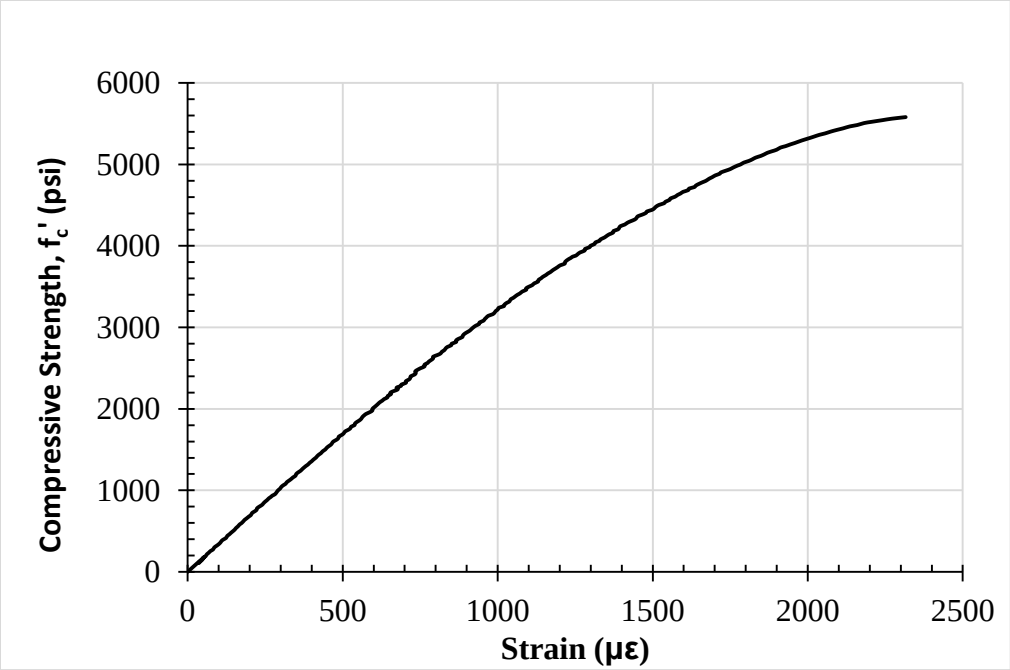

Figure 3.6 Stress-Strain Relationship for LWC (ASTM C469)

3.2 Fabrication

3.2.1 Formworks

The study comprised of testing four LWC slabs to simulate their application in bridge decks using different reinforcement ratios for simply supported and two 2-span continuous slabs all with 18 x 8 in. cross section. The fabrication of the simply supported slabs required two 18 x 8 x 92 in. forms to accommodate a testing span of 6.67 ft. (80 in.). Their bottom reinforcement consisted of 5 BFRP bars of diameter 0.625 in. (16 mm) and 5 BFRP bars of diameter 0.5 in (13mm), respectively. The design ratios of the bottom to the balanced reinforcement areas (ρ_f/ρ_b) were 4.1 and 2.6, respectively. Top reinforcement consisted of 5 BFRP bars of 0.375 in. (10 mm) diameter for both specimens. At each end of the forms, 7-#3 U-shape steel stirrups were installed at 4" spacing to cover a distance of 2 ft., projected from support located 6 in. from the edge of the specimen. One stirrup was also placed in the center of the specimen to provide support for

the top reinforcement. Additionally, both specimens had secondary distribution reinforcement of 0.5 in. (13mm) diameter in the transverse direction at 6.5 in. spacing. The complete formworks for specimens SS1 and SS2 are shown in Figure 3.7.

Figure 3.7. Finalized Formworks for Simply Supported Specimens SS1 and SS2

The two continuously supported slabs extended for two spans of 8.67 ft. each, which required a form size of 18 x 8 x 220 in. The two continuous specimens were reinforced with 5 BFRP bars of diameter 0.625 in. (16 mm) and 5 BFRP bars of diameter 0.5 in. (13 mm) at the bottom with a design ratio (ρ_f/ρ_b) of 4.1 and 2.6, respectively. The slabs were reinforced at the top with 6 BFRP bars of 0.625 in. (16 mm) diameter and 6 BFRP bars of 0.5 in (13 mm) diameter, respectively. Secondary distribution reinforcement consisted of 0.5 in. (13mm) diameter bars in the transverse direction at 6.5 in. spacing. At each end of the forms, 5-#3 stirrups were installed

at a 4 in. spacing, followed by 4-#3 spaced at 6 in. center to center. At the middle of the slab, 9 stirrups were installed; one at the center and 4 at the direction of each span, evenly spaced at 4 in. The formwork for specimens CS1 and CS2 are shown in Figure 3.8.

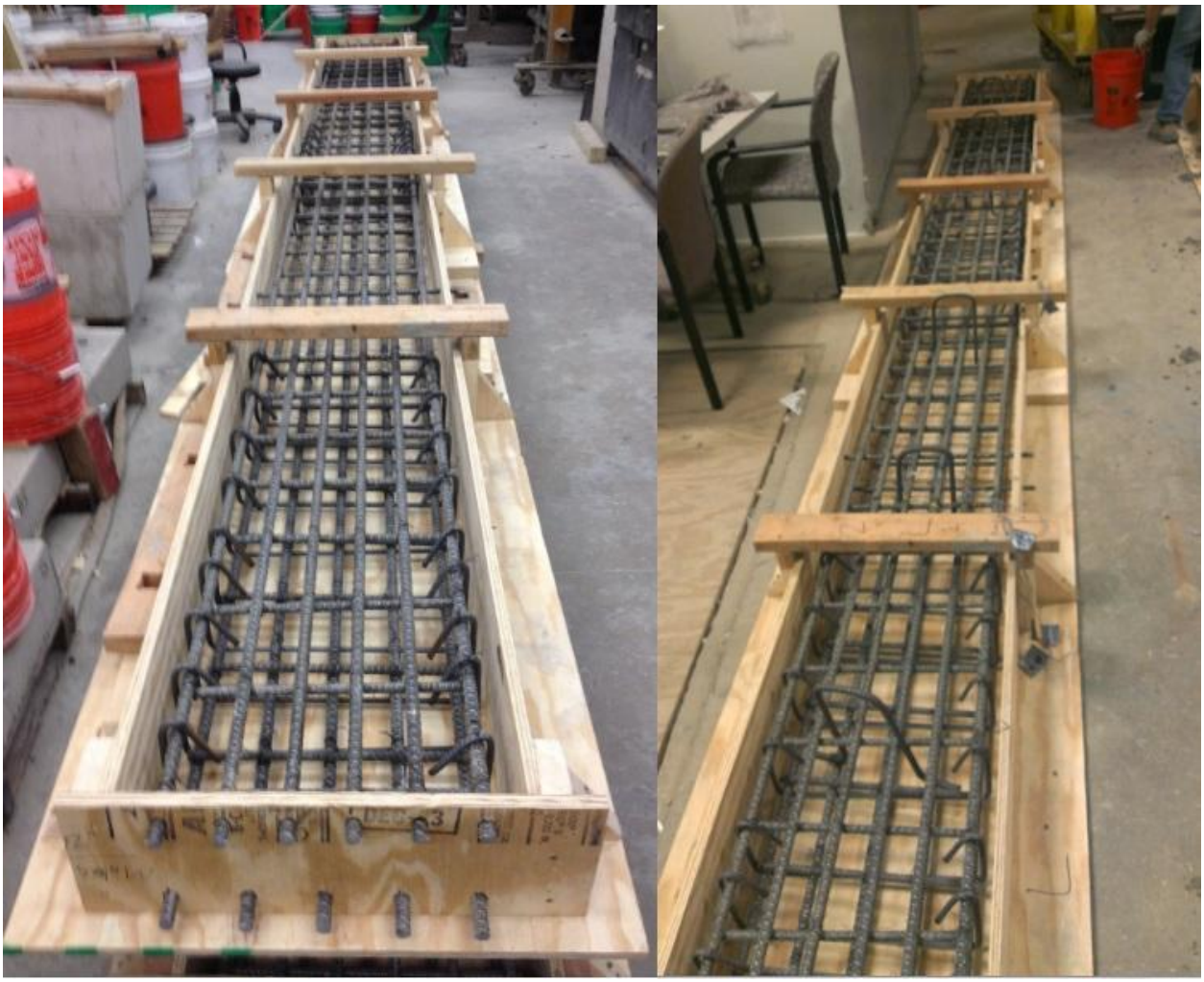

Figure 3.8. Formwork for 2-Span Continuous Slabs CS1 and CS2

The formwork was removed three days after casting the slabs. Curing started few hours after casting using wet burlap covered with plastic sheets. The curing continued until the cylindrical specimens gained a minimum strength of 5500 psi (approximately 2 weeks). The cast slabs are shown in Figure 3.9.

Figure 3.9. Casting of the Slabs

After testing the four slabs, it was possible to test the two separated halves of each continuous slab at 6 and 8 ft spans. Despite their already cracked sections, they were tested for ultimate moment capacity while attaining load-deflection behavior and load-strain relationships for both concrete and BFRP bars.

3.2.2 Strain Gages

The strain gages installed on BFRP rebars were designed and recommended for use on composite materials. Two types were used; BFLA-2-8 and BFLA-5-8. Two different types were also used for concrete, PL-60-11-1L and EP-08-10CBE-120. The installation of the strain gages

on BFRP bars required surface preparation while avoiding excessive reduction in the rebars' cross sectional area. Figure 3.10 shows the process of installing a BFRP strain gage.

(a) Surface Preparation of BFRP Rebar

(b) Bonding the Strain Gage to the Rebar

(c) Protection of Strain Gage with Rubber Tape

Figure 3.10. Installation Process of BFRP Strain Gage

The technical specifications of the four strain gages are listed in Table 3.4.

Material	Strain Gage Type	Gage Factor	Gage Length (mm)	Gage Width (mm)	Overall Length (mm)	Overall Width (mm)	Resistance (Ω)
BFRP Bars	BFLA-2-8	2.09	2	0.9	7.6	2.5	120
	BFLA-5-8	2.10	5	1.5	12.3	3.3	120
Concrete	PL-60-11-1L	2.12	60	1	74	8	120.3
	EP-08-10CBE-120	2.065	25.4	6.35	31.75	6.35	120

Table 3.4. Types of Strain Gages used in the Experimental Program

3.3 Experimental Parameters and Design Procedure

A total of eight BFRP reinforced concrete slabs were tested, each with a different span length and reinforcement. The main experimental parameters were the reinforcement ratio, the number of spans (simply supported versus continuous), and the span length. For the simply supported slabs, the bottom reinforcement to the balanced ratio (ρ_f/ρ_{fb}) varied. Initially, the design was performed to have (ρ_f/ρ_{fb}) equal to 3.9 and 2.6 for the slabs reinforced with 5 #5 and 5 #4 at the bottom, respectively. These values were chosen to satisfy both strength and serviceability requirements; in most cases for the design of FRP flexural members, meeting the deflection limitations is known to satisfy the strength criteria. The two different ratios were selected to study the effect of increasing the reinforcement area on moment capacity and deflection.

Six out of the eight specimens were tested as simply supported with different spans; 6, 6.67 and 8 ft., giving a length to height (L/H) ratio of 9, 10 and 13, respectively. An L/H ratio of 10 is equal to the maximum value for beams, while a ratio of 13 is the maximum permissible limit for one-way solid slabs, as in bridge decks (ACI 440.1R, 2006). The two other slabs were two-span continuous; each span was 8.66 ft. long with an L/H ratio of 10 and a total length of 17.33 ft. The top reinforcement at the middle support, where the maximum moment is expected, was 6 #5 and 6 #4 for the two slabs, and (ρ_f/ρ_{fb}) equaled 5.1 and 3.2, respectively. The details of each bridge deck specimen are listed in Table 3.5 and detailed in Figures 3.11 to 3.13.

Specimen ID		Span Length (ft)	L/H	Bottom Reinforcement			Top Reinforcement		
				BFRP Bars	Area (in.^{2})	ρ_f/ρ_b	BFRP Bars	Area (in.^{2})	ρ_f/ρ_b*
Simply Supported	SS1	6.67	10.0	5 - #5	1.55	4.1	5 - #3	0.55	-
	SS2	6.67	10.0	5 - #4	0.8	2.6	5 - #3	0.55	-
	SS3-CS1	8.0	12.0	5 - #5	1.55	4.1	6 - #5	1.86	-
	SS4-CS2	8.0	12.0	5 - #4	0.8	2.6	6 - #4	0.66	-
	SS5-CS1	6.0	9.0	5 - #5	1.55	4.1	6 - #5	1.86	-
	SS6-CS2	6.0	9.0	5 - #4	0.8	2.6	6 - #4	0.66	-
2-Span Continuous	CS1	8.67 each	13.0	5 - #5	1.55	4.1	6 - #5	1.86	5.1
	CS2	8.67 each	13.0	5 - #4	0.8	2.6	6 - #4	0.66	3.2

* ρ_f/ρ_b for top reinforcement is only considered for the continuous slabs and over the middle support.

Table 3.5. Reinforcement and Span Length Details for Bridge Deck Specimens

The simply supported slabs SS3 to SS6 are followed by a designation to mark which continuous slab they originally belonged to. The length to height ratio (L/H) was equal to 10 for the simply supported slabs SS1 and SS2, and 13 for the continuous slabs CS1 and CS2. The two 8 ft. slabs had an L/H ratio of 12, slightly less than the maximum permissible defined by ACI 440.1R (2006) as 13 for one-way solid slabs.

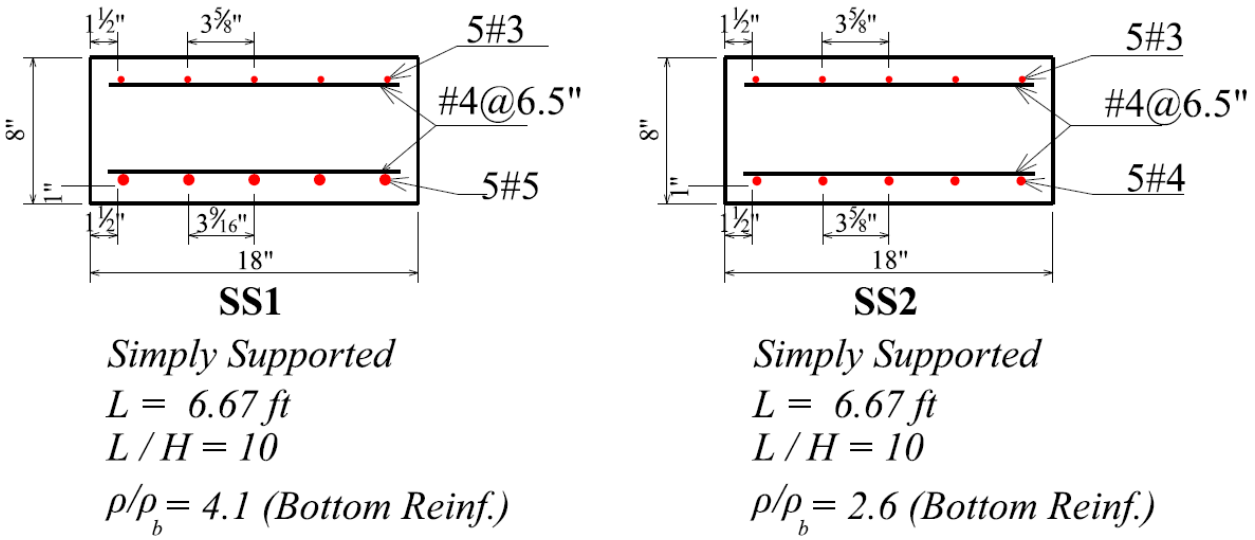

Figure 3.11. Cross-Section and Details for Specimens SS1 and SS2

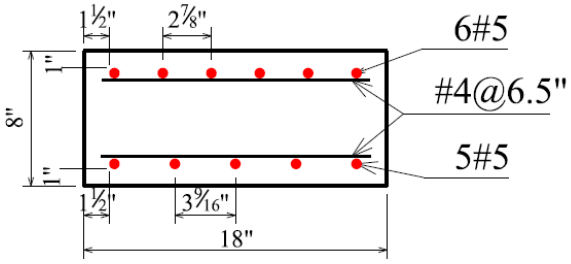

CS1
2-Span Continuous
L = 17.33 ft
L / H = 13
ρ/ρ_b *= 4.1 (Bottom Reinf.)*
ρ'/ρ_b *= 5.1 (Top Reinf.)*

SS3-CS1
Simply Supported
L = 8 ft
L / H = 12
ρ/ρ_b *= 4.1 (Bottom Reinf.)*
ρ'/ρ_b *= 5.1 (Top Reinf.)*

SS5-CS1
Simply Supported
L = 6 ft
L / H = 9
ρ/ρ_b *= 4.1 (Bottom Reinf.)*
ρ'/ρ_b *= 5.1 (Top Reinf.)*

Figure 3.12. Cross-Section and Details for Specimens CS1, SS3-CS1 and SS5-CS1

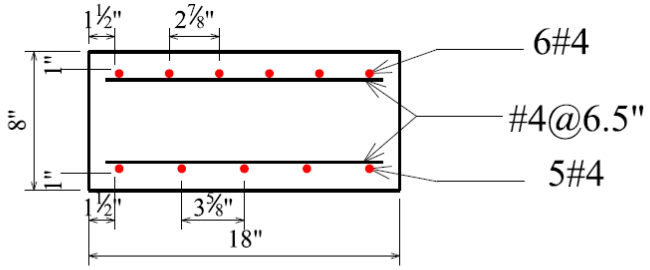

CS2
2-Span Continuous
L = 17.33 ft
L / H = 13
ρ/ρ_b *= 2.6 (Bottom Reinf.)*
ρ'/ρ_b *= 3.2 (Top Reinf.)*

SS4-CS2
Simply Supported
L = 8 ft
L / H = 12
ρ/ρ_b *= 2.6 (Bottom Reinf.)*
ρ'/ρ_b *= 3.2 (Top Reinf.)*

SS6-CS2
Simply Supported
L = 6 ft
L / H = 9
ρ/ρ_b *= 2.6 (Bottom Reinf.)*
ρ'/ρ_b *= 3.2 (Top Reinf.)*

Figure 3.13. Cross-Section and Details for Specimens CS2, SS4-CS2 and SS6-CS2

The design was done according to the equations and procedure in ACI 440.1R (2006) for sections with $\rho_f/\rho_{fb} > 1$, defined as over-reinforced and fail by crushing of concrete. The moment capacity of the section is calculated using equation 3.1 (Eq. 8-4a in ACI 440.1R (2006))

$$M_n = A_f f_f \left(d - \frac{a}{2}\right) \qquad Eq.\ 3.1$$

$$where\ a = \frac{A_f f_f}{0.85 f_c' b} \qquad Eq.3.2a$$

$$and\ f_f = E_f \varepsilon_{cu} \frac{(\beta_1 d - a)}{a} \qquad Eq.3.2b$$

Substituting Eq. 3.2a into 3.2b gives Eq. 3.2c to calculate the stress in the BFRP bars and ensure that it doesn't exceed the design tensile stress.

$$f_f = \sqrt{\frac{\left(E_f \varepsilon_{cu}\right)^2}{4} + \frac{0.85\beta_1 f_c'}{\rho_f} E_f \varepsilon_{cu}} - 0.5 E_f \varepsilon_{cu} \leq f_{fu} \qquad Eq.3.2c$$

The ultimate moment capacity (M_u) is then calculated by multiplying the nominal capacity by a strength reduction factor, ($M_u = \emptyset M_n$) and (ϕ) is found as follows:

$\phi = 0.55$ if $\rho_f < \rho_{fb}$,

$\phi = 0.65$ if $\rho_f > 1.4\,\rho_{fb}$

$\phi = 0.3 + 0.25\,{\rho_f}/{\rho_{fb}}$ when $\rho_{fb} < \rho_f < 1.4\,\rho_{fb}$

$$where \qquad \rho_{fb} = 0.85\beta_1 \frac{f_c'}{f_{fu}} \frac{E_f \varepsilon_{cu}}{E_f \varepsilon_{cu} + f_{fu}} \qquad Eq.3.2$$

For members designed to fail by rupture of FRP bars, ACI 440.1R (2006) lowers the strength reduction factor because the failure is considered more catastrophic than crushing of concrete.

A sample calculation for Slab SS2 is shown in the following spreadsheet.

Concrete Properties

f_c' =	5500	psi	Compressive Strength of Concrete
E_c =	3461395	psi	Modulus of Elasticity for Concrete
ε_{cu} =	3000	με	Ultimate Strain of Concrete
γ_c =	126	pcf	Unit Weight of Concrete
f_r =	556	psi	Modulus of Rupture
β_1 =	0.775		Factor relating depth of equivalent rectangular compressive stress block to neutral axis

BFRP Properties

f_{fu} =	150000	psi	Ultimate Tensile Strength for BFRP Bars
E_f =	7260000	psi	Modulus of Elasticity for BFRP Bars
ε_{fu} =	20000	με	Ultimate Strain of BFRP Bars

Bridge Deck Strip Dimensions

b =	18	in	Beam Width
h =	8	in	Beam Height
L =	6.67	ft	Span Length
L / h =	10.00		**Span to Depth Ratio within ACI Limits**

Reinforcement

Size #	4	Imperial	Size of Rebar
# of Rebars	5	#	Total Number of Reinforcement Rebars
# of Layers	1		
d_b	0.50	in	Nominal Diameter of Reinforcement
A_b	0.20	in^2	Nominal Area of Rebar
A_f	1.00	in^2	Area of BFRP Reinforcement Provided
Side Cover	1.5	in	Clear Cover from the sides
c_c **(bottom)**	1	in	Clear Cover from the bottom

Moment Capacity

d	6.75	in	Effective Depth
ρ_{fb}	0.00315		BFRP Balanced Reinforcement Ratio
ρ_f	0.00818		Provided Ratio of Reinforcement
A_{fb} =	0.38	in^2	Area of Balanced FRP Reinforcement
ρ_f / ρ_{fb}	2.6		**Ratio Larger than 1.4, OK**
a (in)	1.0	in	Depth of equivalent rectangular stress block
f_f	87924	psi	Stress in FRP Reinforcement in tension
M_n	45.4	kips.ft	Nominal Moment Capacty
ϕ	0.650		Strength Reduction Factor (ACI 440.1R)
ϕM_n	29	kips.ft	Moment Capacity

Table 3.6 displays the calculated nominal and ultimate moment capacities for each specimen.

Specimen ID	ACI Predicted Nominal Moment "M_n" (kip.ft)	ACI Predicted Ultimate Moment "M_u" (kip.ft)
SS1	53.40	34.7
SS2	45.40	29.5
SS3-CS1	53.40	34.7
SS4-CS2	45.40	29.5
SS5-CS1	53.40	34.7
SS6-CS2	45.40	29.5
CS1	58.10	37.8
CS2	49.60	32.2

Table 3.6. Nominal and Ultimate Moment Capacities for the Slabs

3.4 Experimental Setup

3.4.1 Simply Supported BFRP Reinforced Slabs

The simply supported specimens were set up on two steel rollers, one was prevented from rolling by a locking bolt. Both were supported on W 14 x 90 steel beams bolted to a steel bed. The load was applied in the middle of the span using a hydraulic actuator attached to a load cell, and on a 20 x 8 x 1.5 in. steel plate resting on a HDPE plate of similar size to distribute the load evenly on the concrete surface. The surface area of the steel and HDPE plates represents the contact area of two tires of a HL-93 truck according to AASHTO LRFD specifications. The testing setup for all simply supported slabs is sketched in Figure 3.14 and pictured in Figure 3.15.

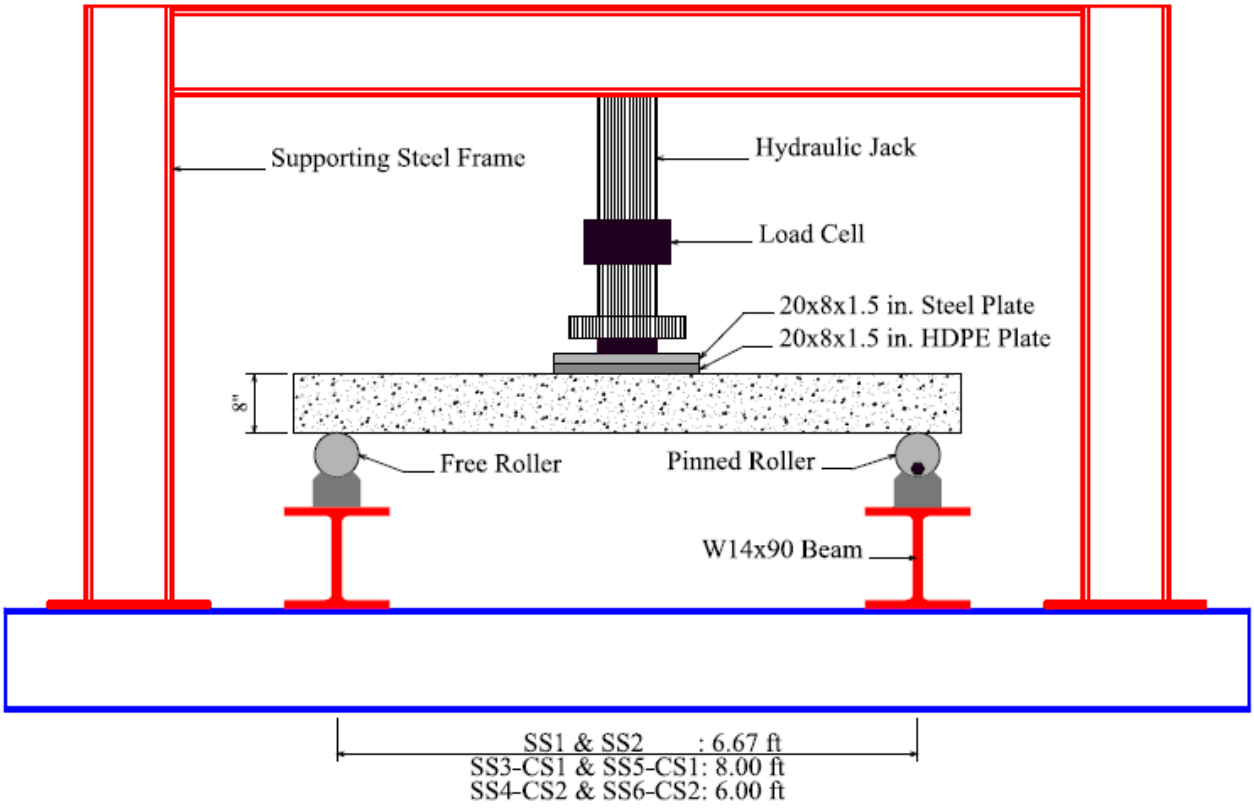

Figure 3.14. Testing Setup for Simply Supported Specimens

Figure 3.15. Laboratory Setup for Simply Supported Slabs

Slabs SS1 and SS2 had three and two bottom BFRP strain gages at the midspan, respectively, in addition to two top BFRP strain gages at the midspan for both specimens. At the top surface of the concrete, two strain gages and two horizontal linear variable differential transformers (LVDTs) were installed to measure the strain of concrete in compression at midspan. Two other horizontal LVDTs were located at the bottom surface of the midspan to measure the strain of the

concrete in tension. The maximum vertical deflection was obtained using a vertical LVDT installed at the midspan. Figure 3.16 displays the instruments installed for slabs SS1 and SS2.

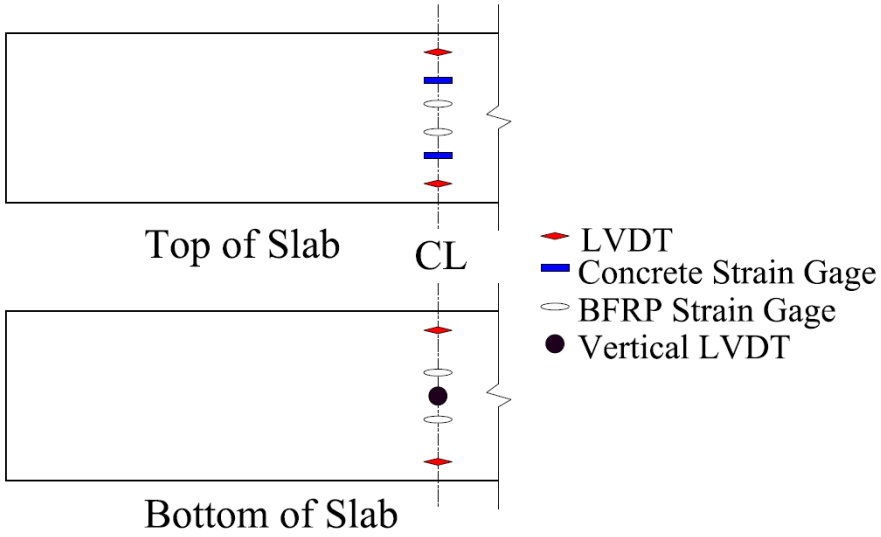

Figure 3.16. Instruments for Specimens SS1 and SS2

Slabs SS3-CS1 and SS5-CS1 were tested at 8 and 6 ft. spans, respectively, and utilized the BFRP rebar strain gages that were already installed on specimen CS1, but offset from the center by 7.25 and 19 in., respectively. Two LVDTs were installed horizontally on the top surface of the midspan to measure the strain of concrete in compression, in addition to one vertical LVDT to measure the deflection at the midspan. The instrumentation for both slabs is detailed in Figure3.17. Similarly, specimens SS4-CS2 and SS6-CS2 were tested at 8 and 6 ft. spans, respectively, and utilized the BFRP rebar and concrete strain gages that were already installed on specimen CS2, but offset from the center by 7.25 and 19 in., respectively. Two LVDTs were installed horizontally on the top surface of the midspan to measure the strain of concrete in compression, in addition to one vertical LVDT to measure the deflection. SS4-CS2 had two extra concrete strain gages at the compression face located 23 in. from the center of the span. The location of instruments are shown in Figure 3.18.

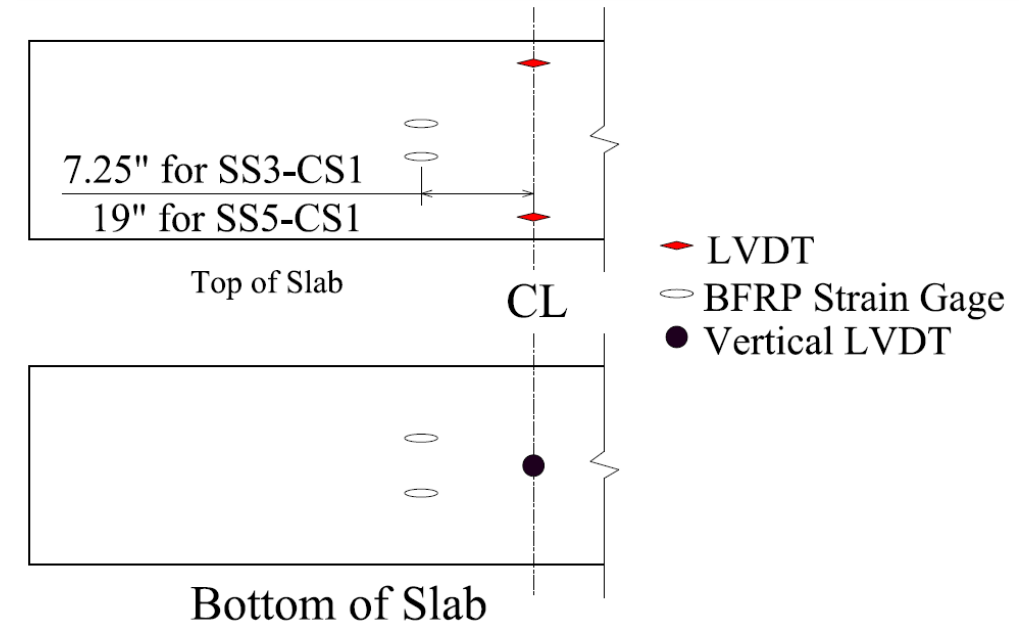

Figure 3.17. Instruments for Specimens SS3-CS1 and SS5-CS1

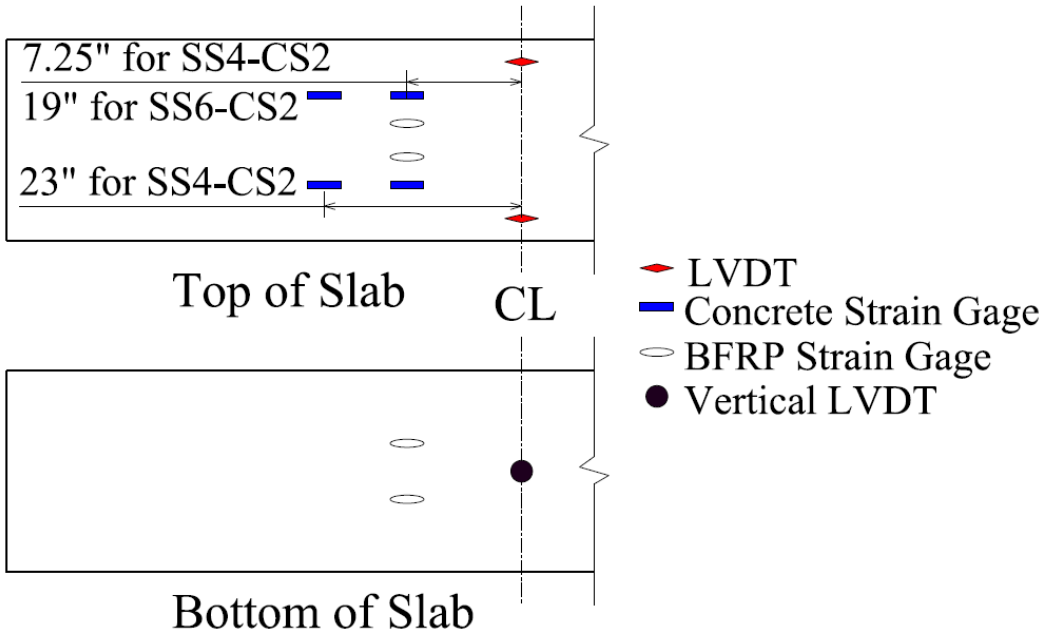

Figure 3.18. Instruments for Specimens SS4-CS2 and SS6-CS2

3.4.2 Two-Span Continuous BFRP Reinforced Slabs

The two continuous specimens had two equal spans of 8.67 ft. and were supported on two free rollers at the edges, fixed on W 14 X 90 steel beams that are bolted to the steel bed. The middle support was another W-shape beam with rigid HDPE plates. The load was applied via a hydraulic actuator located right above the middle support, and attached to spreader beam to apply the load at two points 6 ft. apart; each 3 ft. away from the mid-support. The 6 ft. distance represents the width of the HL-93 truck axle. The spreader beam distributed the load at both sides on 20 x 8 x 1.5 in. steel plate resting on a similarly sized HDPE plate, which represents the contact area of HL-93 truck tires. The testing setup is sketched in Figure 3.19 and pictured in Figure 3.20.

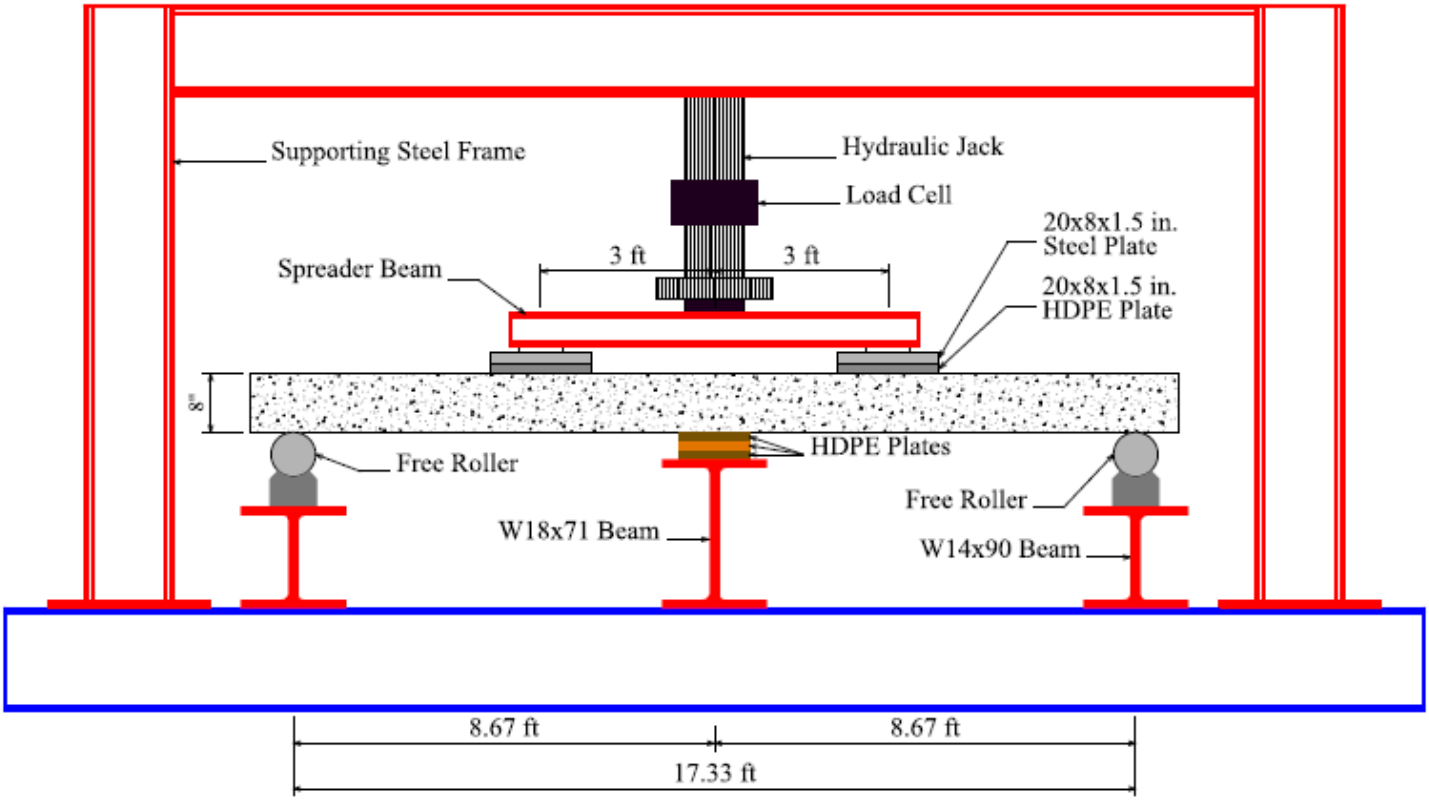

Figure 3.19. Testing Setup for 2-Span Continuous Slabs, CS1 and CS2

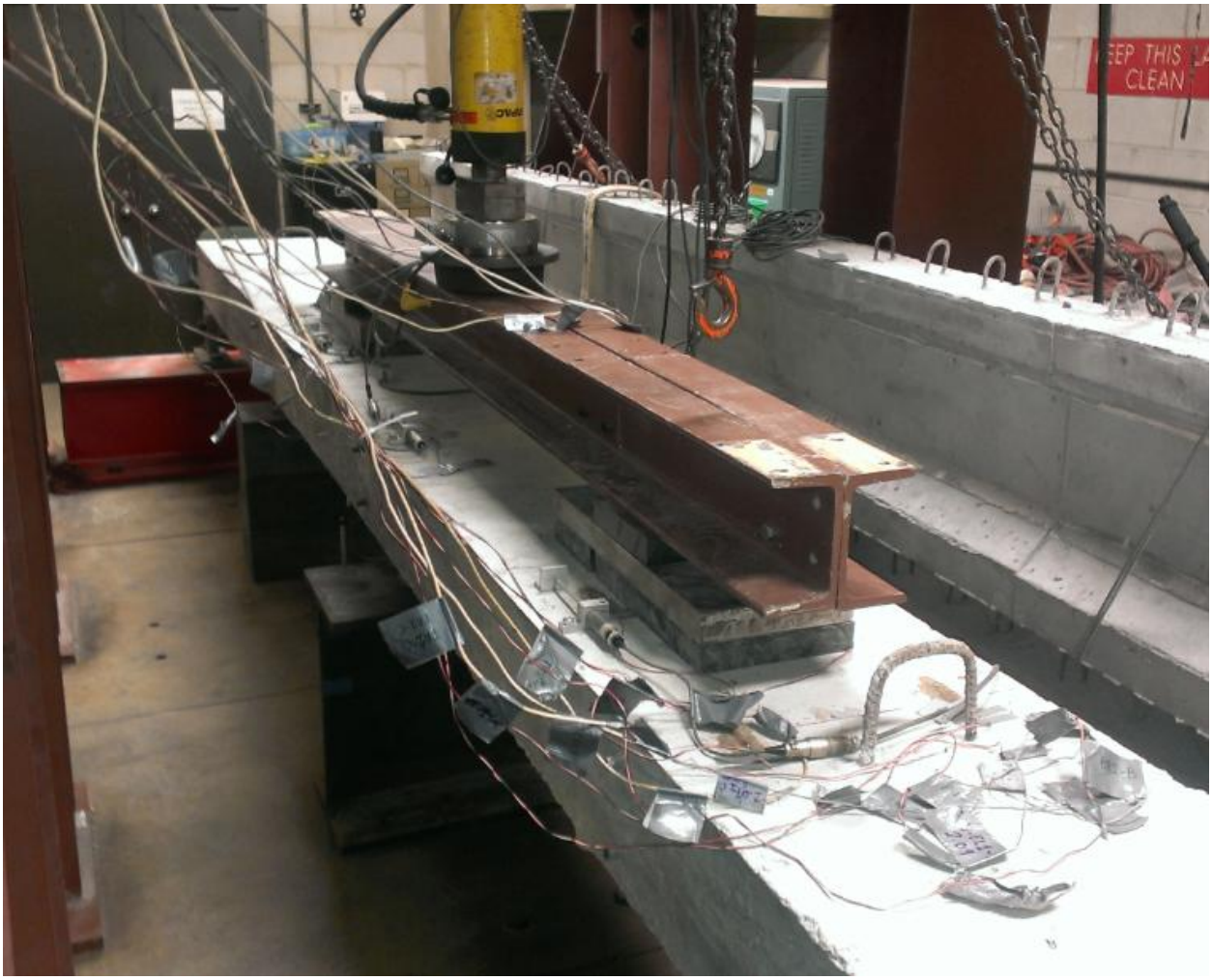

Figure 3.20. Laboratory Setup for Testing Continuous Slabs CS1 and CS2

Each of the continuous slab specimens, CS1 and CS2, had a total of twelve strain gages installed on the BFRP reinforcement; four at the middle of each span and four at the mid-support. Each set of 4 consisted of two strain gages at the bottom bars, and two at the top to measure the tensile and compressive strain at each location. For concrete, ten strain gages were installed at the top surface of each slab and in five locations; the middle and load location of each span, and at the mid-support (two strain gages at each location). In addition, one horizontal strain gage was installed at the top surface in three locations; each point load position and the mid-support. Two other horizontal LVDTs were installed on the bottom surface at the location of mid-support to

capture the strain of concrete in compression, where the failure is expected to occur. The maximum deflection was measured for each span by installing a vertical LVDT at a distance of 58 in. from the mid-support in each direction. This exact location was attained by structural analysis prior the testing. Figure 3.21 presents the details and location of all 29 instruments, all of which were connected to the data logger shown in Figure 3.22. A sample of the instruments used during the tests are shown in Figures 3.23 and 3.24.

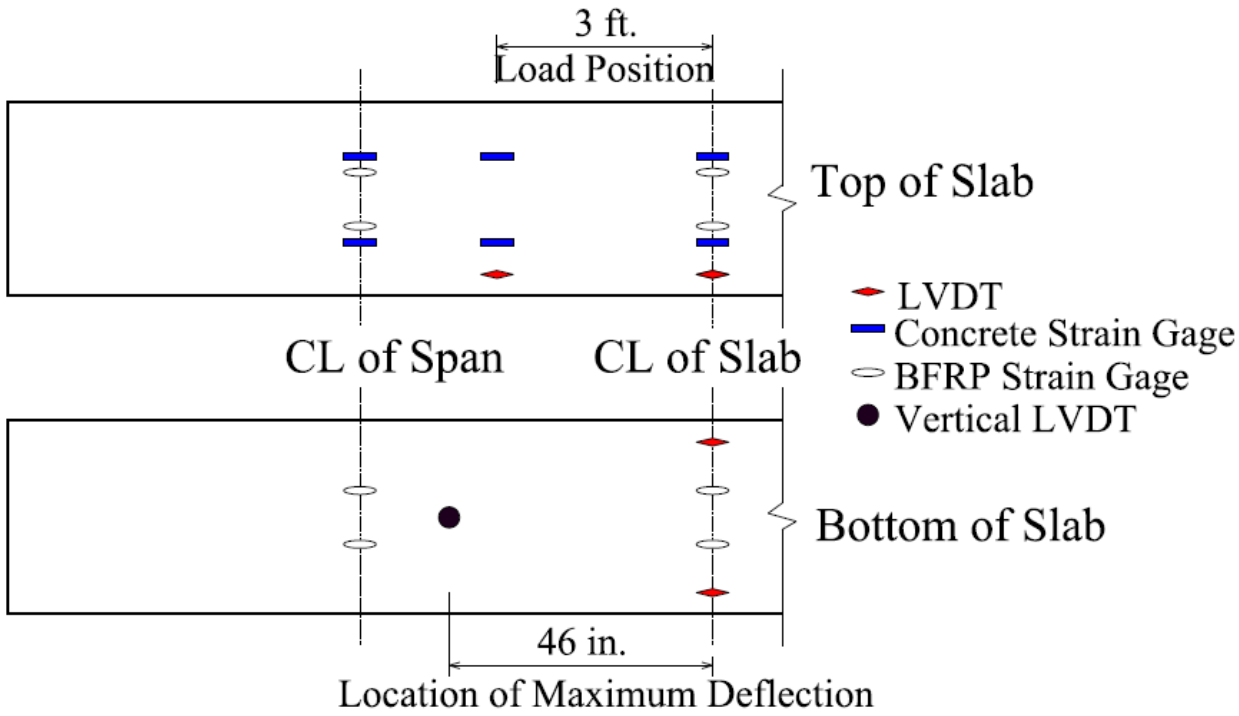

Figure 3.21. Instrumentation for Slabs CS1 and CS2

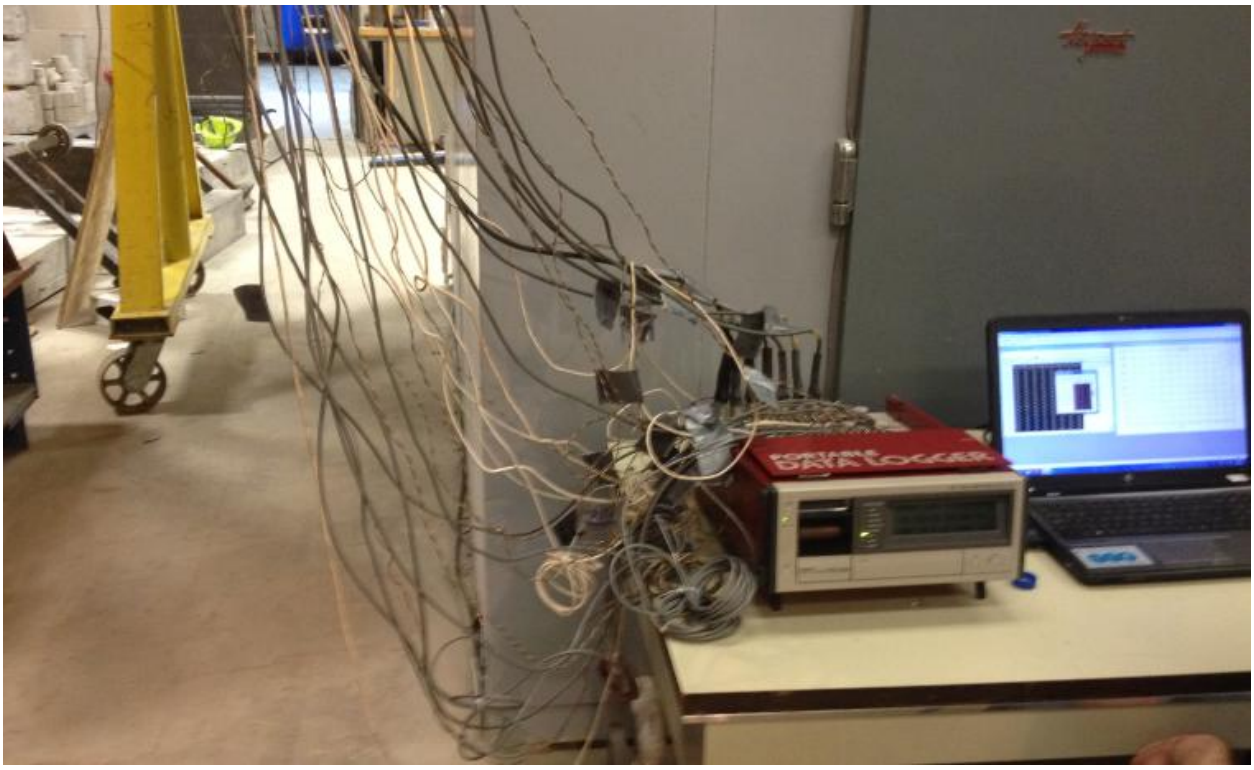

Figure 3.22. Data Logger and Recording System

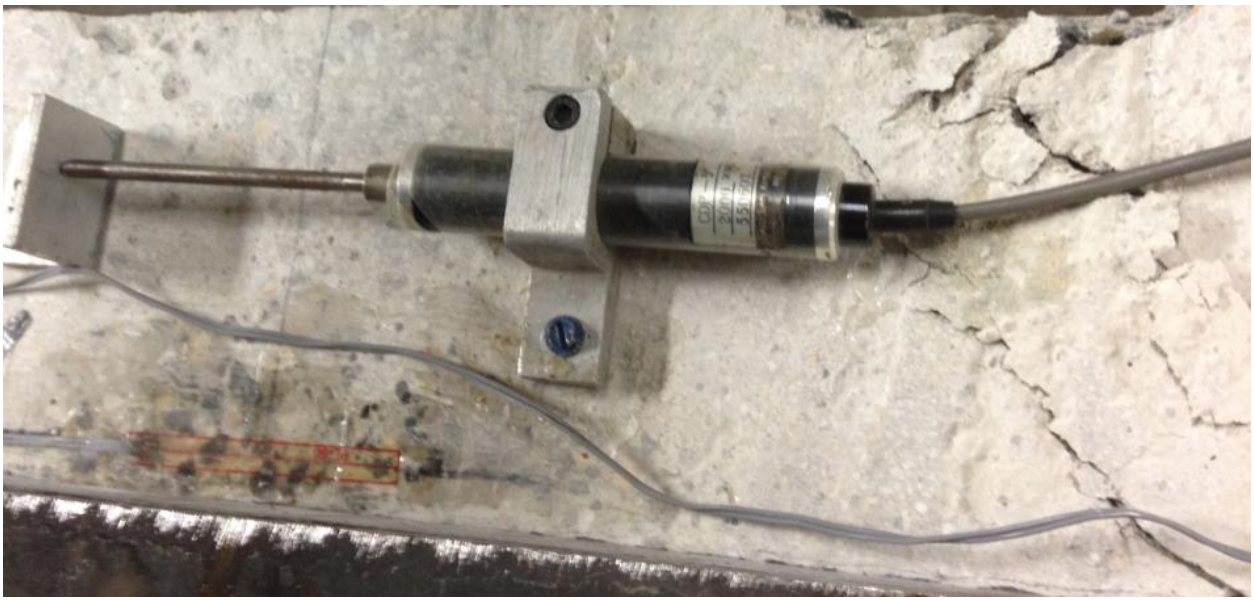

Figure 3.23. Strain Gage and Horizontal LVDT to Measure the Compressive Strain in Concrete

Figure 3.24. Vertical LVDT for Deflection Measurement and Horizontal LVDT to Measure the Tensile Strain in Concrete

CHAPTER 4
EXPERIMENTAL RESULTS

This Chapter presents the experimental results for the simply supported slabs and two-span continuous slabs in two sections. The discussion and analysis of these results are deliberated in the chapters to follow.

4.1 Simply Supported BFRP Reinforced Slabs

A total of six simply supported specimens were tested until failure by three-point bending mode. The first two specimens, SS1 and SS2 were designed with (ρ_f/ρ_{fb}) greater than 1 so that the mode of failure would be the crushing of concrete, rather than rupture of BFRP bars. However, the steel stirrups at both ends prevented a very early shear failure from occurring first. Both slabs exhibited flexural shear failure. Vertical flexural cracks started to occur at the center region after exceeding the cracking load. As the load increased, crack initiation moved outwards to the sides in a larger spacing than that for cracks in the center. Finally, shear cracks were generated at the ends of the slab, while flexural cracks propagated further. Finally cracks extended in an inclination until failure occurred, causing flexural shear failure. No horizontal cracks were observed at the level of the bottom reinforcement, which indicates that bonding failure did not occur. The maximum applied load for slabs SS1 and SS2 was 36.61 and 36.14 kips, which corresponds to moments of 61.02 and 60.24 kip.ft, respectively. The equal experimental capacities confirm that both specimens, although reinforced differently, failed due to flexural shear. The experimental cracking load of 5.85 and 5.74 kips for specimens SS1 and SS2 was almost equal to the predicted moment of 5.33 kips. The experimental value is slightly higher because it depends on the bare-eye observation of the first initiated crack. Smaller and narrower

cracks could have initiated earlier without being seen. The deflection at maximum load reached 1.22 in. for SS1 and 1.75 in. for SS2. These results revealed that a 150% increase in the reinforcement area in SS1 (1.55 in^2) compared to SS2 (1.0 in^2) lowered the deflection by 30% at ultimate.

Figure 4.1. Flexural Shear Failure of Specimen SS1

The flexural shear failure cracks shown in Figure 4.1 occurred on the other side too, simultaneously. In Figure 4.2, the first cracking load is marked as 5.7 kips.

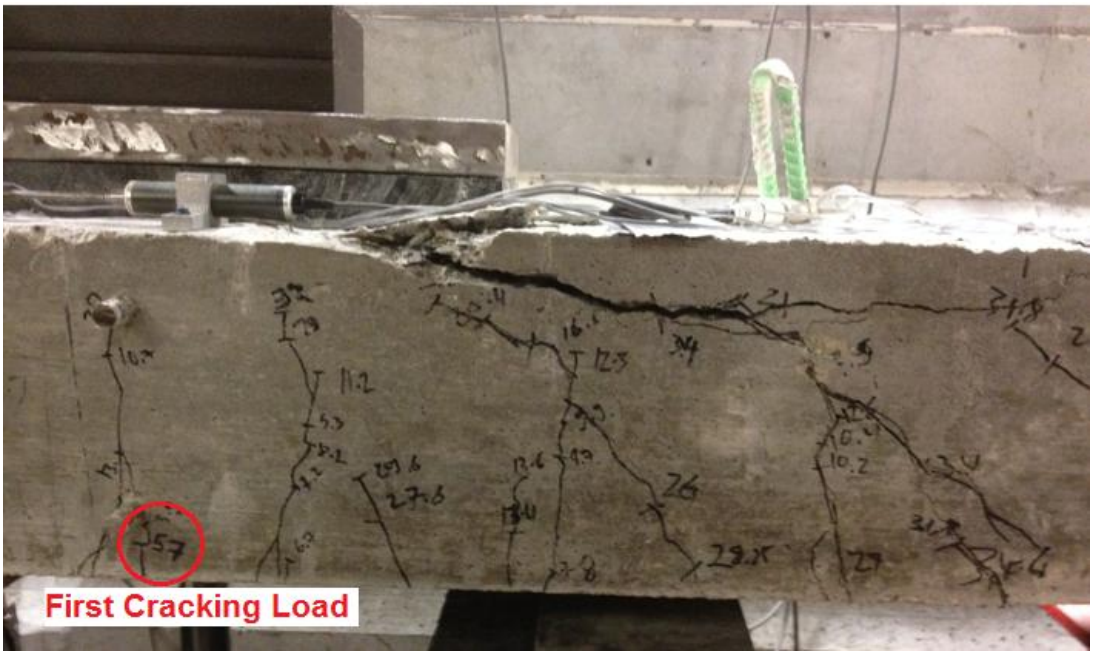

Figure 4.2. (a) Flexural Shear Failure of Specimen SS2

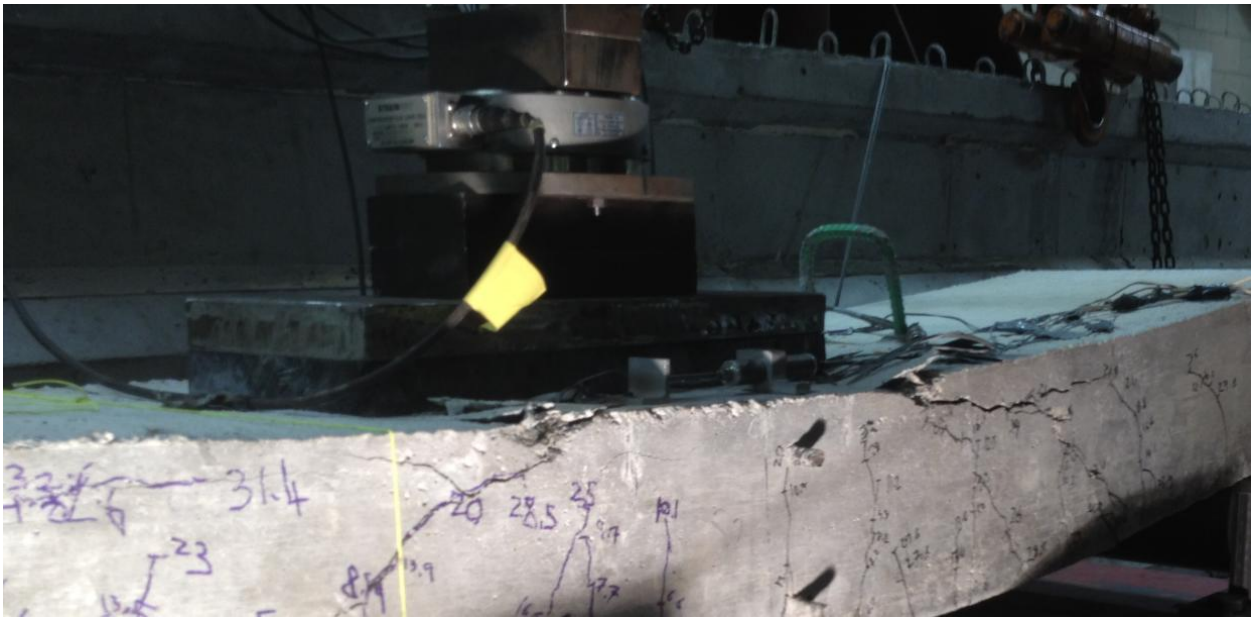

Figure 4.2 (a). Crack Mapping for Specimen SS2

The load-deflection curve, load-strain curve for bottom BFRP reinforcement, concrete in compression load-strain curve and concrete in tension load-strain curve for specimens SS1 and SS2 are shown in Figures 4.3 to 4.10.

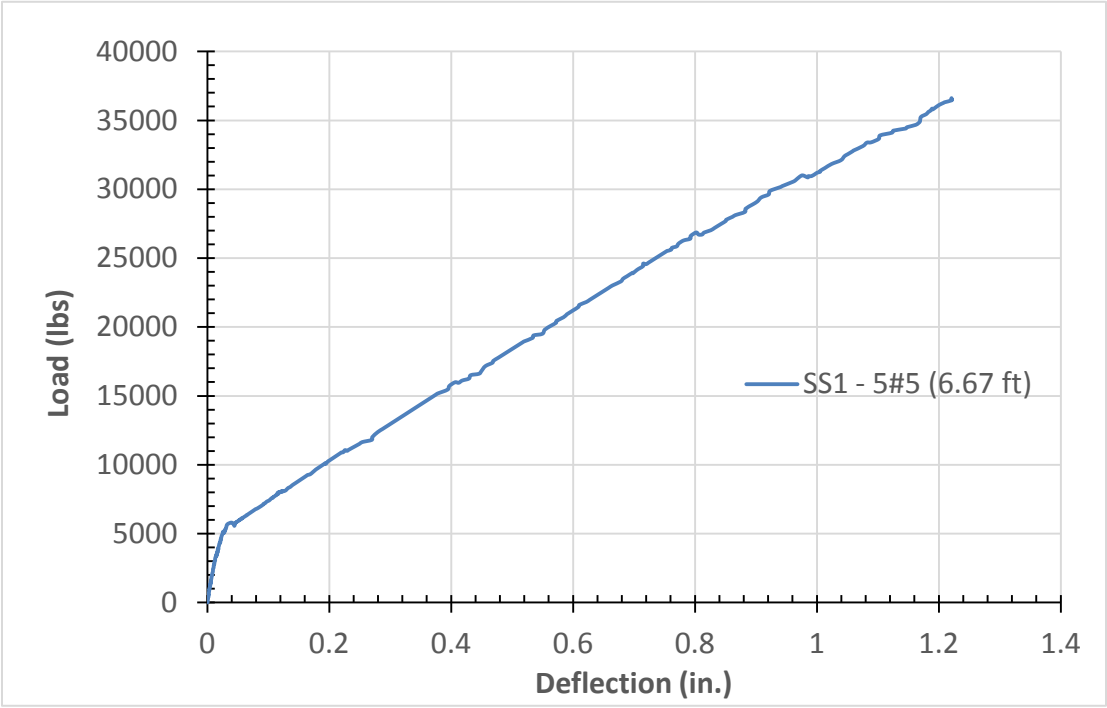

Figure 4.3. Load-Deflection Curve for Specimen SS1

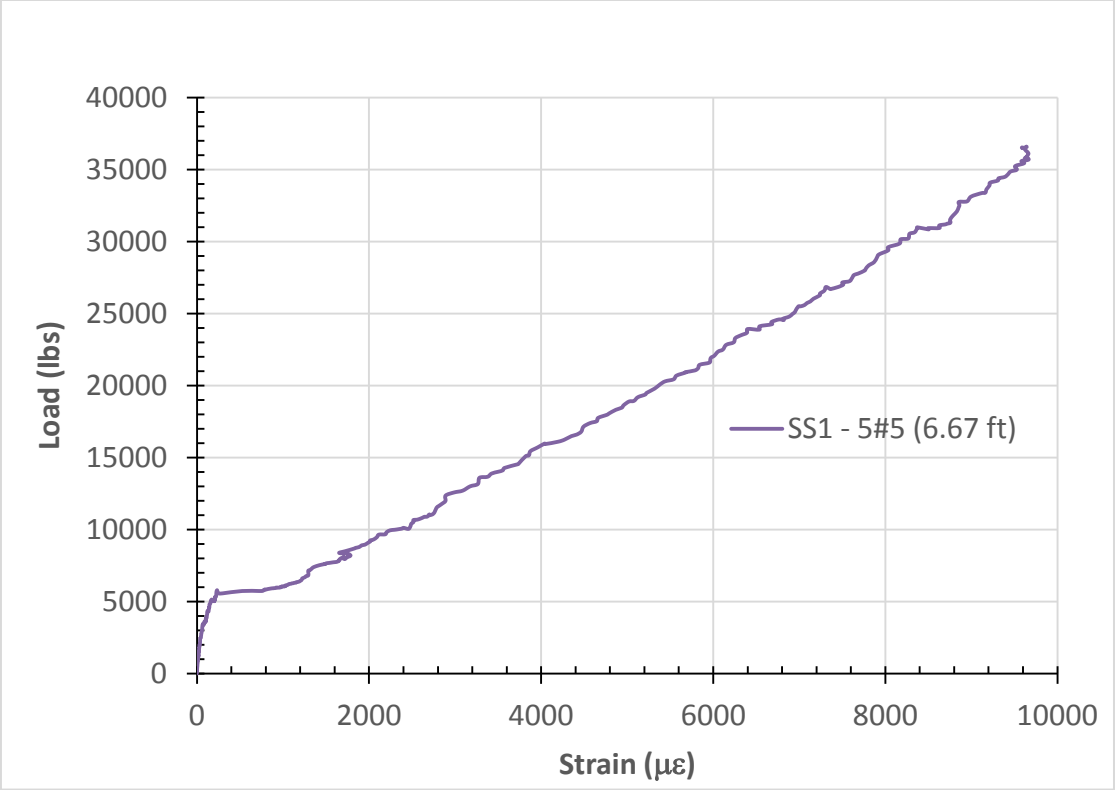

Figure 4.4. Load-Strain Curve for Bottom Reinforcement - Specimen SS1

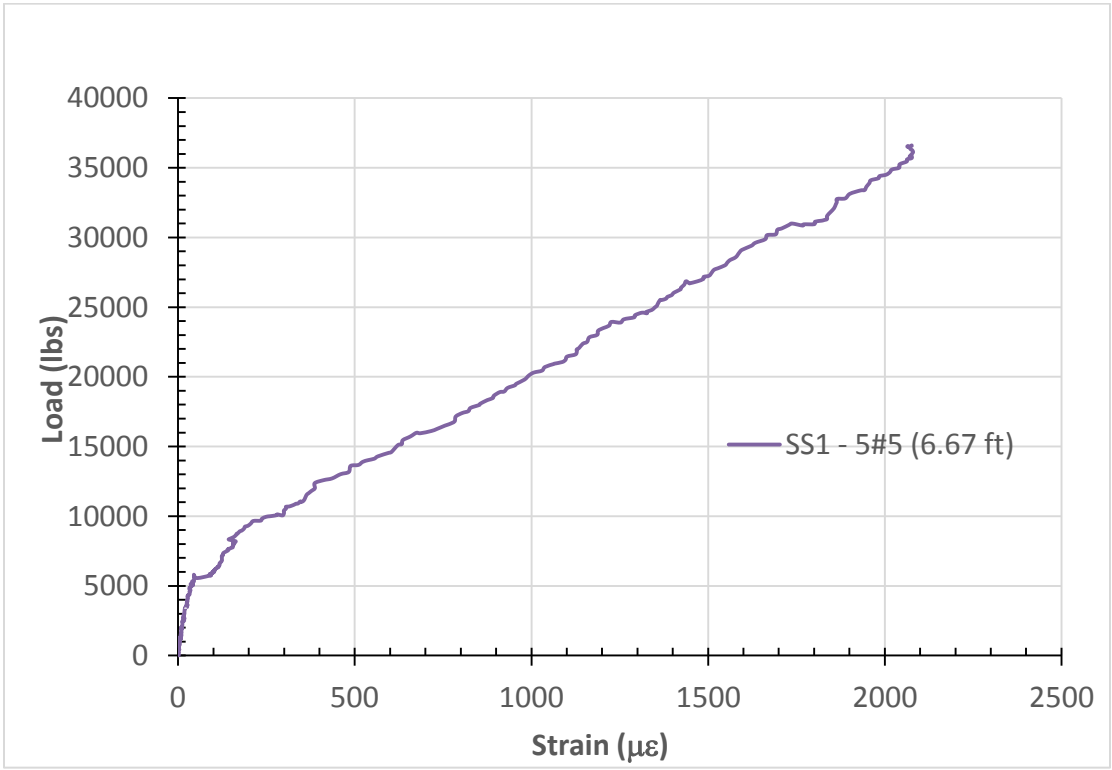

Figure 4.5. Load-Strain Curve for Concrete in Compression - Specimen SS1

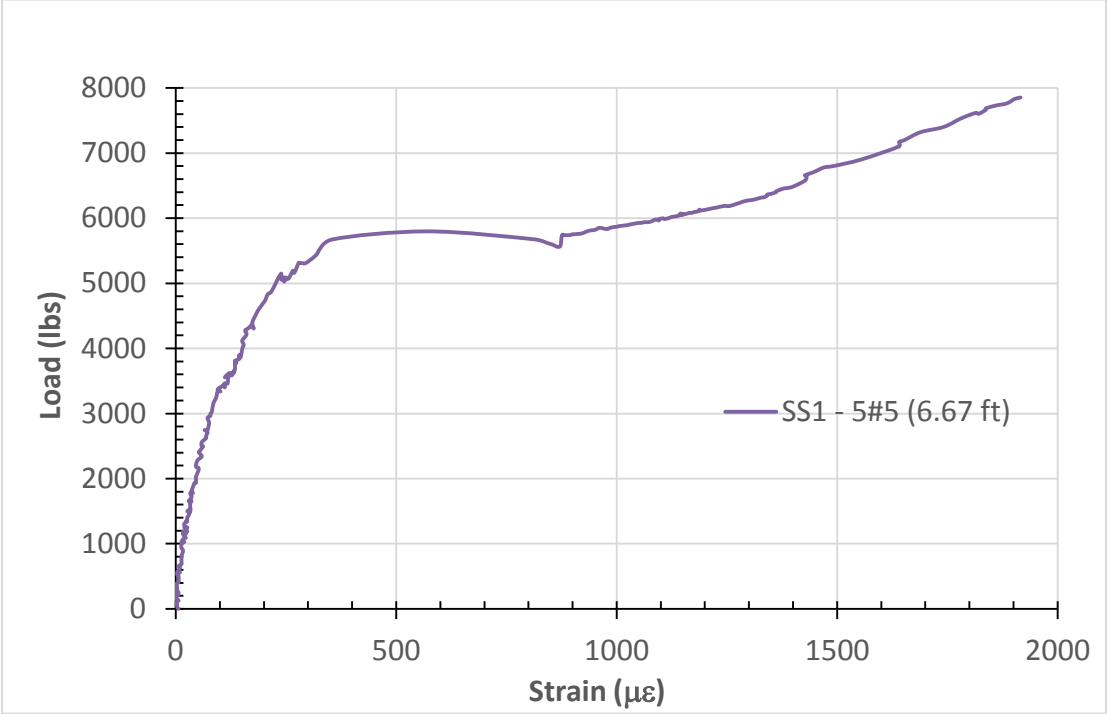

Figure 4.6. Load-Strain Curve for Concrete in Tension - Specimen SS1

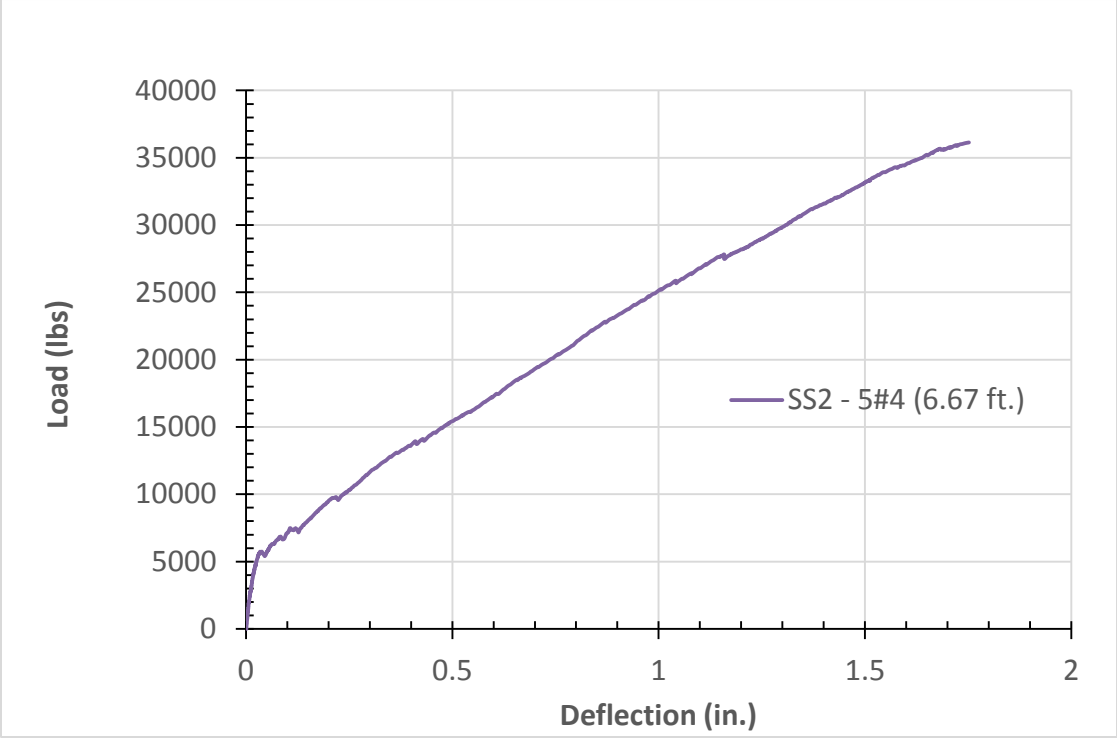

Figure 4.7. Load-Deflection Curve for Specimen SS2

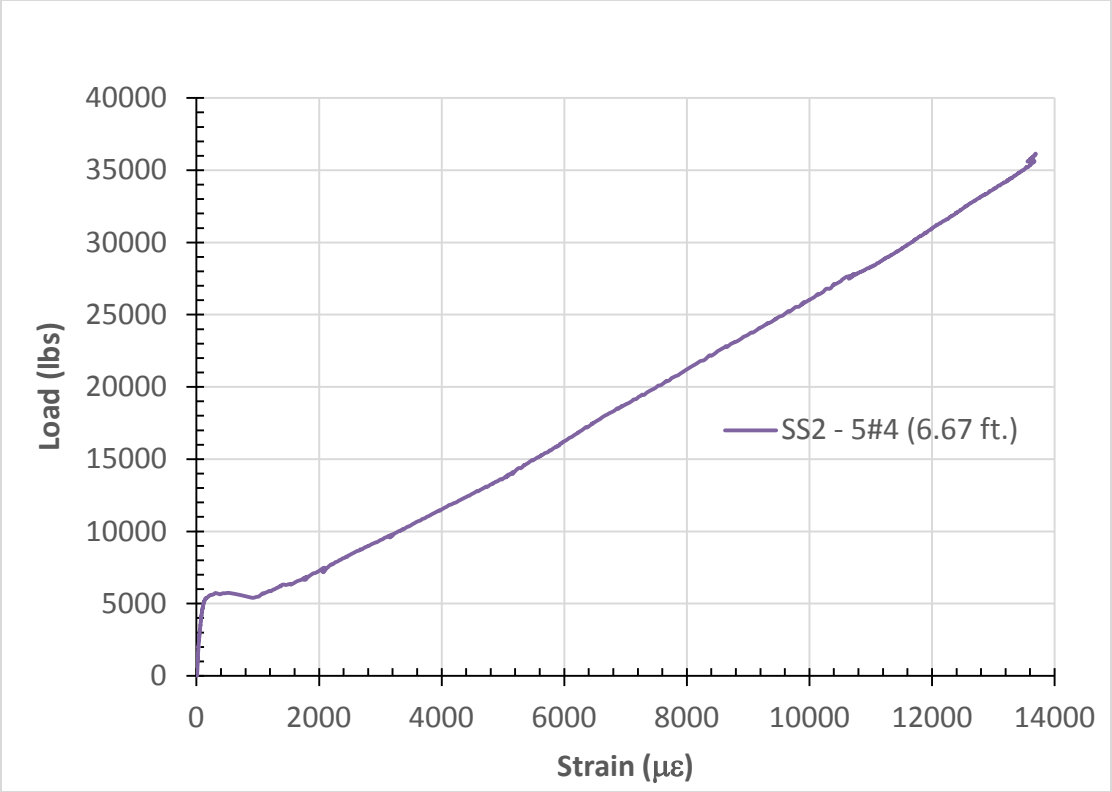

Figure 4.8. Load-Strain Curve for Bottom Reinforcement - Specimen SS2

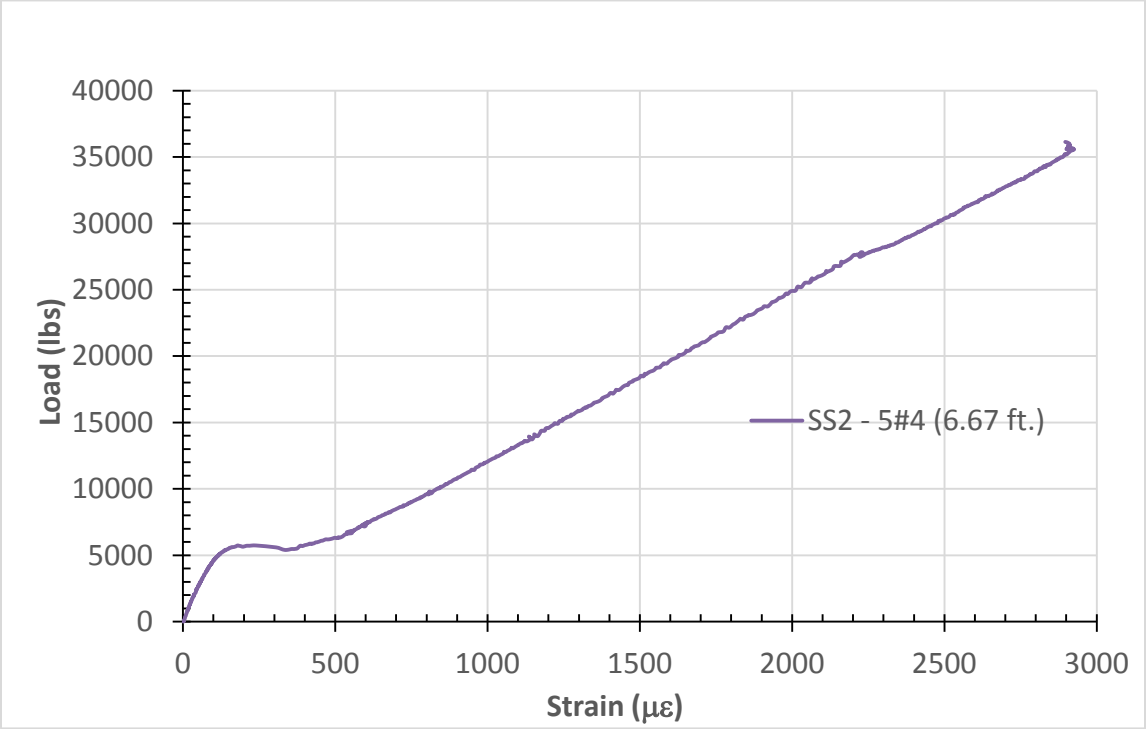

Figure 4.9. Load-Strain Curve for Concrete in Compression - Specimen SS2

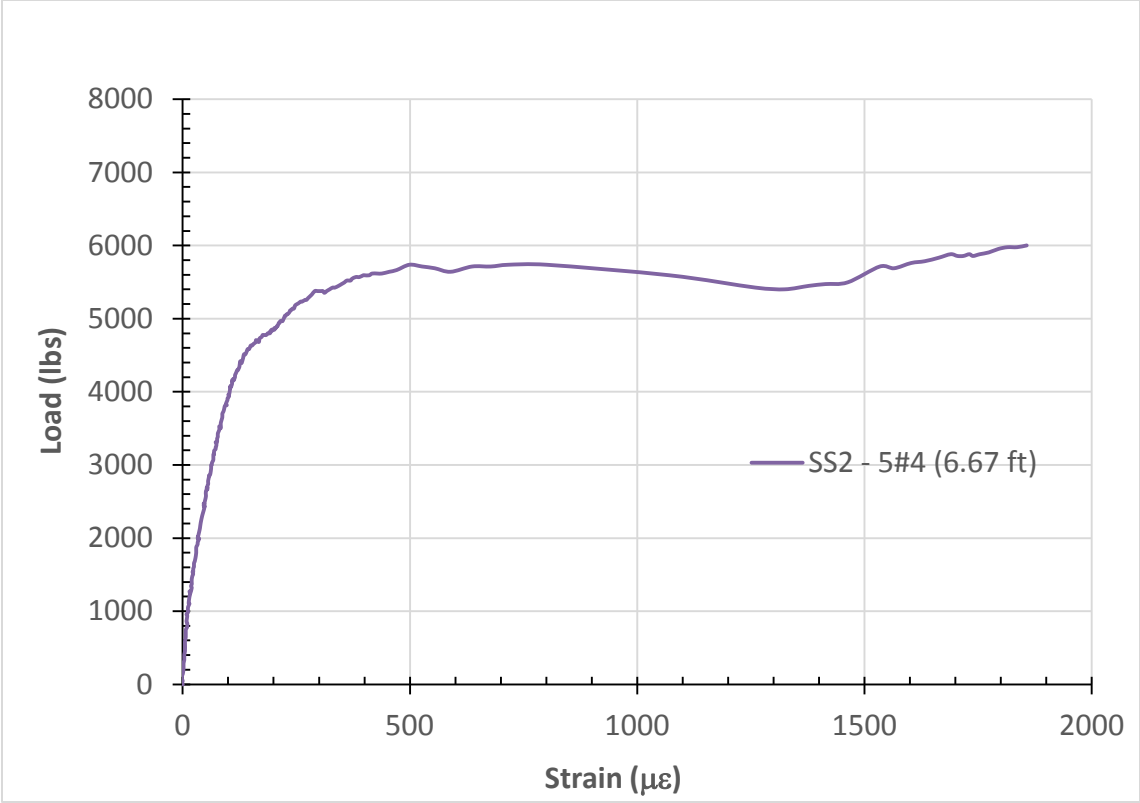

Figure 4.10. Load-Strain Curve for Concrete in Tension - Specimen SS2

The second set of four simply supported slabs are those taken from the failed two-span continuous specimens CS1 and CS2. Therefore, the slabs were all pre-cracked and no distinct pre-cracking stage is visible in any of their charts. Specimens SS3-CS1 and SS4-CS2 are 8 ft. long (L/H = 12.0), reinforced with 5#5 (1.55 in^2) and 5#4 (1.0 in^2), respectively. Both slabs had shear reinforcement on one side only hence they exhibited shear mode of failure, displayed in Figures 4.11 and 4.12, which explains the close ultimate moment capacities of 49.0 and 50.02 kip.ft for SS3-CS1 and SS4-CS2, respectively, and regardless of the difference in the reinforcement areas. The maximum deflection was 1.46 and 1.73 in. in the order mentioned, which reflects a stiffer behavior for the slab with higher reinforcement, as expected. The load-deflection curve, load-strain curve for bottom BFRP reinforcement, and the concrete in compression load-strain curve for both slabs are plotted in Figures 4.13 to 4.18.

Figure 4.11. Shear Failure of Specimen SS3-CS1

Figure 4.12. Shear Failure of Specimen SS4-CS2

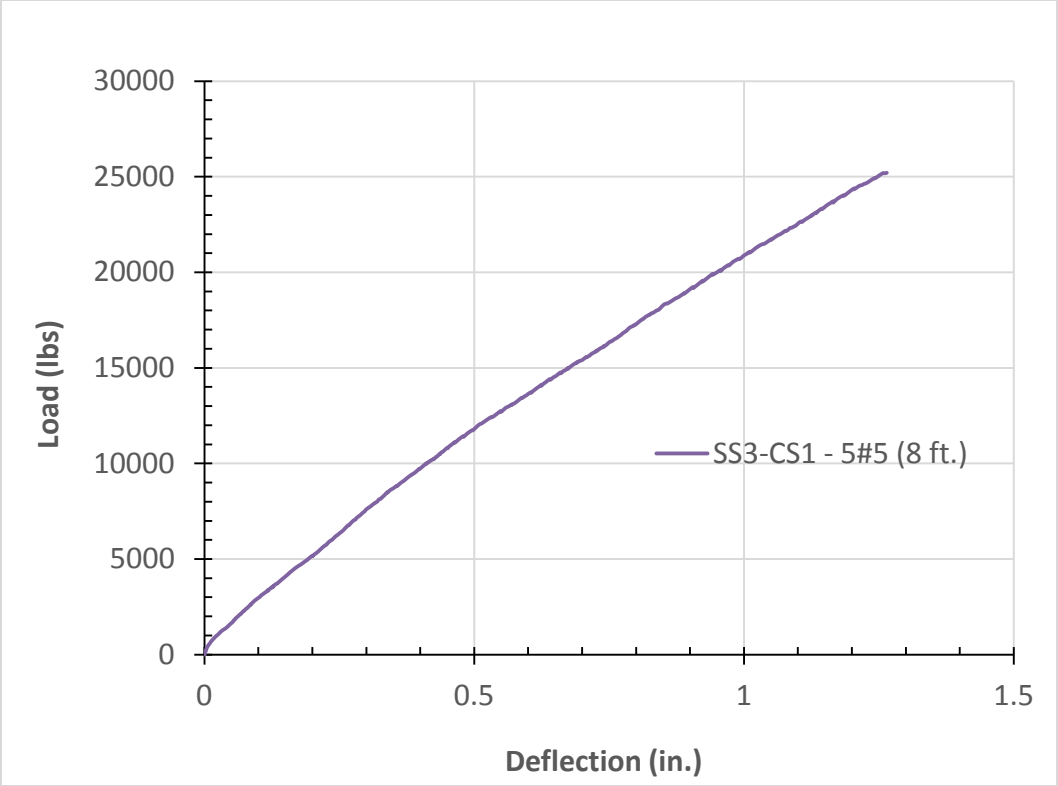

Figure 4.13. Load-Deflection Curve for Specimen SS3-CS1

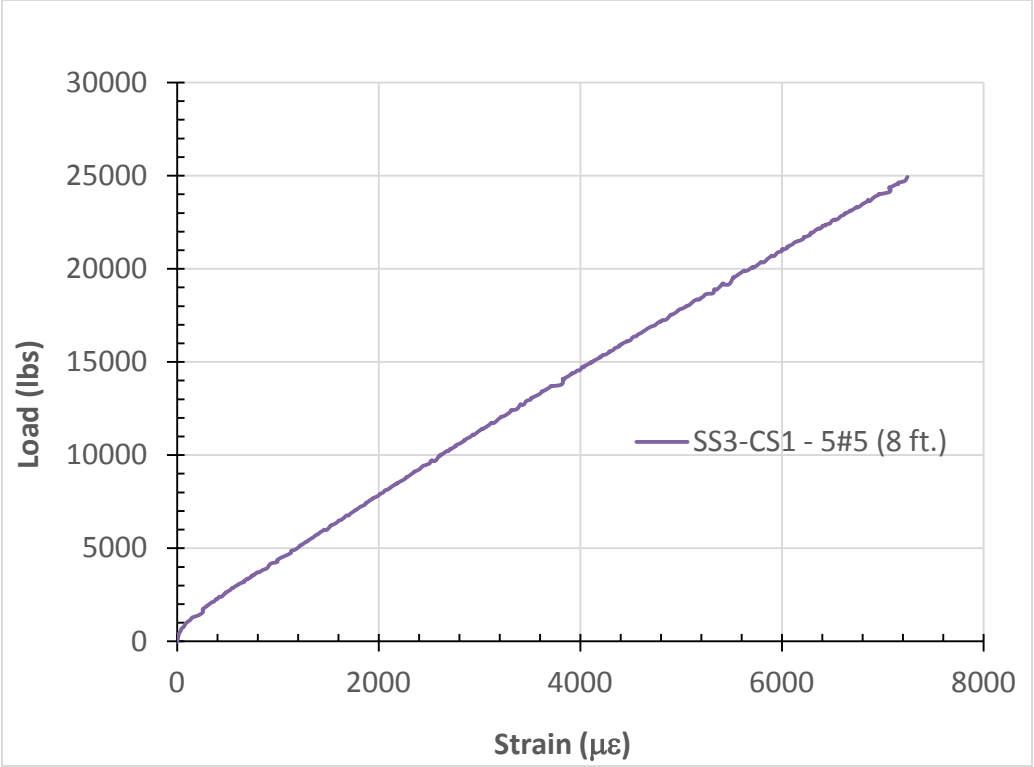

Figure 4.14. Load-Strain Curve for Bottom Reinforcement - Specimen SS3-CS1

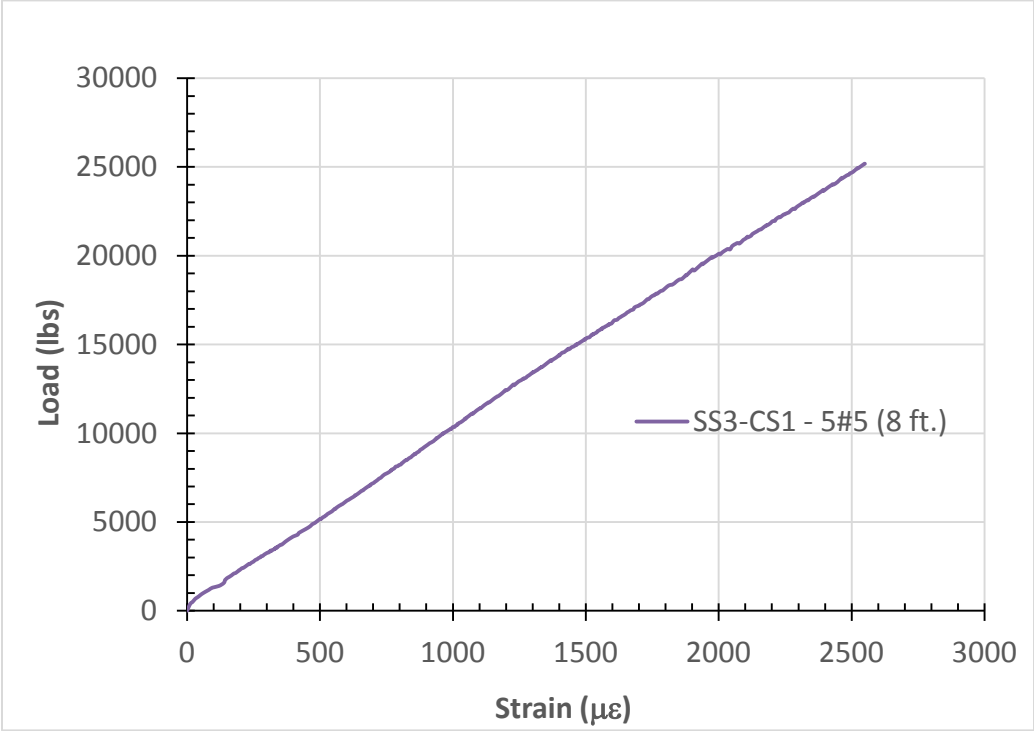

Figure 4.15. Load-Strain Curve for Concrete in Compression - Specimen SS3-CS1

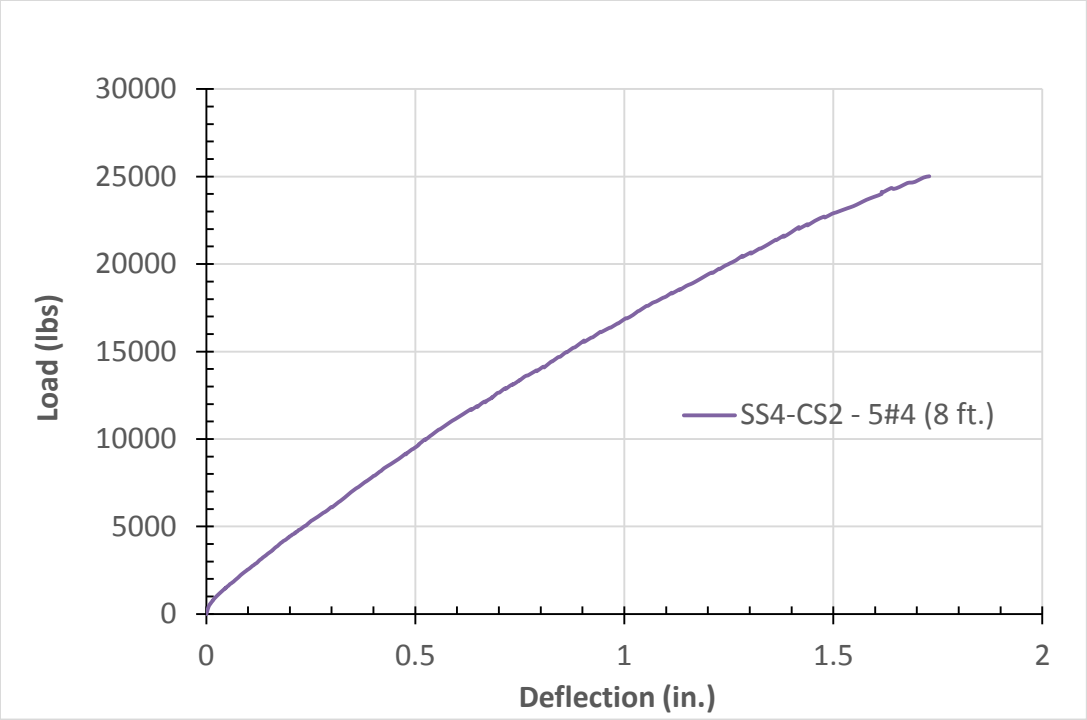

Figure 4. 16. Load-Deflection Curve for Specimen SS4-CS2

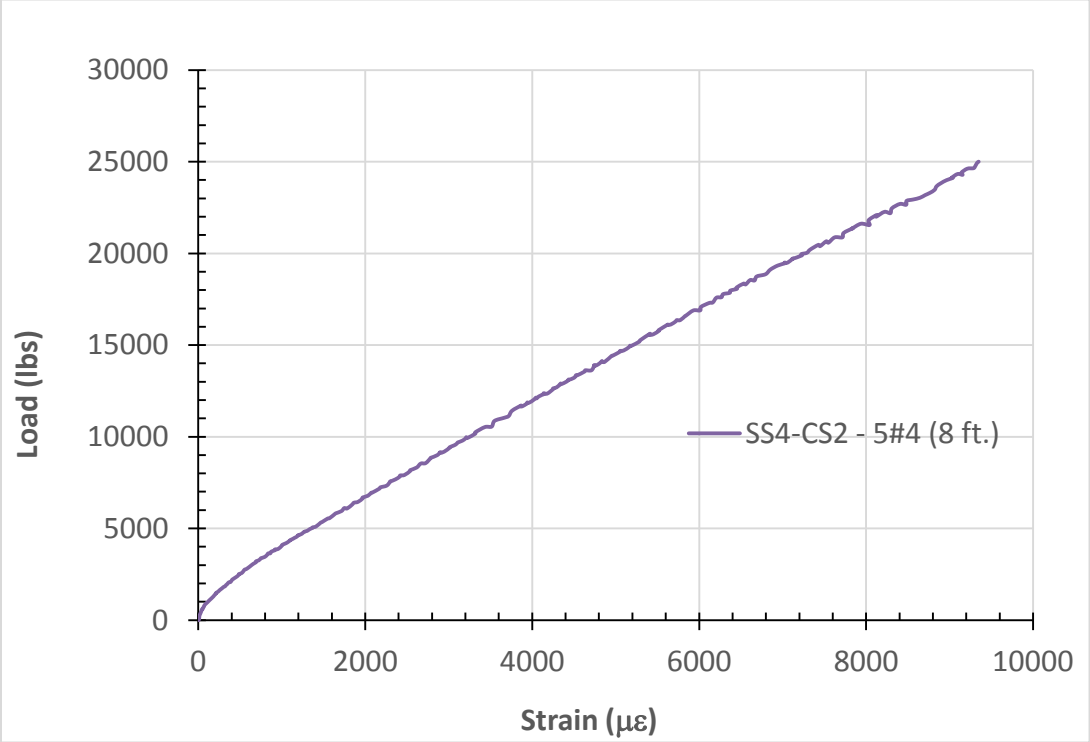

Figure 4.17. Load-Strain Curve for Bottom Reinforcement - Specimen SS4-CS2

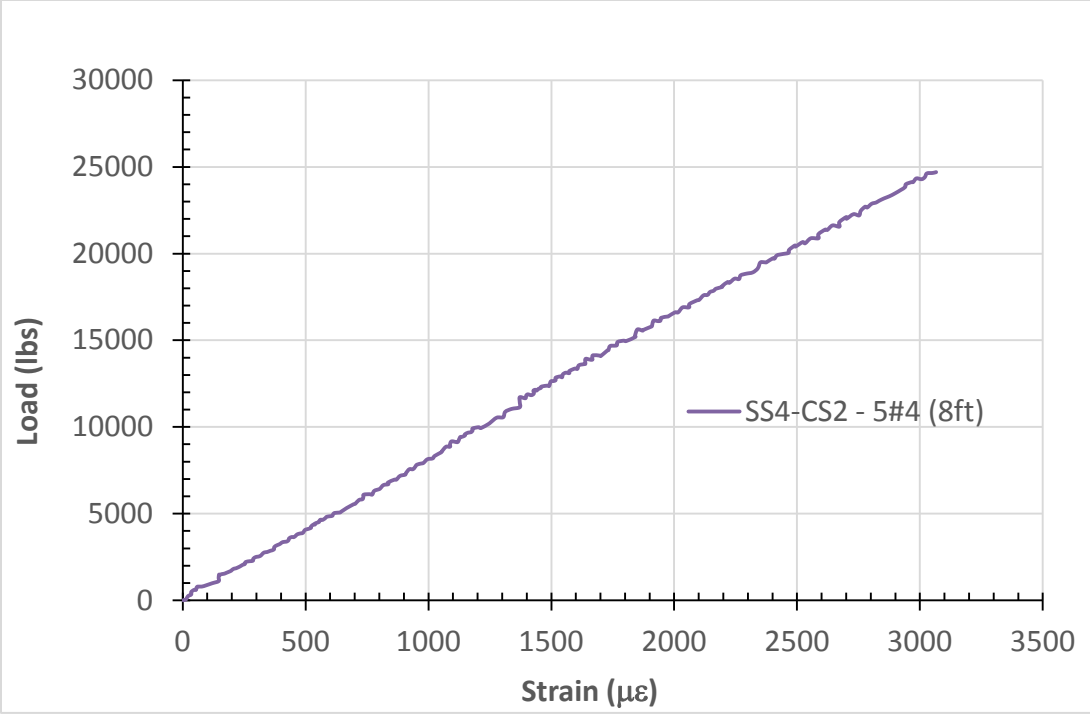

The last two simply supported slabs, SS5-CS1 and SS6-CS2, are reinforced with 1.55 in^2 and 1.0 in^2, respectively, having 6 ft. span length and L/H ratio equal to 9.0. Shear reinforcement was only present on one end of the slab. These slabs were cut out from the continuous slab due to their failure at the middle support as shown in Figures 4.19 and 4.20. Due to the similar mode of failure, both specimens had a close ultimate moment of 56.9 and 53.0 kip.ft, in the order mentioned earlier. Their maximum deflections were almost equal, with values of 0. 97 and 0.98 in.;~~,~~ however, these results were obtained at a load of 37.9 and 35.3 kips, respectively. Such behavior is expected due to the higher reinforcement area in former specimen. The load-deflection curve, load-strain curve for BFRP reinforcement in tension, and the concrete in compression load-strain curve for both slabs are plotted in Figures 4.21 to 4.26.

Figure 4.18. Shear Failure of Specimen SS5-CS1

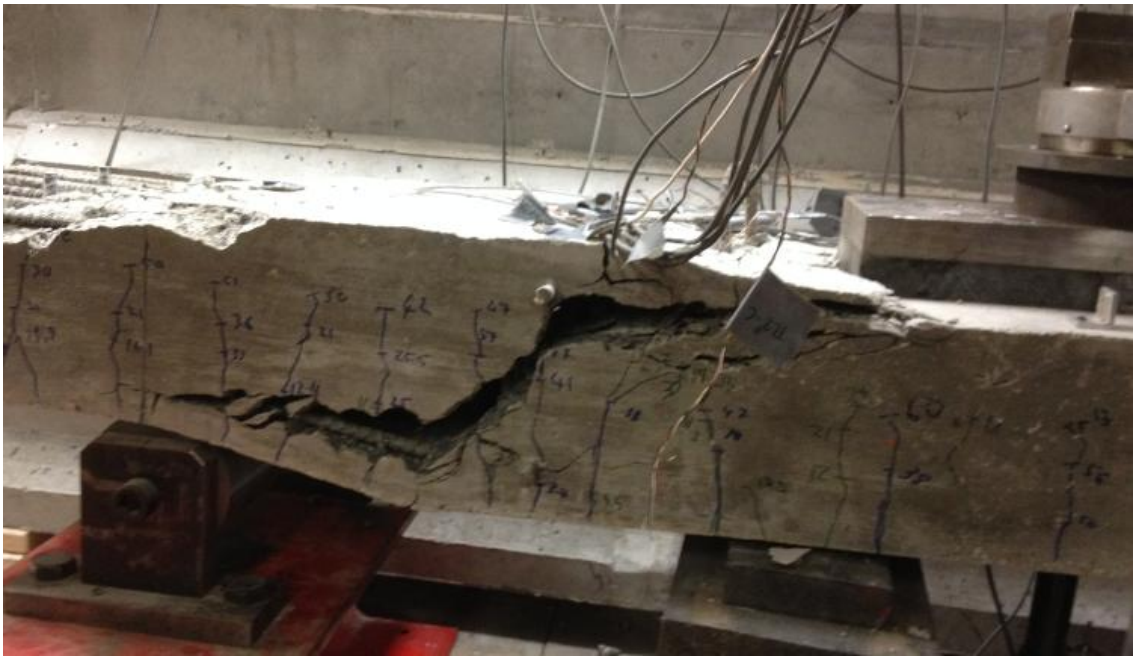

Figure 4.19. Shear Failure of Specimen SS6-CS2

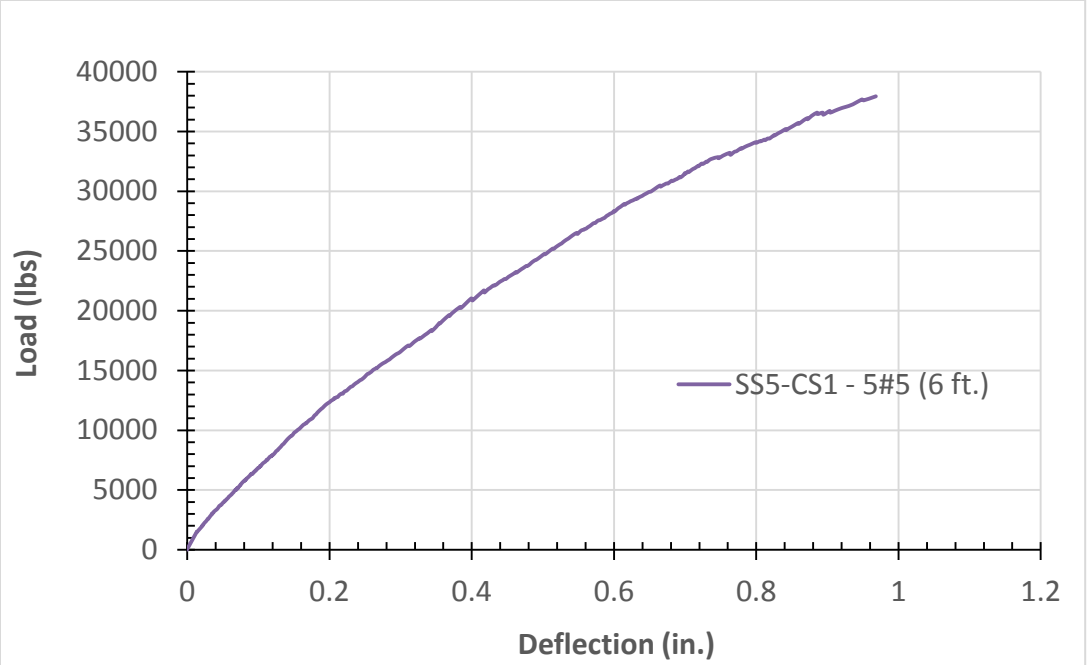

Figure 4.20. Load-Deflection Curve for Specimen SS5-CS1

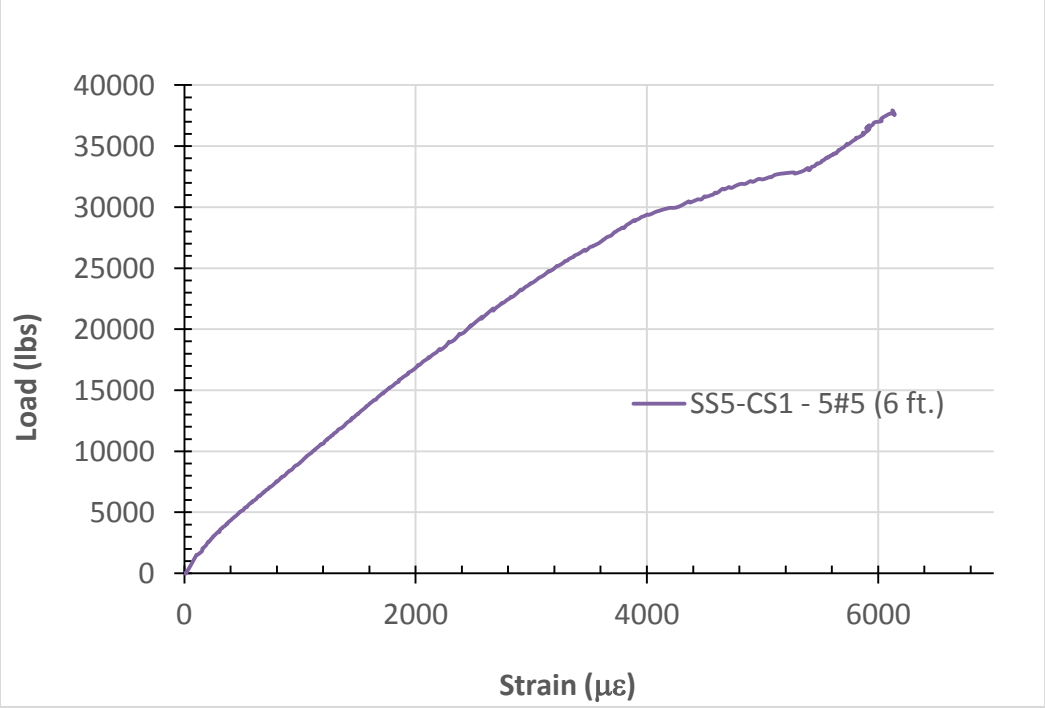

Figure 4.21. Load-Strain Curve for Bottom Reinforcement - Specimen SS5-CS1

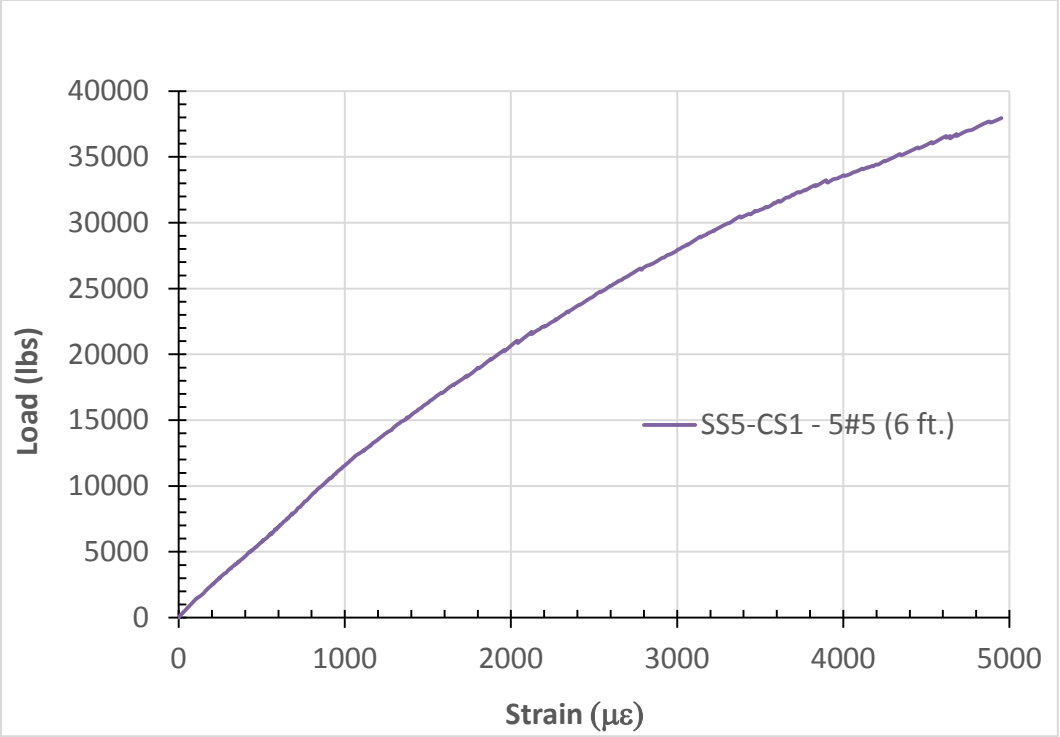

Figure 4.22. Load-Strain Curve for Concrete in Compression - Specimen SS5-CS1

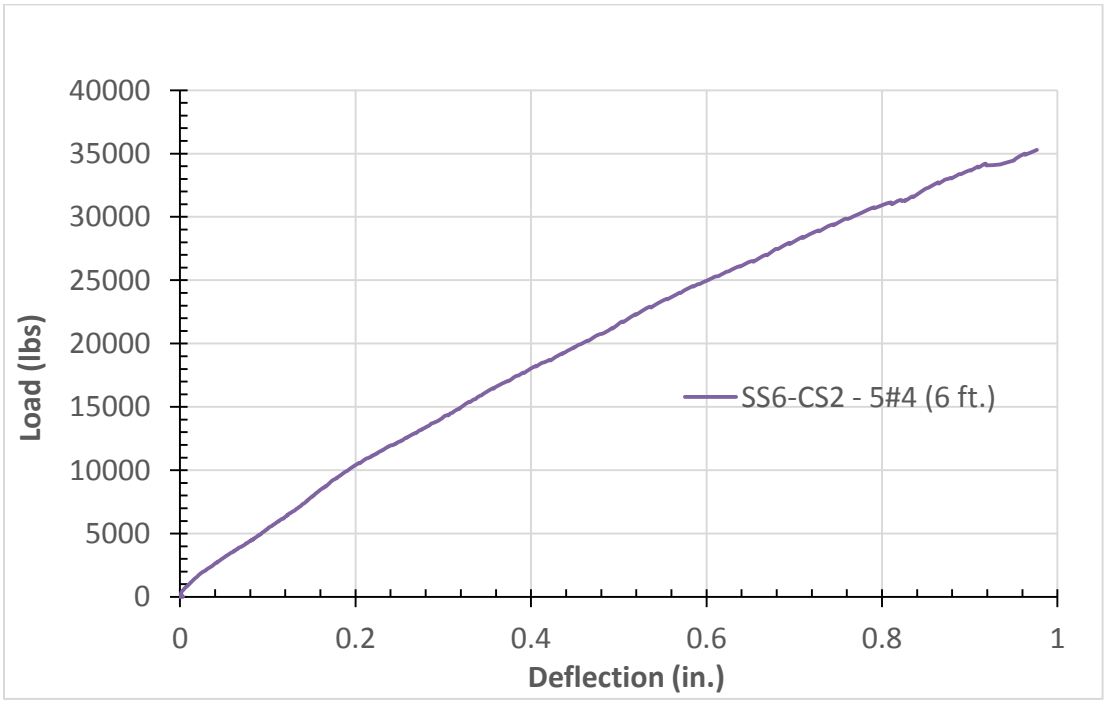

Figure 4.23. Load-Deflection Curve for Specimen SS6-CS2

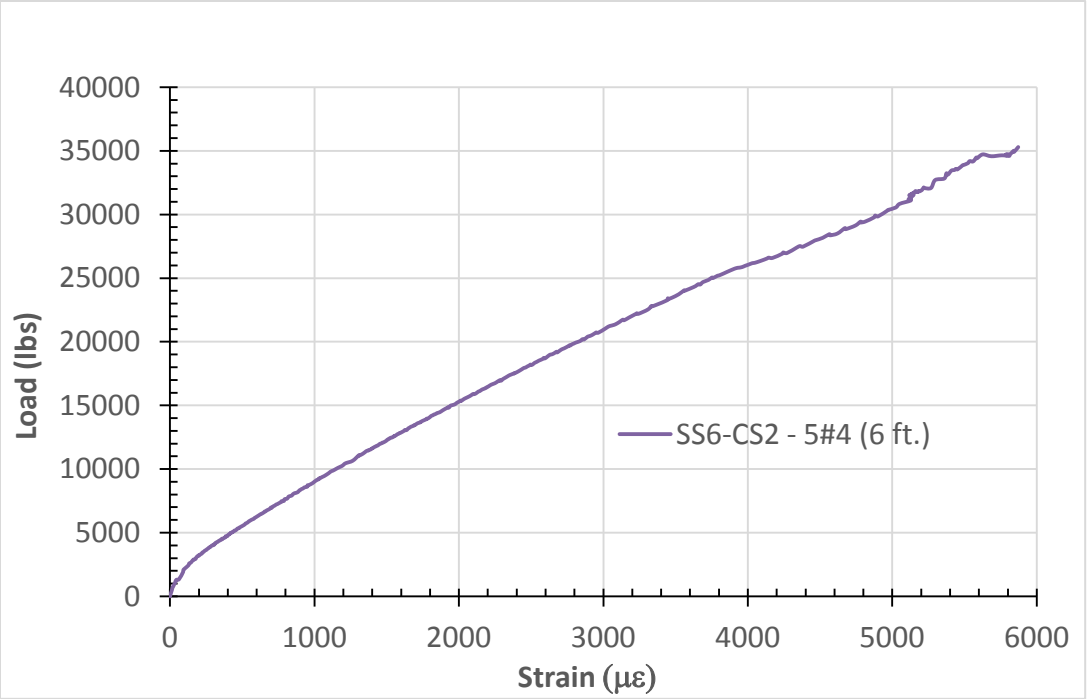

Figure 4.24. Load-Strain Curve for Bottom Reinforcement - Specimen SS6-CS2

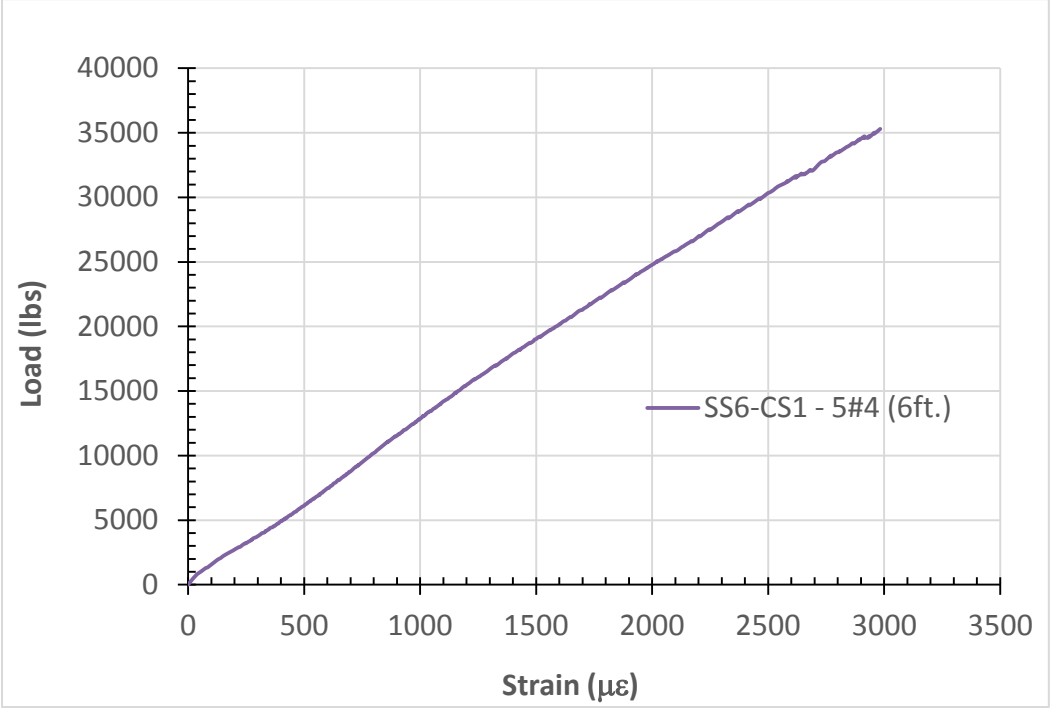

Figure 4.25. Load-Strain Curve for Concrete in Compression - Specimen SS6-CS2

4.2 Two-Span Continuous BFRP Reinforced Slabs

Both two-span continuous slabs were tested using a 2-point load 6 ft. apart, simulating a truck load. Each slab consisted of two 8.67 ft. spans (L/H = 13.0), with a total length of 17.33 ft. At the location of the middle support where the maximum moment (negative) would occur, CS1 and CS2 were reinforced with 6#5 (1.86 in^2) and 6#4 (1.2 in^2), respectively. By using (ρ_f/ρ_{fb}) greater than one, it was guaranteed that the failure would not occur in the BFRP reinforcing bars. For both specimens, shear reinforcement at the mid-support was provided in each span direction and at 4 in. spacing for a distance of twice the slab height (2H = 16 in.) followed by a spacing of 6 in. for a distance of 2 ft. The purpose of installing the stirrups was to prevent a shear failure at very low loads. The maximum experimental load reached by CS1 and CS2 was 51.86 and 68.57 kips, corresponding to ultimate moments of 41.9 and 55.4 kip.ft, respectively. Despite having a larger reinforcing area, slab CS1 failed inexplicably, and prematurely at a lower load than CS2. On the other hand and as anticipated, its load-deflection behavior during the testing exhibited a stiffer performance and the strain in the BFRP bars was lower compared to slab CS2. At ultimate loads, a maximum deflection of 0.55 and 1.32 in. was obtained for slabs CS1 and CS2, though these values are incomparable as CS1 failed to achieve its highest capacity. A better comparison which reflects the real behavior is achieved by relating the deflections of both specimens at the same load, such as the maximum reached by CS1 (51.86 kips). At this specific value, deflections were equal to 0.55 and 0.78 in. for slabs CS1 and CS2, respectively. It should be noted that the aforementioned deflection values are the average of the left and right spans of each slab. At the start of the testing, the first flexural crack initiated from the top fibers of the concrete at the middle support, followed by more cracks of the same type at the right and left of that location. As the load increased, crack initiation moved to the middle of each span and at the location of

load. With further increase in the load, flexural cracks along the spans continued to propagate while new cracks appeared near the middle support, ultimately causing a flexural shear mode of failure. Failure of both specimens is shown in Figures 4.27 and 4.28. The load-deflection curve, load-strain curve for BFRP bars in tension (top of mid-support), concrete in compression load-strain curve and concrete in tension load-strain curve for both slabs are shown in Figures 4.29 to 4.36.

Figure 4.26. Flexural Shear Failure of Specimen CS1

Figure 4.27. Flexural Shear Failure of Specimen CS2

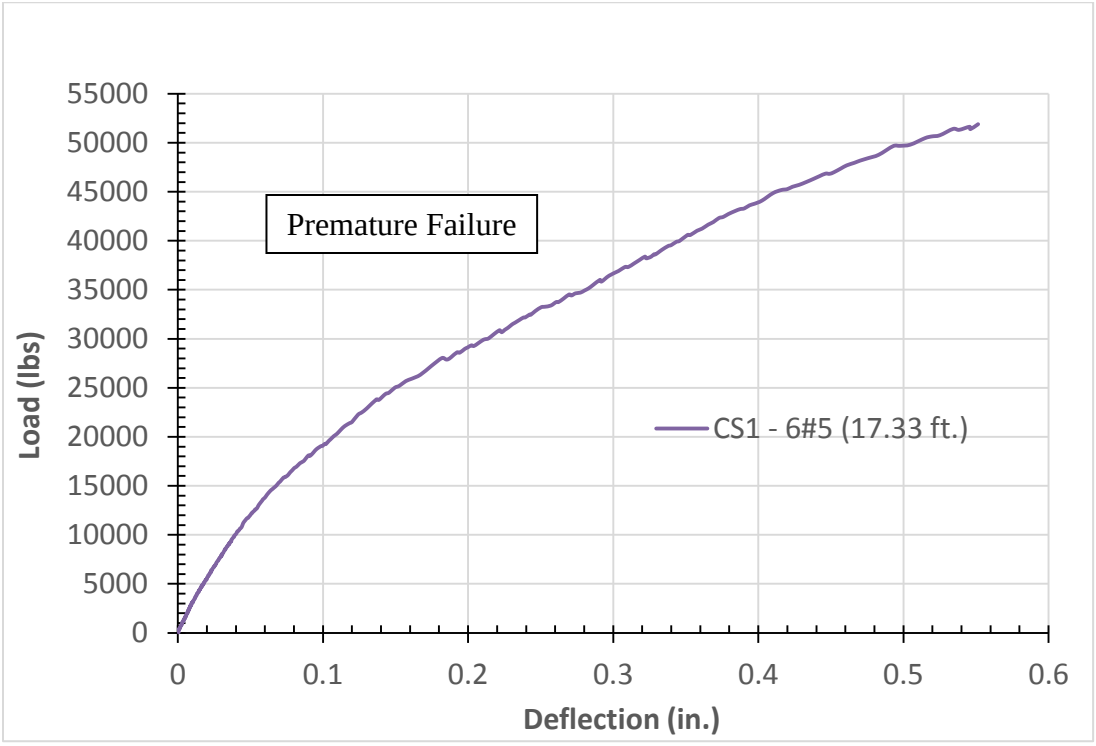

Figure 4.28. Load-Deflection Curve for Specimen CS1

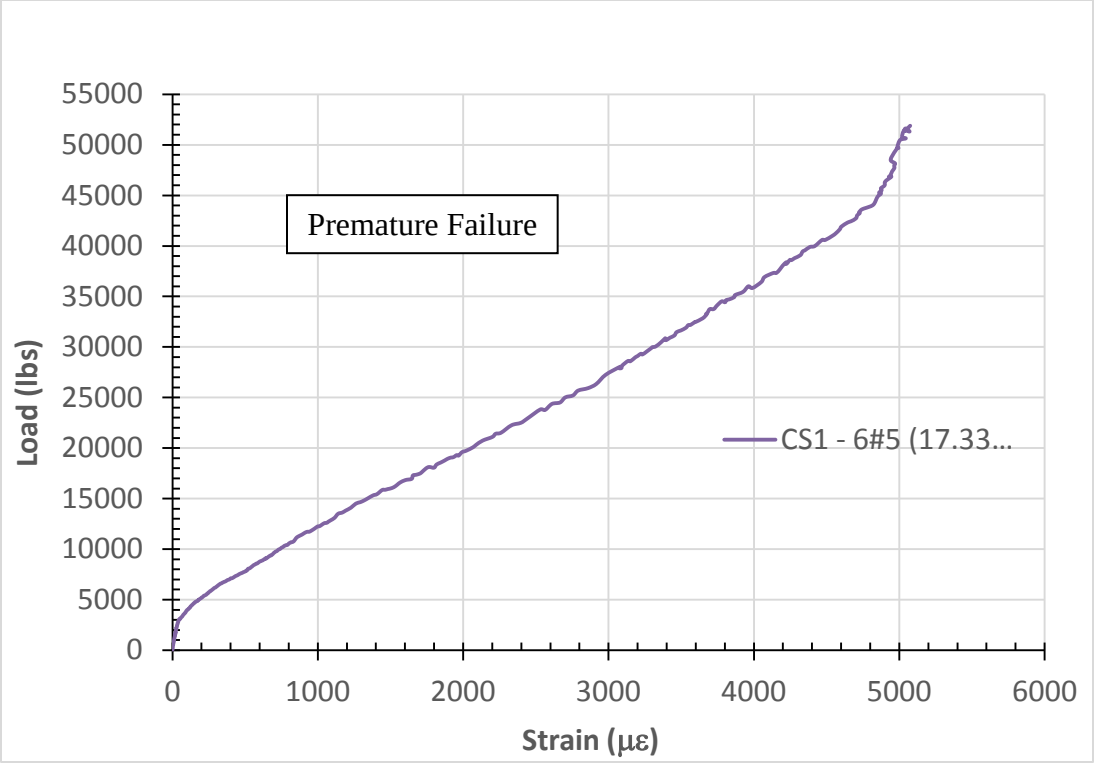

Figure 4.29.Load-Strain Curve for Top Reinforcement at Mid-Support- Specimen CS1

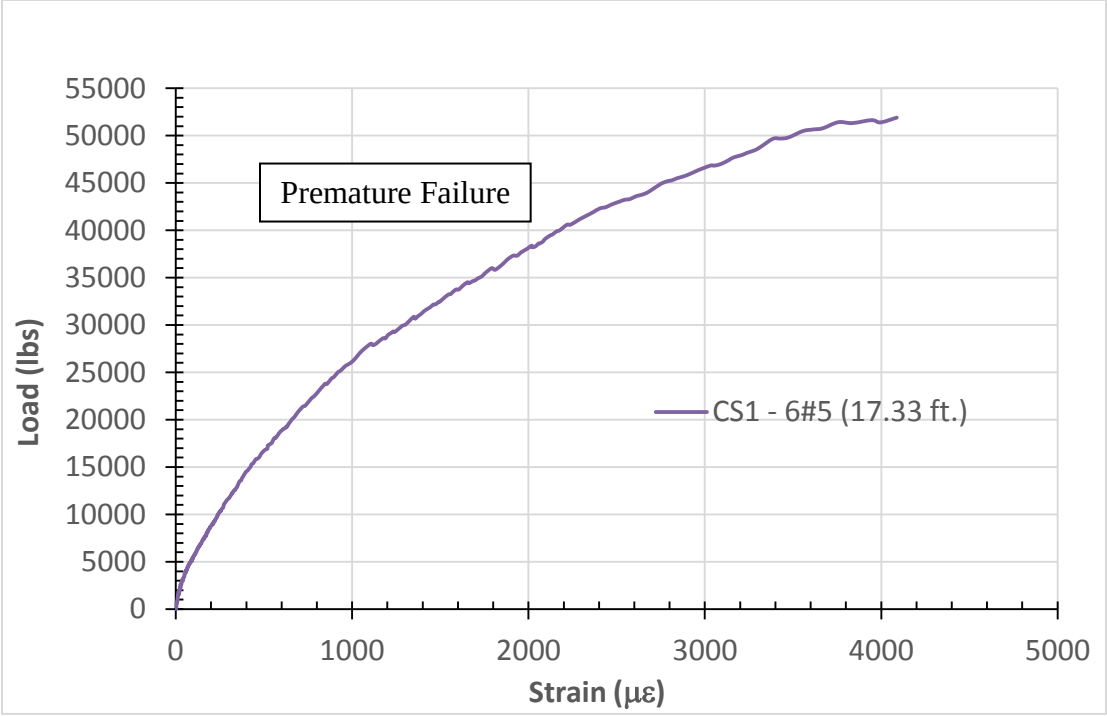

Figure 4.30. Load-Strain Curve for Concrete in Compression at Mid-Support- Specimen CS1

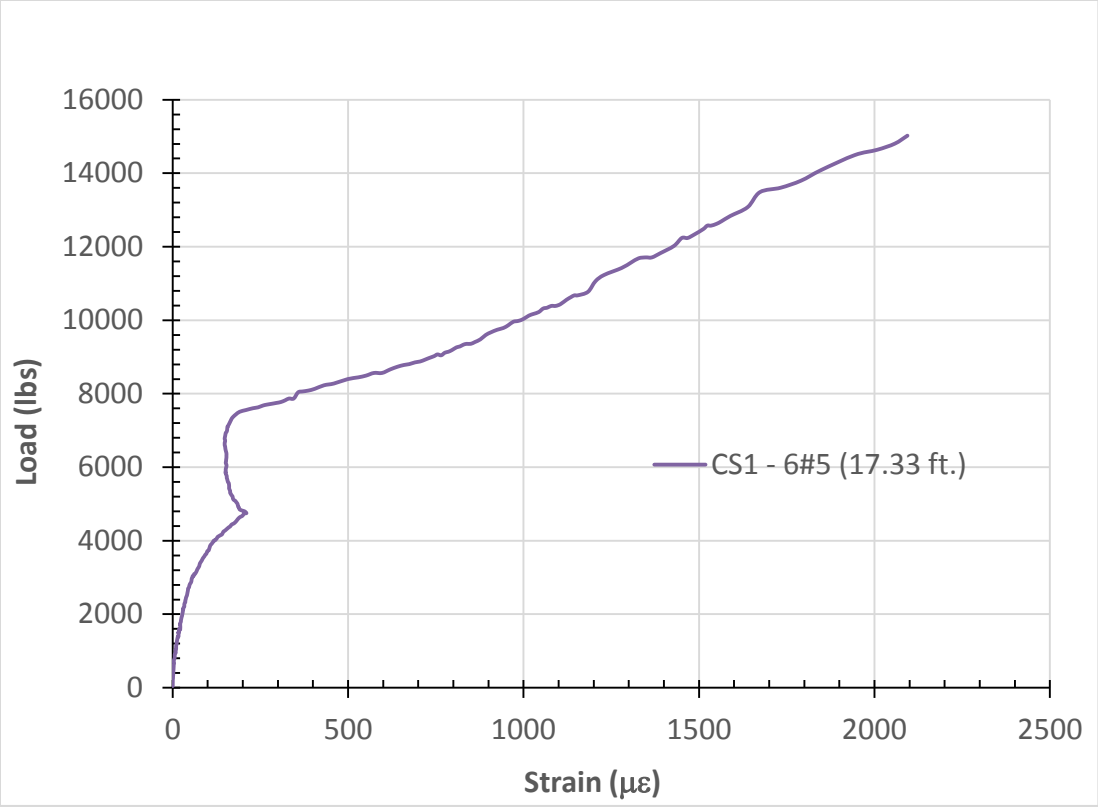

Figure 4.31. Load-Strain Curve for Concrete in Tension at Mid-Support- Specimen CS1

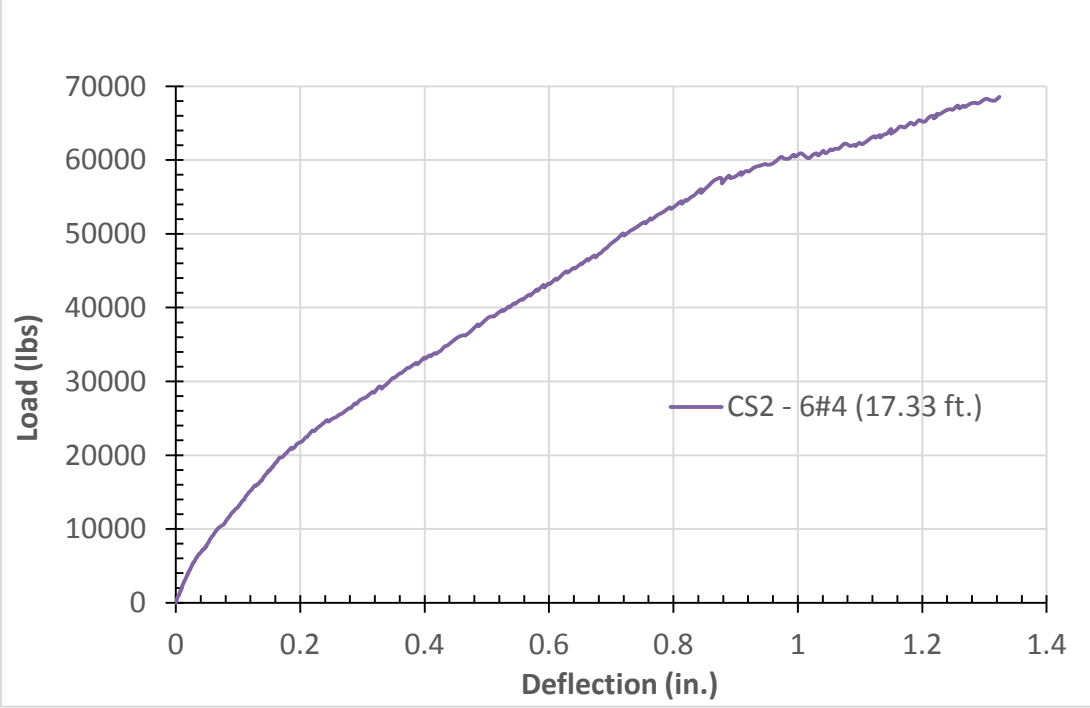

Figure 4.32. Load-Deflection Curve for Specimen CS2

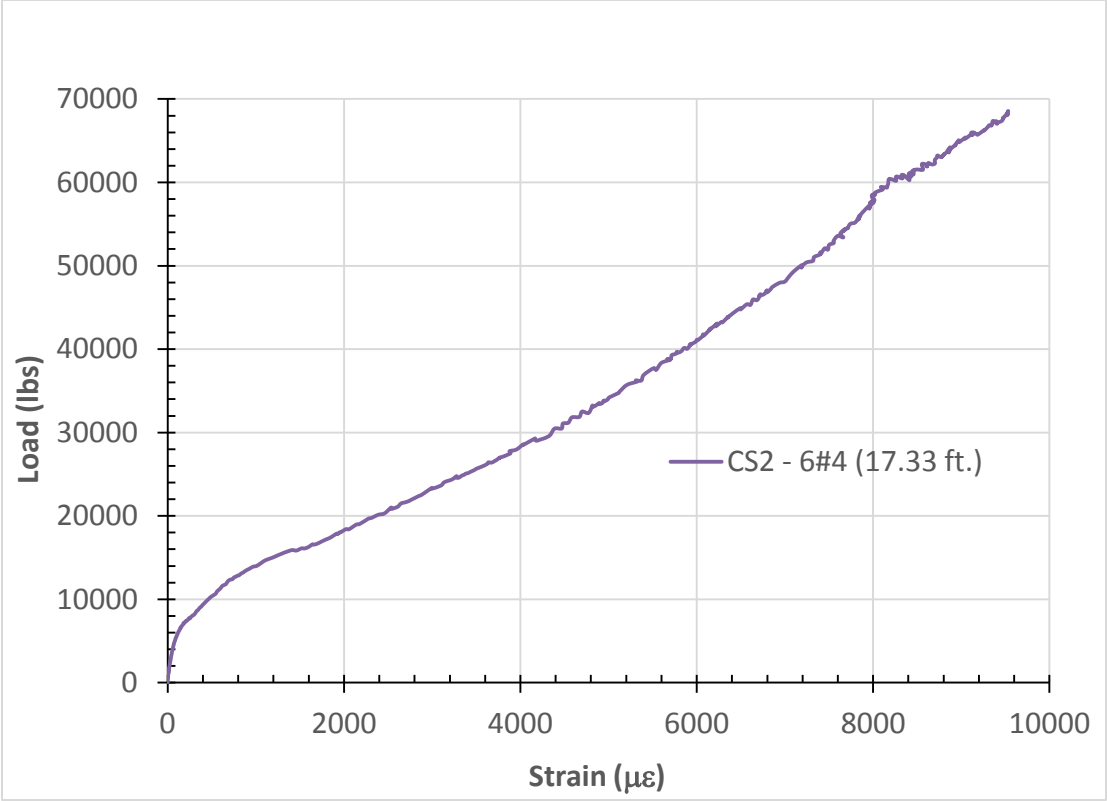

Figure 4.33. Load-Strain Curve for Top Reinforcement at Mid-Support- Specimen CS2

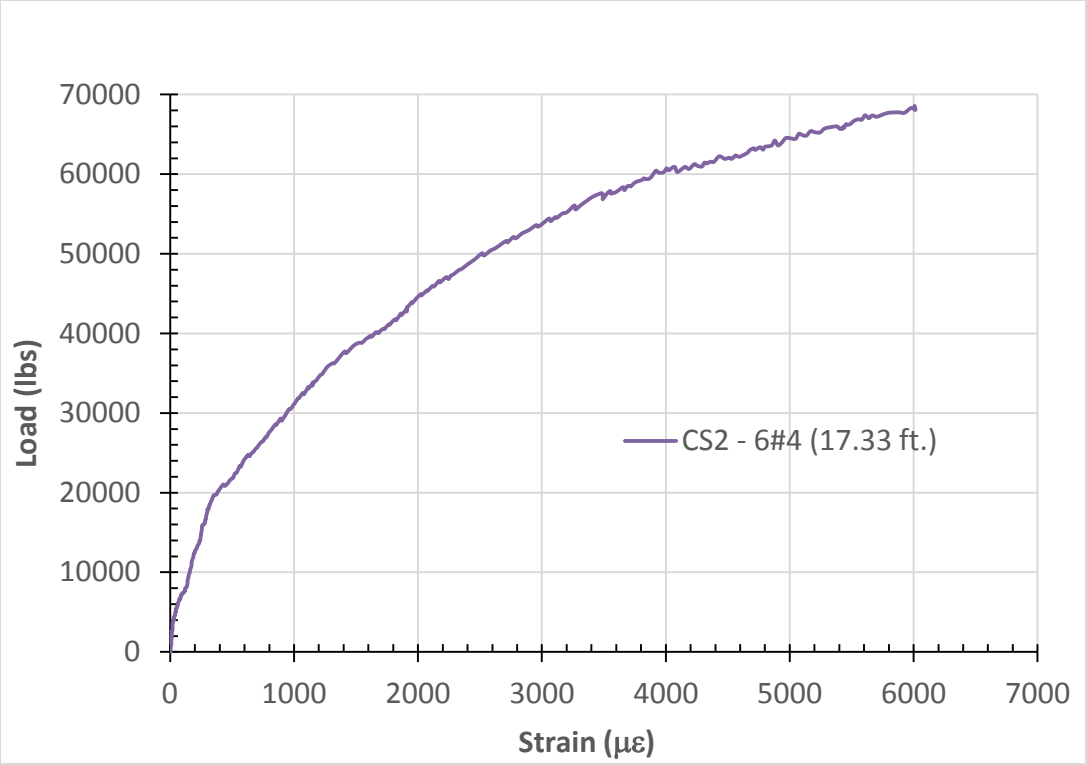

Figure 4 34. Load-Strain Curve for Concrete in Compression at Mid-Support- Specimen CS2

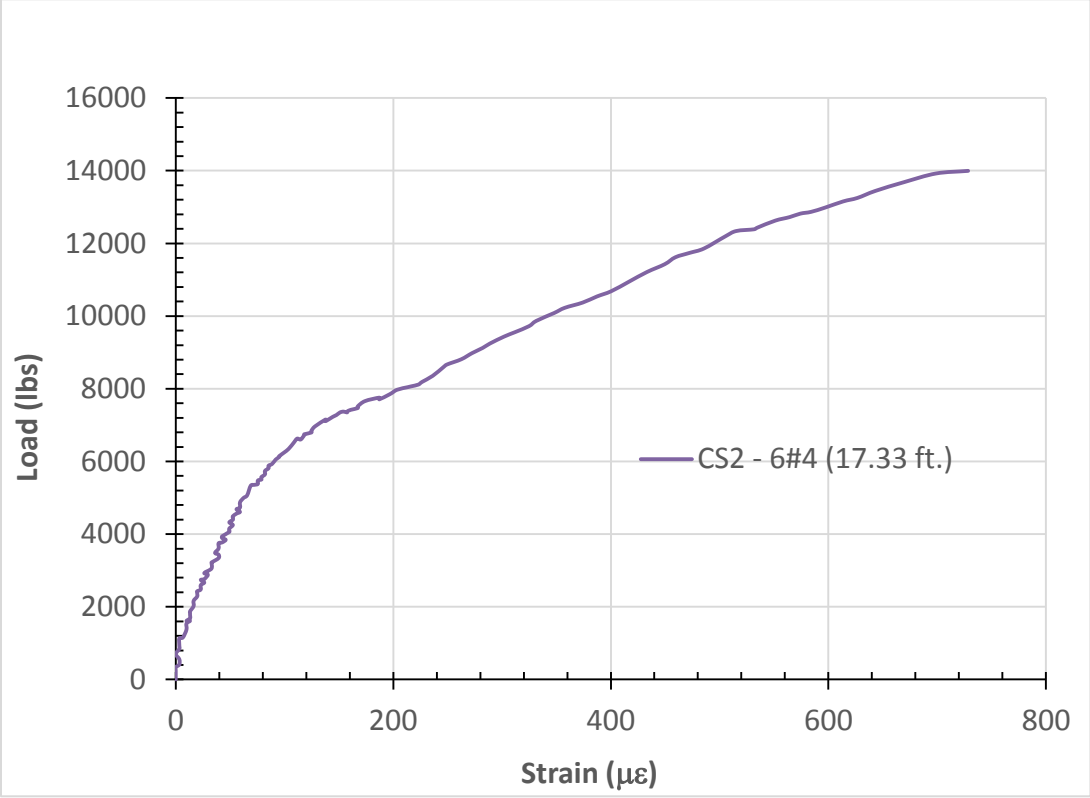

Figure 4.35. Load-Strain Curve for Concrete in Tension at Mid-Support- Specimen CS2

Pictures during the tests were taken to illustrate the cracks, deflection and behavior, and are shown below in Figures 4.37 to 4.39. After the simply supported slabs reached the maximum load and failed, a picture of deflected shape was taken, followed by progressive pictures during the release of the load, as displayed in Figure 4.40. The behavior was fully elastic due to the BFRP bars, and it returned to its unloaded position with a residual deflection of 0.55 in.

Figure 4.36. Deflected Shape and Cracks for Slab SS2

Figure 4.37. Left Span Cracking and Deflection of Slab CS1

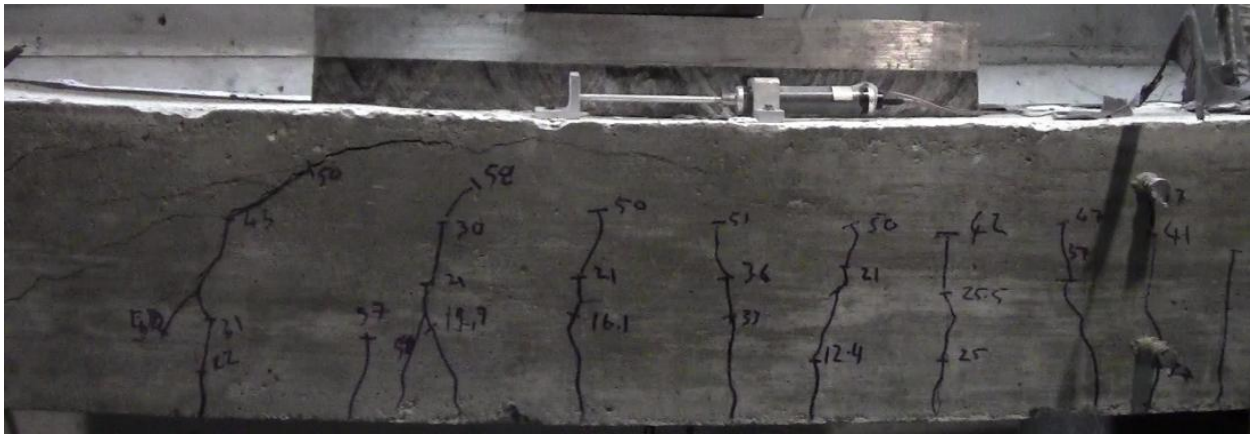

Figure 4. 38. Deflection and Flexural Shear Cracks for Continuous Slab CS2

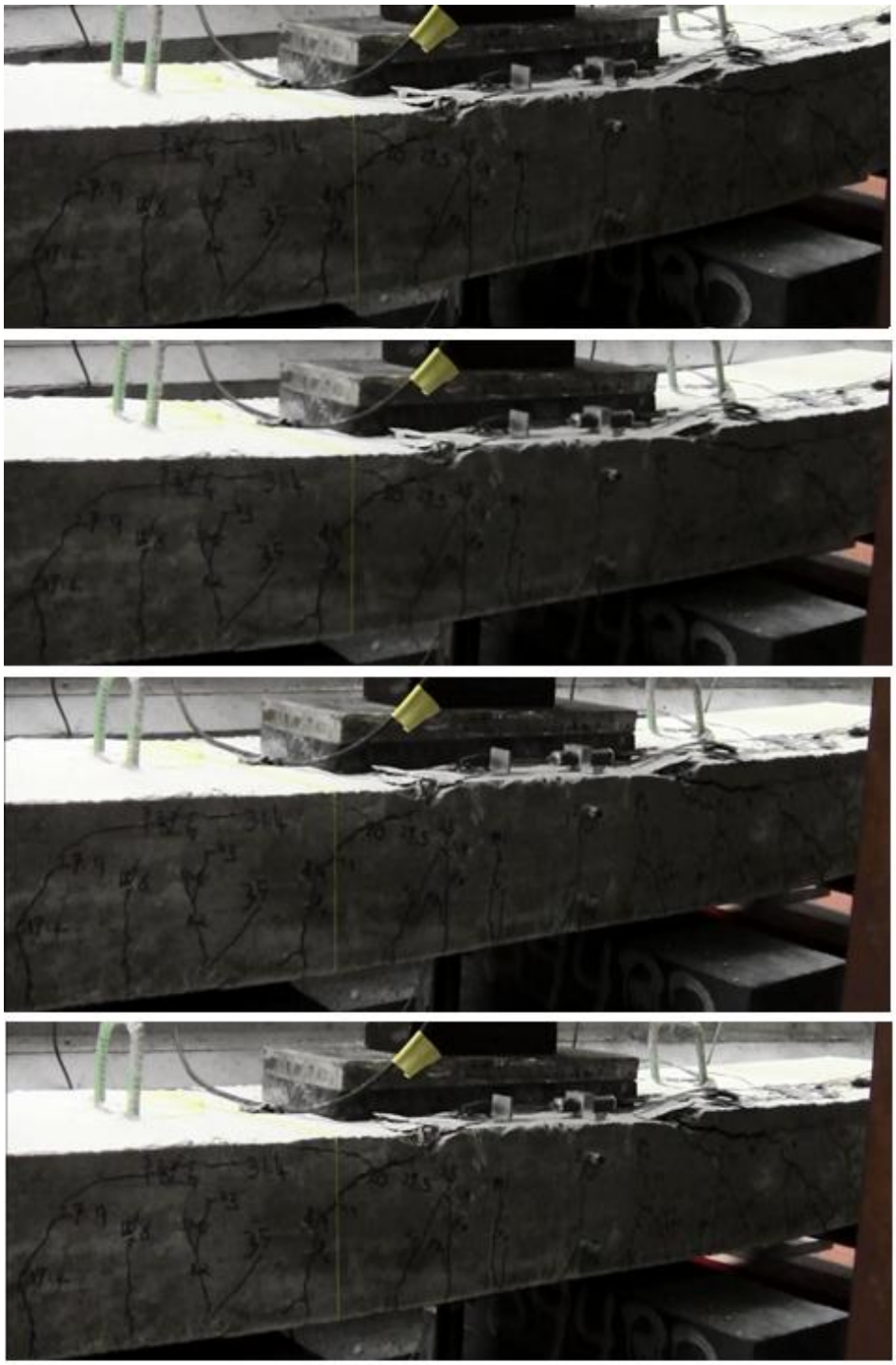

Figure 4.39. Elastic Behavior of Slab SS2 as the Load was Released (Top to Bottom: Ultimate Load to Release)

CHAPTER 5
DISCUSSION AND ANALYSIS

This chapter includes discussion and comparison of the experimental results for each set of specimens. It also contains analysis of the predicted capacities and deflections from the design code and literature, compared with the actual test results.

5.1. Simply Supported Slabs

5.1.1. Slabs SS1 and SS2

Specimens SS1 and SS2 have a span length of 6.67 ft., and an L/H ratio of 10. The load-deflection curves in Figure 5.1 show three distinct stages; pre-cracking, cracking and post-cracking. The cracking load was 5.85 and 5.74 kips for SS1 and SS2, respectively. As expected, both slabs exhibited similar behavior at the pre-cracking stage. The load increased linearly until the cracking load was reached. Subsequently, a slight decrease in the load and an increase in the deflection occurred due to the first crack. The linear post-cracking stage shown in Figure 5.1 is a property of the BFRP reinforcing bars, unlike steel which has a plastic region after yielding. The stiffness, represented by the slope of the curve, decreased after the first flexural crack occurred, but it was higher for SS1 after cracking due to the higher reinforcement area. Before cracking, the difference in the reinforcement area didn't affect the specimens' stiffness. It can also be observed that at any load after the first crack, specimen SS2 displayed larger deflection. At 35 kips, the deflection of SS1 was 71% of that for SS2, because the reinforcement area in SS1 is 1.5 times that in SS2. The pre-cracking, cracking and post-cracking stages are also clear in the load-strain relationships for BFRP bars and concrete, as shown in Figures 5.2 and 5.3. As expected, the specimen with lower reinforcement, SS2, experienced larger strains in the BFRP

reinforcement in tension and concrete in compression, and were equal to 13693 με and 2924 με, compared to 9645 με and 2075 με for SS1, respectively. The maximum strain in BFRP reinforcement for SS1 was 70% of that for SS2. The maximum registered BFRP strain for SS1 and SS2 corresponds to 48% and 68% of the ultimate strain of BFRP rebar. The main criteria in FRP design is to control the serviceability requirements. It is evident that increasing the reinforcement area results in achieving less deflection values, especially at higher loads where the gap increases between the load-deflection of SS1 and SS2 curves.

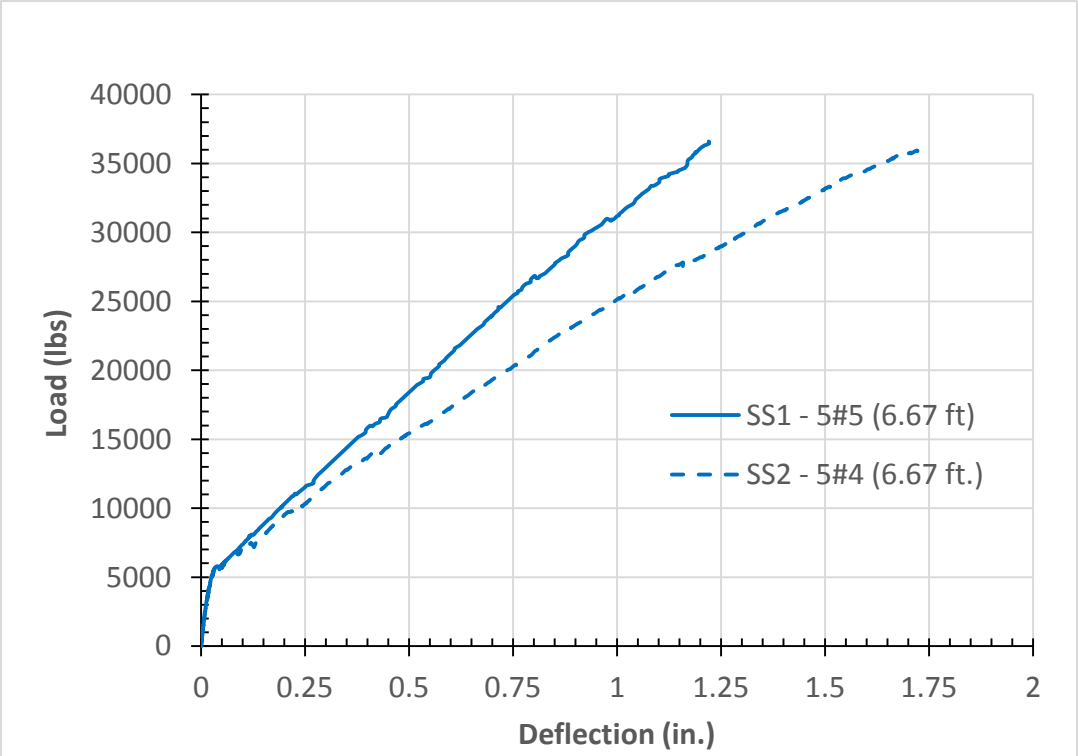

Figure 5.1. Load-Deflection Curve for SS1 and SS2

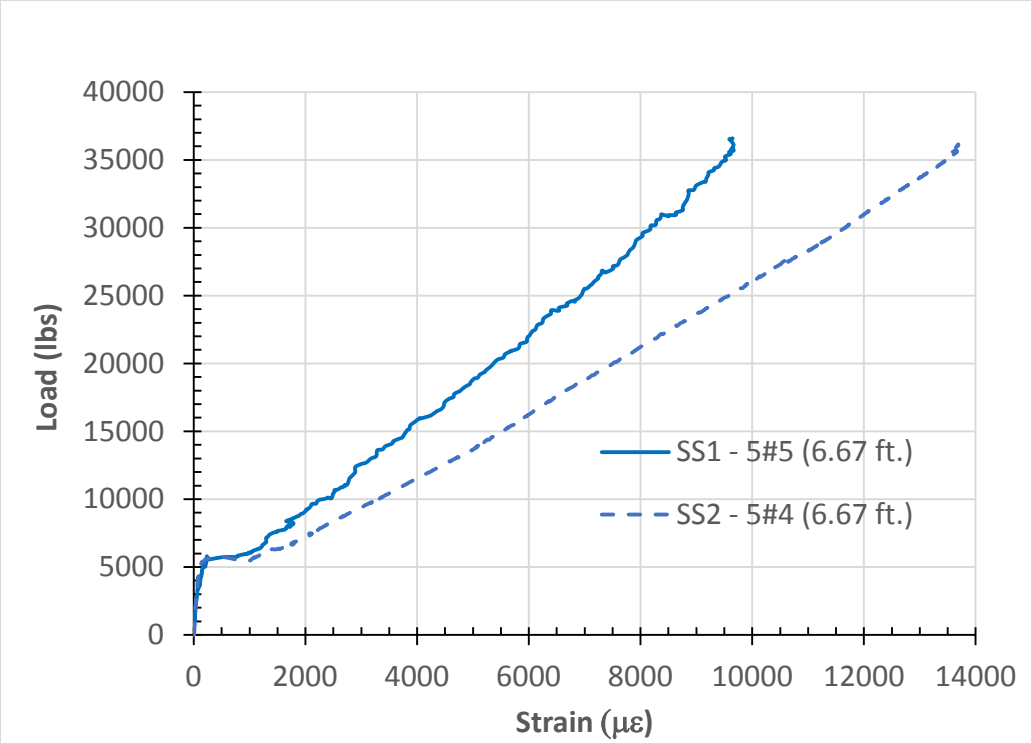

Figure 5.2. Load-Strain Curve for BFRP bars in Tension at Midspan for SS1 and SS2

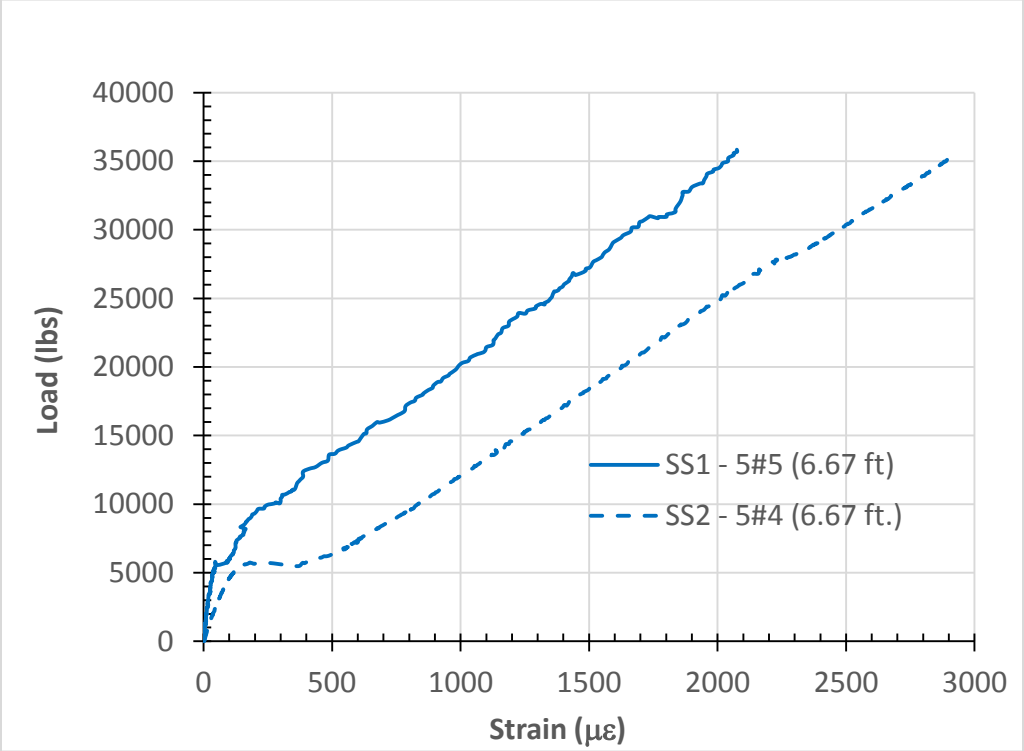

Figure 5. 3.Load-Strain Curve for Concrete in Compression (at Midspan) for SS1 and SS2

5.1.2. Slabs from Continuous Specimens

Four slabs were taken from the continuous specimens after being tested to investigate their moment capacities and maximum deflections. Slabs designated "-CS1" were reinforced with 5#5 at the bottom, while those designated "-CS2" had 5#4. SS3-CS1 and SS4-CS2 have an 8 ft. span with an L/H ratio of 12, less than the maximum L/H ratio allowed by ACI 440.1R (2006) for solid slabs. The other two slabs, SS5-CS1 and SS6-CS2, have a 6 ft. span and a lower L/H ratio of 9.0. All slabs were pre-cracked due to the tests performed earlier on the continuous slabs, which explains why there is no clear pre-cracking and post-cracking stages in the load-deflection curves shown in Figures 5.4 and 5.5. In each set, the slab with higher reinforcement exhibited stiffer behavior, less deflection, and had less strain in the reinforcement, as expected.

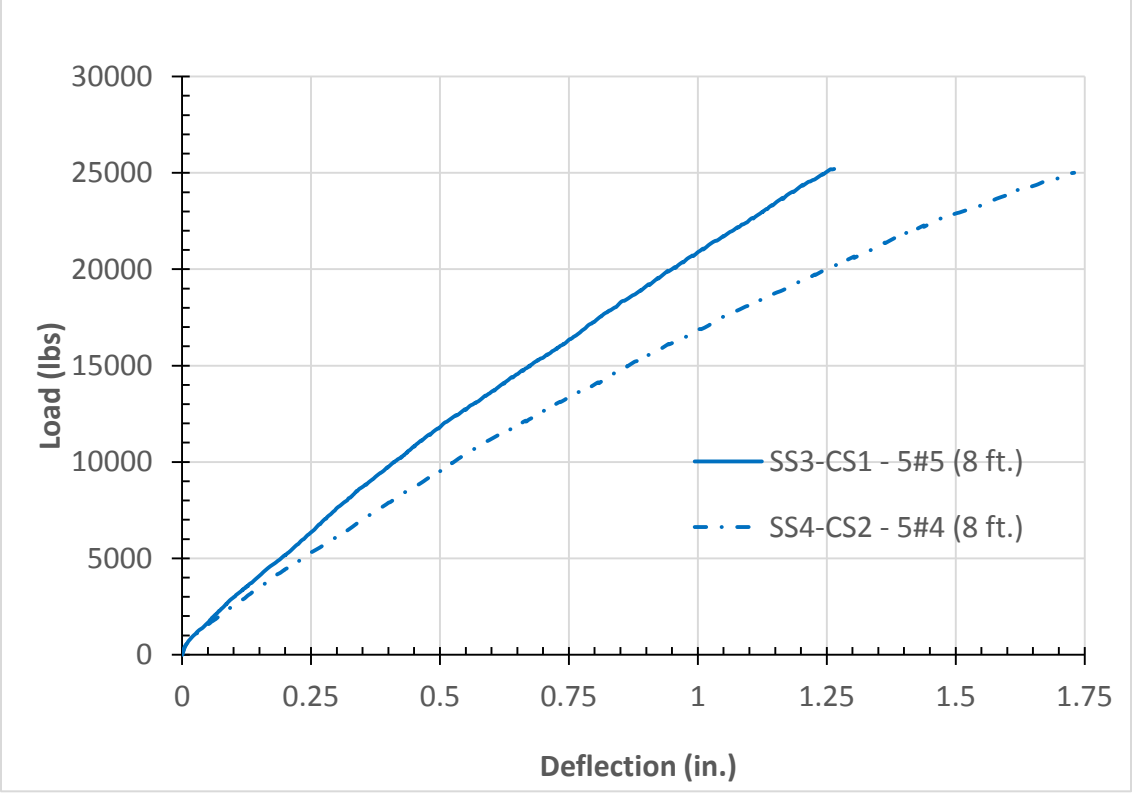

Figure 5.4. Load-Deflection Curve for SS3-CS1 and SS4-CS2

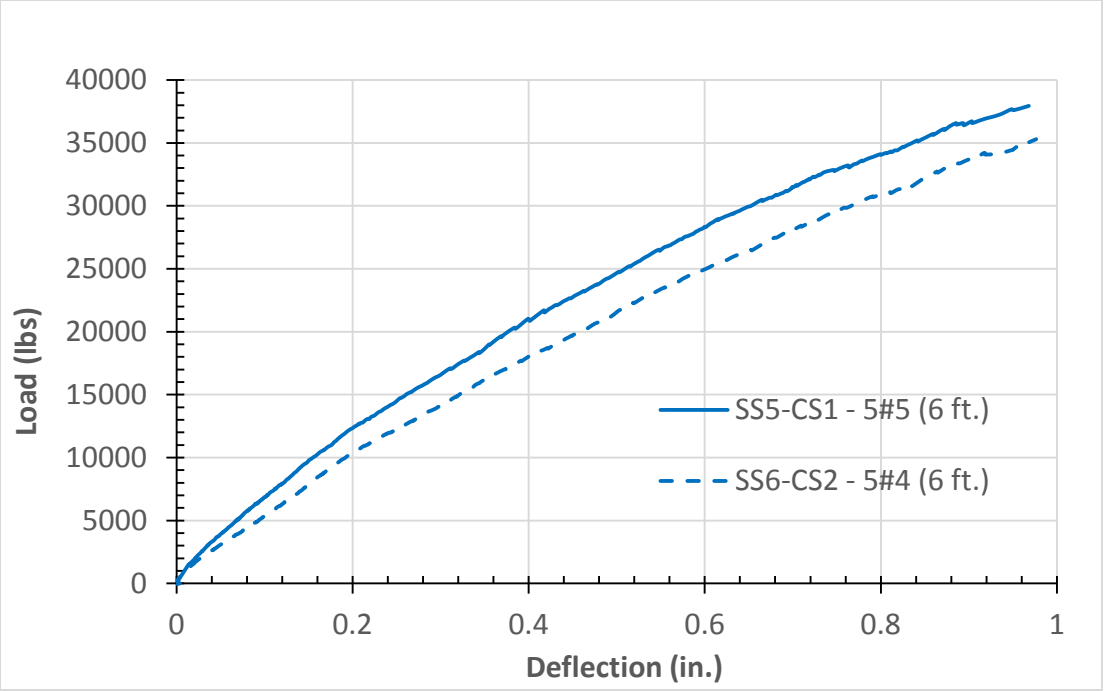

Figure 5.5. Load-Deflection Curve for SS5-CS1 and SS6-CS2

Figure 5.4 reveals that at 25 kips, SS3-CS1 deflected 1.25 in., which is 72% the deflection of SS4-CS2 that deflected 1.74 in. This ratio is very close to that obtained from SS1 and SS2 (71%) at a load of 35 kips and shown in Figure 5.1. Both specimens had the same BFRP tensile strain at the maximum load although at first they followed the trend of other specimens until a load value of 30 kips, as shown in Figure 5.6. The load-deflection curves shown in Figure 5.5 shows that both slabs SS5-CS1 and SS6-CS2 had the same deflection of 0.97 in. at failure, however the failure occurred at different loads. By comparing the deflection at the same load for each slab, say 35 kips, the deflection of SS5-CS1 was 86% that of SS6-CS2. Figure 5.7 indicates that BFRP reinforcement underwent less deformation in SS5-CS1 compared to SS6-CS2, with strains of 7242 and 9350 με respectively, a ratio of 77% between the first to the second. It should be noted that the strain readings for the bottom reinforcement were taken 7.25 in. away from the center of

the 8 ft. span, and 19 in. away from the center of the 6 ft. span because these specimens utilized the same instruments previously installed at the same location on the continuous slabs.

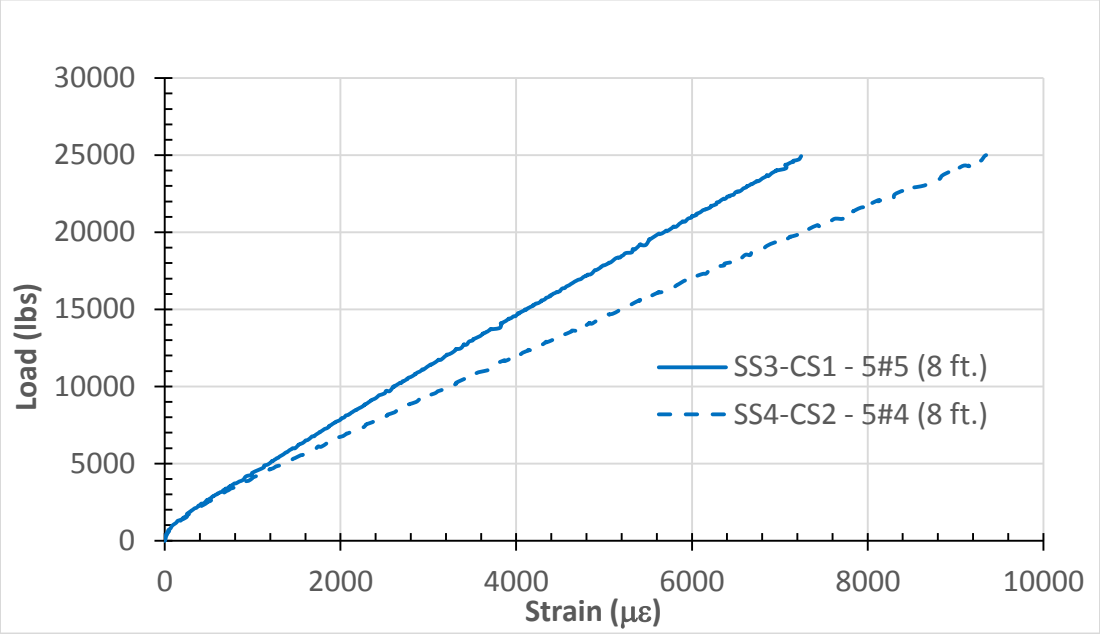

Figure 5.6. Load-Strain Curve for BFRP bars in Tension (7.25 in. from midspan) for SS3-CS1 and SS4—CS2

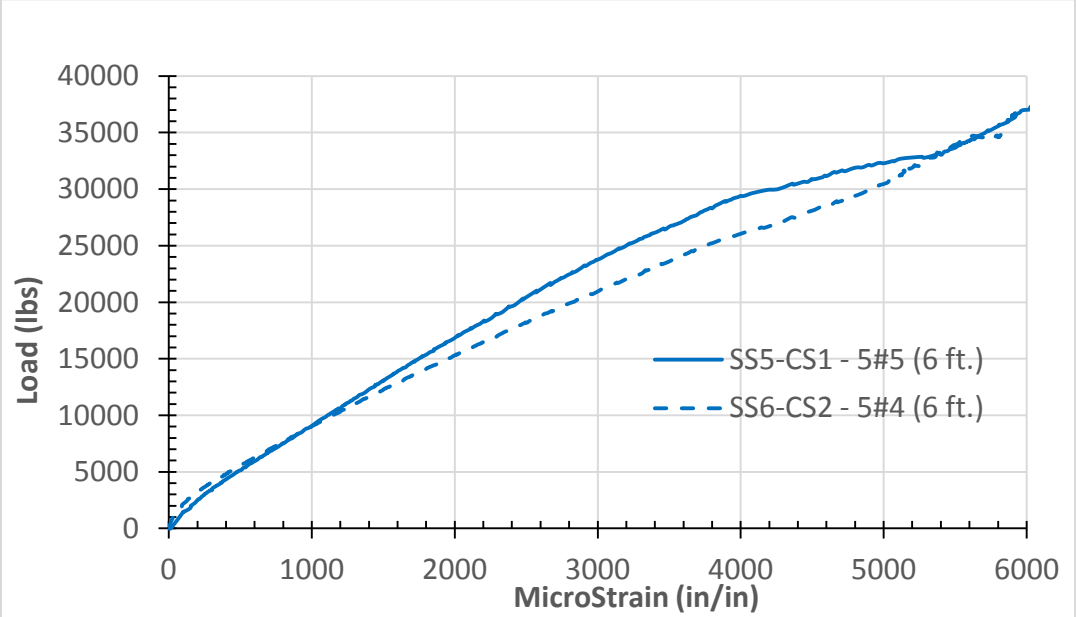

Figure 5.7. Load-Strain Curve for BFRP bars in Tension (19 in. from midspan) for SS5-CS1 and SS6—CS2

5.2. Two-Span Continuous Slabs

The continuous slabs CS1 and CS2 consisted of two spans each 8.67 ft. in length and a total length of 17.33 ft. The load was applied to generate the maximum negative moment at the support using a 6 ft. long spreader beam, with each load located 3 ft. from the mid-support. This setup simulates the axle of the HL-93 truck where the width of its axle center to center of the tires is 6 ft.

The transition from the pre-cracking to the post-cracking zones was very smooth and barely noticeable. However, it can be seen from the change in the slope of the load-deflection or load-strain curves. Slab CS1 failed prematurely at a load of 51.86 kips with a maximum deflection of 0.55 in. as shown in Figure 5.8. Its maximum BFRP tensile strain was 5076 με and the maximum concrete compressive strain was 4088 με as shown in Figures 5.9 and 5.10, respectively. The strain in the reinforcement was just one quarter of the ultimate strain. On the other hand, CS2 failed at its full capacity at a load of 68.6 kips after deflecting 1.32 in. The maximum strains for BFRP in tension and concrete in compression were 9532 με and 6005 με, respectively.

The deflection of CS1 at 50 kips load was 0.52 in., and is equal to 70.3% of the deflection of CS2 at the same load (0.74 in.). This ratio is in agreement with the deflection ratios between SS1 and SS2, as well as SS3-CS1 and SS4-CS2. In both slabs, the increase in the load propagated the existing cracks and initiated new ones, causing reduction in the stiffness. This is observed by the changing slopes of the load-deflection plots, as it is more evident in CS2 slab. The three slopes are identified at the following load stages: before the 20 kips load, after 20 and until 57 kips, and after 57 kips for CS2. The strain of concrete in compression for CS1 does not reflect the expected behavior; the stiffness (slope of curve) should be higher than that of CS2. However, it

appears from Figure 5.10 that at the same load, CS2 has a higher concrete compressive strain than in CS1.

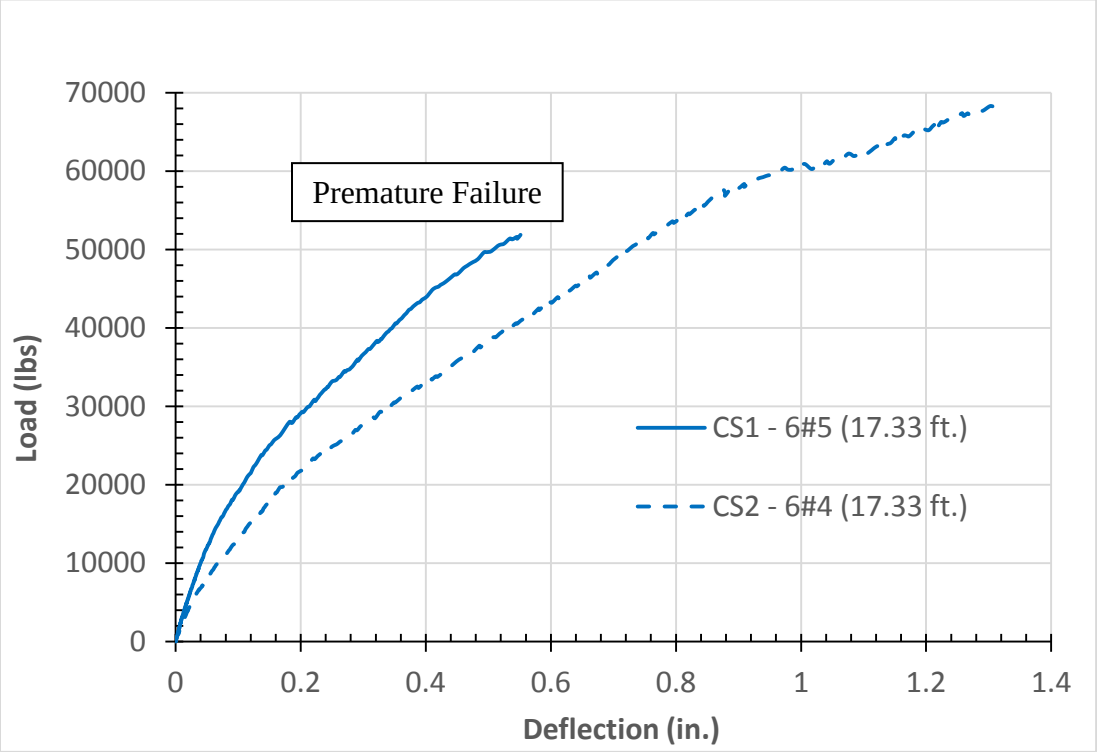

Figure 5.8. Load-Deflection Curve for CS1 and CS2

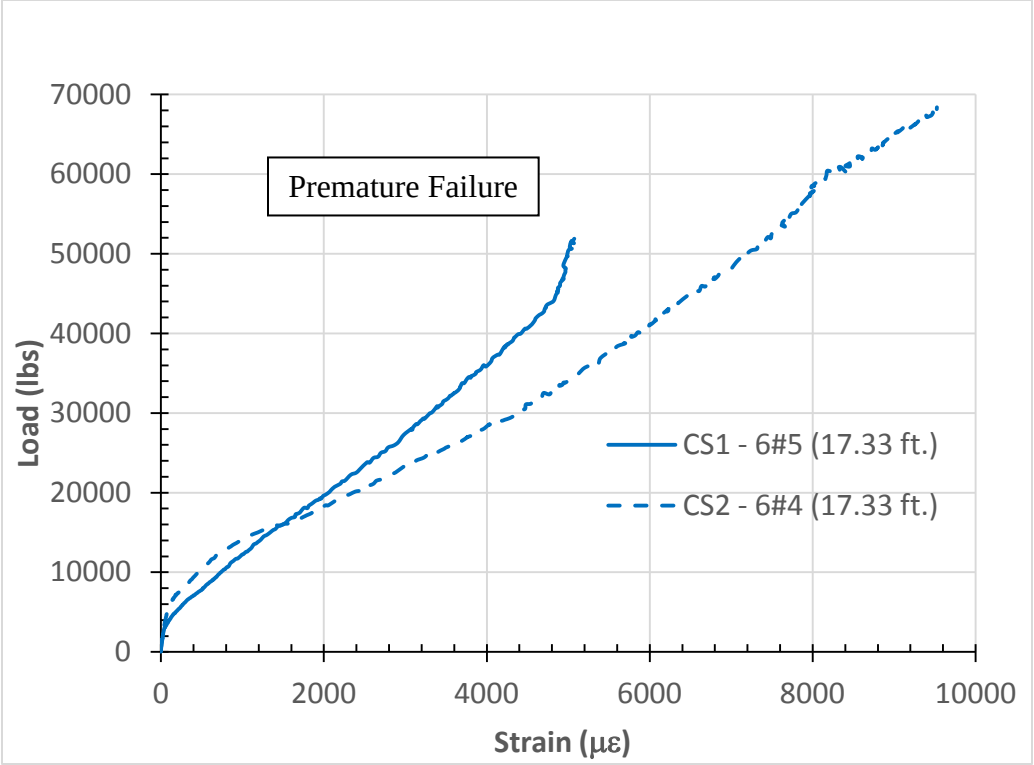

Figure 5.9. Load-Strain Curve for BFRP bars in Tension (at mid-support) for CS1 and CS2

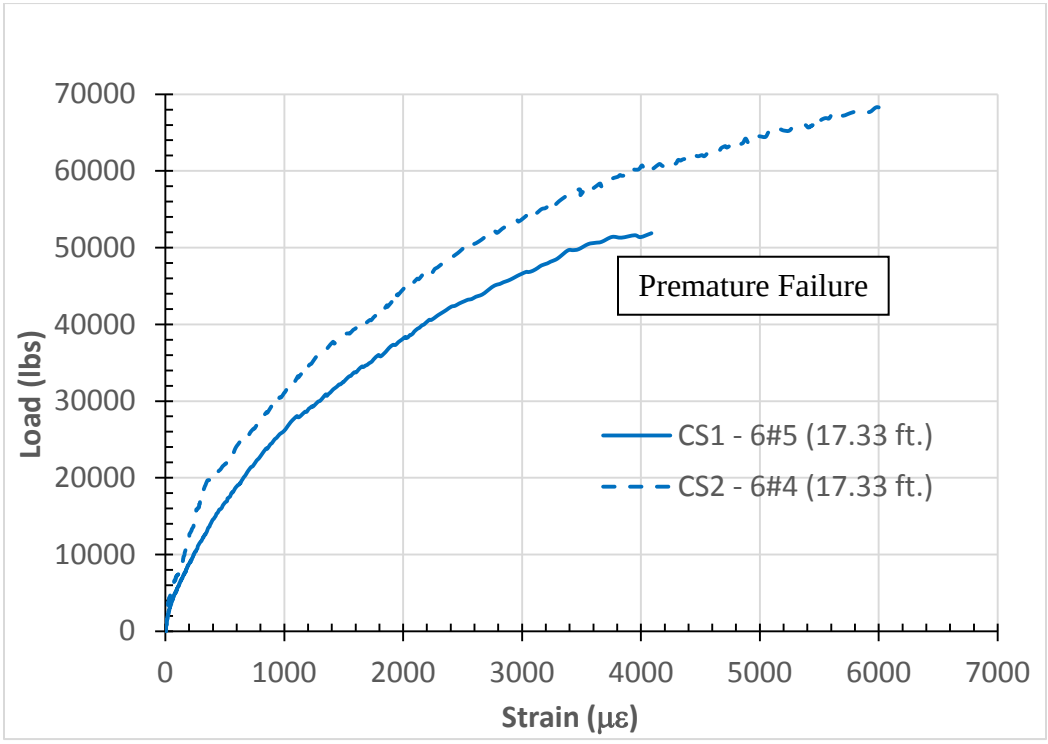

Figure 5.10. Load-Strain Curve for Concrete in Compression (at mid-support) for CS1 and CS2

5.3. Prediction of Ultimate Moment Capacity and Effective Moment of Inertia

The moment capacity and deflection of each slab were predicted based on the design equations provided in ACI 440.1R (2006) for structural NWC reinforced with FRP bars. Lightweight concrete is not addressed in the guidelines, so the equations for normal weight concrete were used. BFRP material is not included in the guidelines either, but its linearly elastic behavior until failure is similar to the FRP materials addressed in the code, which are CFRP, AFRP and GFRP. This fact, in addition to the absence of ductility in FRP materials, must be taken into consideration in the design of FRP reinforced elements. The guidelines consider working stress and strength design methods, however it follows the later to be in agreement with the ACI 318. The recommended procedure is to design the structural members based on the required strength and check for serviceability criteria. In most cases, the design is governed by serviceability to control deflection and cracks. Therefore, it is recommended by ACI 440.1R committee and other cited researches in the same guideline that the beams and slabs are designed using the over-reinforced section approach, which satisfies strength requirements as well as meeting deflection limits.

5.3.1. Ultimate Moment Capacity

The calculation of the nominal moment capacity of BFRP reinforced slabs followed the equations given in ACI 440-1R (2006) for over-reinforced members. The two introduced approaches govern the mode of failure for flexural members and are dependent on the ratio (ρ_f/ρ_{fb}). Under-reinforced sections with $\rho_f < \rho_{fb}$ fails by rupturing of the FRP bars. They are designed using Eq. 5.1 (Eq. 8.6b in ACI 440.1R (2006), which is a conservative form

of Eq. 8.6a in the guidelines; because it assumes that the maximum concrete strain of 3000 με is reached.

$$M_n = A_f f_{fu}\left(d - \frac{\beta_1 c_b}{2}\right) \qquad Eq.\ 5.1$$

$$where\ c_b = \left(\frac{\varepsilon_{cu}}{\varepsilon_{cu} + \varepsilon_{fu}}\right) d$$

On the other hand, an over-reinforced section has a (ρ_f/ρ_{fb}) ratio greater than 1 $(\rho_f > \rho_{fb})$, fails by crushing of concrete, and is designed using Eq. 5.2 (Eq. 8-4a in ACI 440.1R (2006)).

$$M_n = A_f f_f\left(d - \frac{a}{2}\right) \qquad Eq.\ 5.2$$

$$where\ a = \frac{A_f f_f}{0.85 f_c' b} \qquad Eq.5.2a$$

$$and\ f_f = E_f \varepsilon_{cu} \frac{(\beta_1 d - a)}{a} \qquad Eq.5.2b$$

Substituting Eq. 5.2a into 5.2b gives Eq. 5.2c.

$$f_f = \sqrt{\frac{\left(E_f \varepsilon_{cu}\right)^2}{4} + \frac{0.85\beta_1 f_c'}{\rho_f} E_f \varepsilon_{cu}} - 0.5 E_f \varepsilon_{cu} \le f_{fu} \qquad Eq.5.2c$$

All slabs were designed using the over-reinforced approach to satisfy serviceability requirements and to prevent rupturing of the BFRP bars.

The ultimate moment capacity is calculated by introducing the strength reduction factor (ϕ) to the nominal capacity. ACI 440.1R (2006) sets a fixed value for ϕ equal to 0.55 if $\rho_f < \rho_{fb}$, 0.65 if $\rho_f > 1.4\,\rho_{fb}$, and defines a transition zone when $\rho_{fb} < \rho_f < 1.4\,\rho_{fb}$, where

$\phi = 0.3 + 0.25\,{}^{\rho_f}/_{\rho_{fb}}$. Ovitigala and Issa (2012) reported that the previous strength reduction factors are very conservative, and can be increased to 0.74. This was confirmed based on the statistics of their study on BFRP reinforced beams and other studies (aforementioned in the literature review) for FRP reinforced flexural members.

The experimental and ACI-calculated nominal and ultimate moments for each slab are listed and compared with each other in Table 5.1.

For the simply supported slabs, the experimental moment was calculated using the moment equation for a simply supported member with a point load (P) applied at the mid-span, given by $M = {}^{PL}/_{4}$, where L is the span length. The experimental moment for the continuous slabs was calculated using structural analysis software. Since all slabs were designed with $(\rho_f/\rho_{fb}) > 1$, the ultimate moment capacities were calculated using strength reduction factor (ϕ) equal to 0.65.

Specimen ID	**Span (ft)**	**Max. Load "P" (kip)**	**Experimental Moment "M_{exp}" (kip.ft)**	**ACI Predicted Nominal Moment "M_n" (kip.ft)**	**M_n / M_{exp} (%)**	**ACI Predicted Ultimate Moment "ϕM_n" (kip.ft)**	**ϕM_n / M_{exp} (%)**
SS1	6.67	36.61	61.02	53.4	88%	34.7	57%
SS2	6.67	36.14	60.24	45.4	75%	29.5	49%
SS3-CS1	8.00	24.50	49.00	53.4	109%	34.7	71%
SS4-CS2	8.00	25.01	50.02	45.4	91%	29.5	59%
SS5-CS1	6.00	37.94	56.91	53.4	94%	34.7	61%
SS6-CS2	6.00	35.30	52.96	45.4	86%	29.5	56%
CS1**	17.33	51.86	41.9*	58.1	139%	37.8	90%
CS2	17.33	68.57	55.4	49.6	90%	32.2	58%

*** Pre-mature failure*

Table 5.1 Experimental and Predicted Nominal Moment Capacities for BFRP Reinforced Slabs

As shown in Table 5.1, for the four main specimens designed with steel stirrups to prevent early shear (SS1, SS2, CS1 and CS2), the experimental moment was around two-time the ACI-predicted ultimate moment (using $\phi = 0.65$), except for CS1 which failed prematurely. The predicted nominal moment ranged between 75 and 90% of the experimental moment for the same slabs with the exception of CS1. These results are quite similar to those found by Ovitigala and Issa (2012). For their tested beams, the predicted ultimate moment was almost double the experimental moment, and the ratio of the experimental to nominal predicted moments (M_n / M_{exp}) ranged between 77-86%.

As for the specimens taken from the continuous slabs, (M_n / M_{exp}) ratio was higher (86-109%) than that for the four main slabs. They failed at relatively lower experimental moment due to the lack of stirrups on one end to prevent early shear failure. Similarly, (M_u / M_{exp}) was also higher and ranged between 56-71%.

5.3.2. Effective Moment of Inertia

Deflection is a major criterion that controls the design of FRP structural elements, along with crack control. In most cases, satisfying the deflection limitations will also satisfy strength requirements. Calculation of the deflection is governed by the moment of inertia of the structural member. Since concrete is a heterogeneous material, its moment of inertia changes after the first crack. Hence, the effective moment of inertia (I_e) is required for estimating the deflection.

Moreover, the stiffness of the member depends on E_cI. For uncracked sections, $I = I_g$, whereas for cracked sections, $I = I_e$. ACI 440.1R and other studies provided different equations for calculating I_e. Once the value of I_e is known, the deflection can be estimated using structural analysis equations. For example, for simply supported beams with a point load in the midspan, the deflection is calculated based on Eq. 5.3.

$$\Delta = \frac{PL^3}{48E_cI_e} \qquad Eq.5.3$$

Several models are available in the literature to calculate the effective moment of inertia, and in this section, 4 different models are compared with the experimental value of I_e for all simply supported slabs. The first is the universally adopted model used by ACI 318 (2011) and ACI 440.1R (2006), which is based on Branson's equation (1977) shown in Eq. 5.4

$$I_e = \left(\frac{M_{cr}}{M_a}\right)^3 I_g + \left[1 - \left(\frac{M_{cr}}{M_a}\right)^3 \right] I_{cr} \leq I_g \qquad Eq.\ 5.4$$

M_{cr} is the applied moment and M_{cr} is the cracking moment (Eq. 5.5)

$$M_{cr} = {f_r I_g}/{y_t} \qquad Eq.5.5$$

and f_r is the modulus of rupture which is calculated theoretically using $f_r = 7.5\sqrt{f_c'}$.

I_{cr} corresponds to the moment of inertia of the cracked section, calculated for all models as shown

in Eq. 5.6

$$I_{cr} = \frac{bd^3}{3} k^3 + n_f A_f d^2 (1-k)^2 \qquad Eq. 5.6$$

where $k = \sqrt{2\rho_f n_f + (\rho_f n_f)^2} - \rho_f n_f$

n_f is the modular ratio of the reinforcement to concrete (E_f / E_c).

The second model is Bischoff's equation (2007) presented in Eq. 5.7 below:

$$I_e = \frac{I_{cr}}{1 - (1 - \frac{I_{cr}}{I_g})(\frac{M_{cr}}{M_a})^2} \leq I_g \qquad Eq. 5.7$$

Gao et al (1998a) modified Branson's Equation in ACI 318 and ACI 440.1R by the factor β_d to reduce the effect of tension stiffening in that formula. ACI 440.1R recommended a simpler and more conservative equation for β_d, as shown in Eq. 5.8 and 5.9.

$$I_e = \left(\frac{M_{cr}}{M_a}\right)^3 \beta_d I_g + \left[1 - \left(\frac{M_{cr}}{M_a}\right)^3\right] I_{cr} \leq I_g \qquad Eq. 5.8$$

$$\beta_d = \frac{1}{5}\left(\frac{\rho_f}{\rho_{fb}}\right) \leq 1.0 \qquad Eq. 5.9$$

Alsayed et al (2000) replaced the cubic form of Branson's formula with the power "*m*", with *m* equal to 5.5 in order to correlate with service loads. Eq. 5.10 displays the modification.

$$I_e = \left(\frac{M_{cr}}{M_a}\right)^m I_g + \left[1 - \left(\frac{M_{cr}}{M_a}\right)^m\right] I_{cr} \leq I_g \qquad Eq. 5.10$$

Where $m = \dfrac{log\left(\frac{I_e - I_{cr}}{I_g - I_{cr}}\right)}{log\left(\frac{M_{cr}}{M_a}\right)}$

The four models are then compared with the experimental effective moment of inertia, $I_{e,\,eff}$ by substituting the experimental results of the load and deflection for each span, as shown in Eq. 5.11.

$$I_e = \frac{PL^3}{48E_c\Delta} \qquad Eq.5.11$$

The comparison between the four models and the experimental I_e is presented for each simply supported slab by plotting the effective moment of inertia (I_e) versus the ratio between the applied and cracking moments (M_a / M_{cr}). Such presentation allows for comparison between the results in other research, and is shown in Figures 5.11 to 5.16. The trend of all experimental plots followed the average trend of the predicting model with some deviation. For all slabs, I_e remains equal to I_g until the first crack occurs, that is when M_a equals M_{cr}, which was calculated using the theoretical cracking moment. Since all slabs have the same cross section, I_g was equal in all cases. The minimum value of I_e was equal to I_{cr} and was reached by all predicting models approximately after M_a / M_{cr} exceeded 4. It appears from the plots of all specimens in Figures 5.11 to 5.16 that all models underestimated the value of I_e after M_a / M_{cr} exceeds 2.5, which in return overestimates the predicted deflection values. The model proposed by ACI 440.1R (2006) had the least deviation when compared with the experimental results. Ovitigala and Issa (2012) reported that the ACI 440.1R (2006) and Bischoff (2007) were able to predict the deflection better than other models. However, this is not the case for the specimens in this study, which could be explained by the fact that none of the specimens reached their ultimate flexural capacity due to shear failure, whereas in their study, the beams were provided with shear reinforcement along the whole span. Finally, the gross moment of inertia (I_g) for the beams tested by Ovitigala and Issa (2012) was 1.5 times that of the slabs, due to the greater depth. The slabs that were

taken from the continuous specimens displayed a sudden drop in I_e when M_a / M_{cr} slightly exceeded a value of 1, as shown in Figures 5.13 to 5.16. This is expected because their section was already cracked.

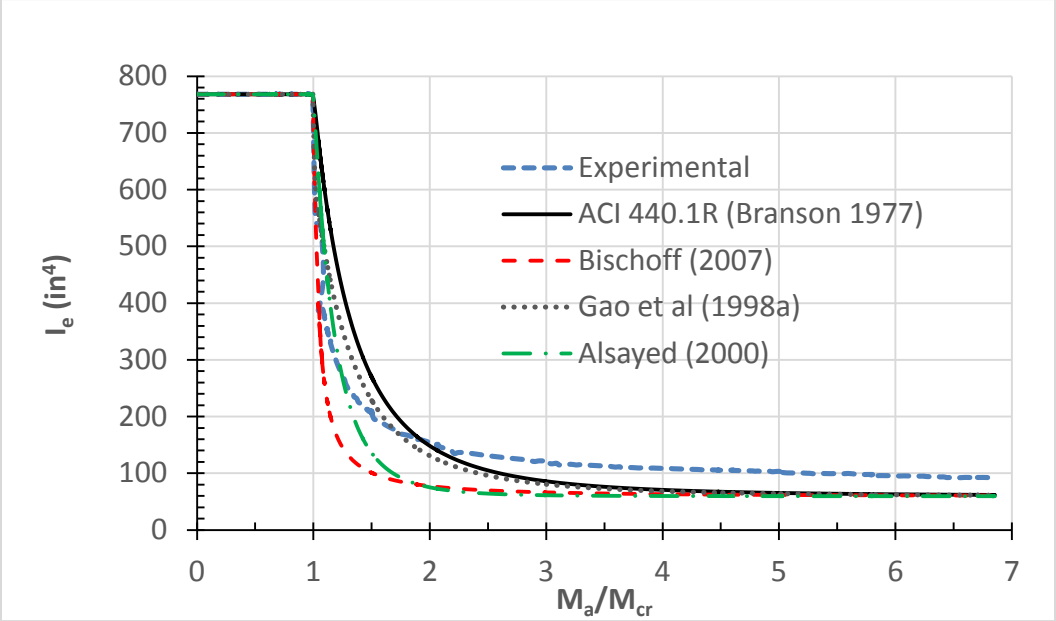

Figure 5.11. Effective Moment of Inertia vs. M_a / M_{cr} for Specimen SS1

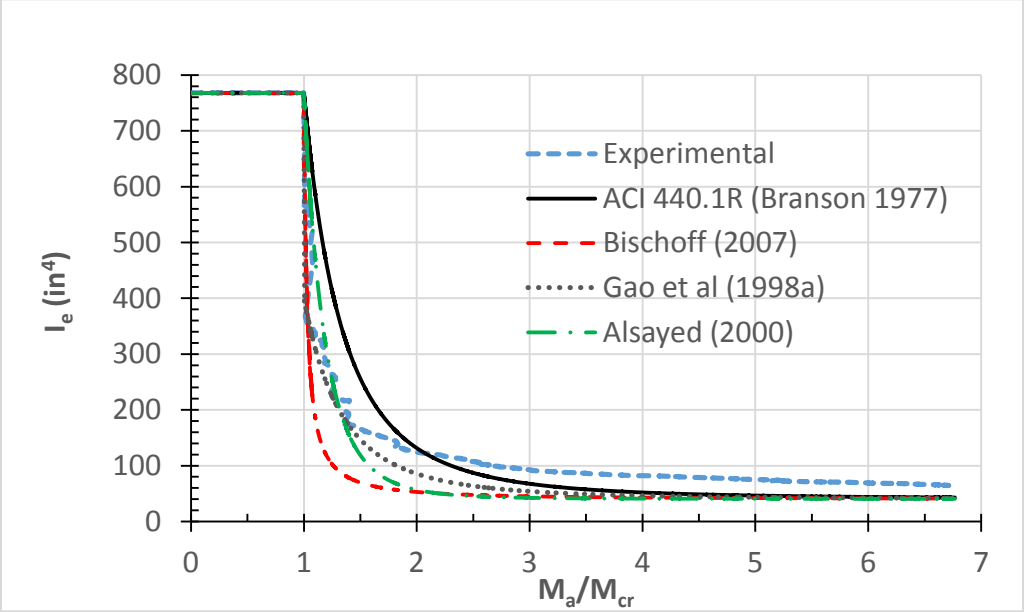

Figure 5.12. Effective Moment of Inertia vs. M_a / M_{cr} for Specimen SS2

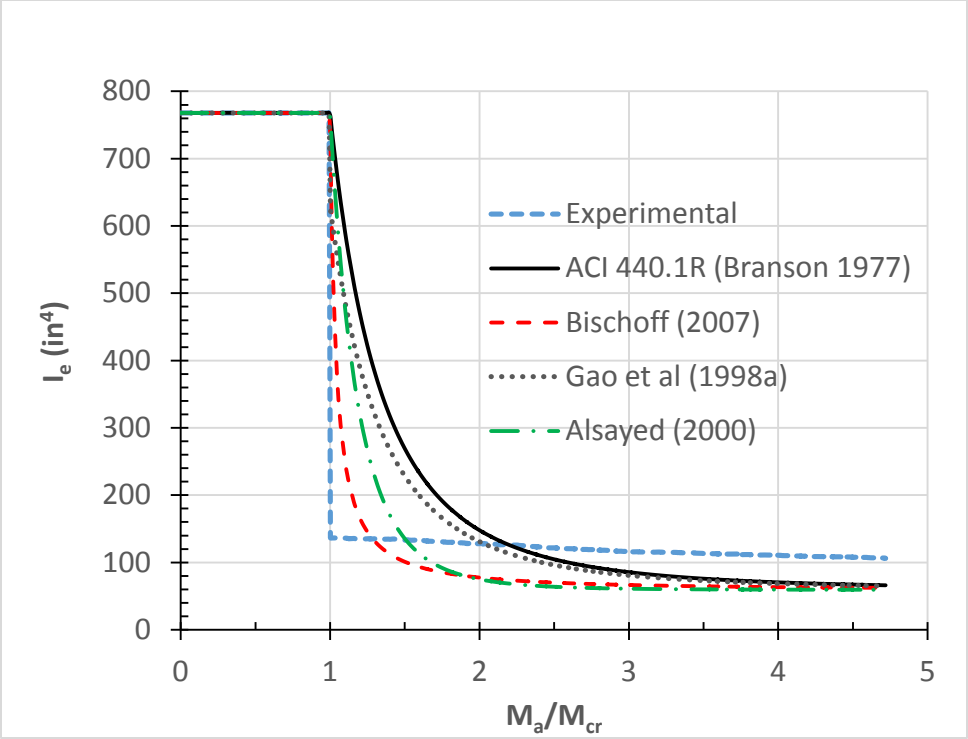

Figure 5. 13. Effective Moment of Inertia vs. M_a / M_{cr} for Specimen SS3-CS1

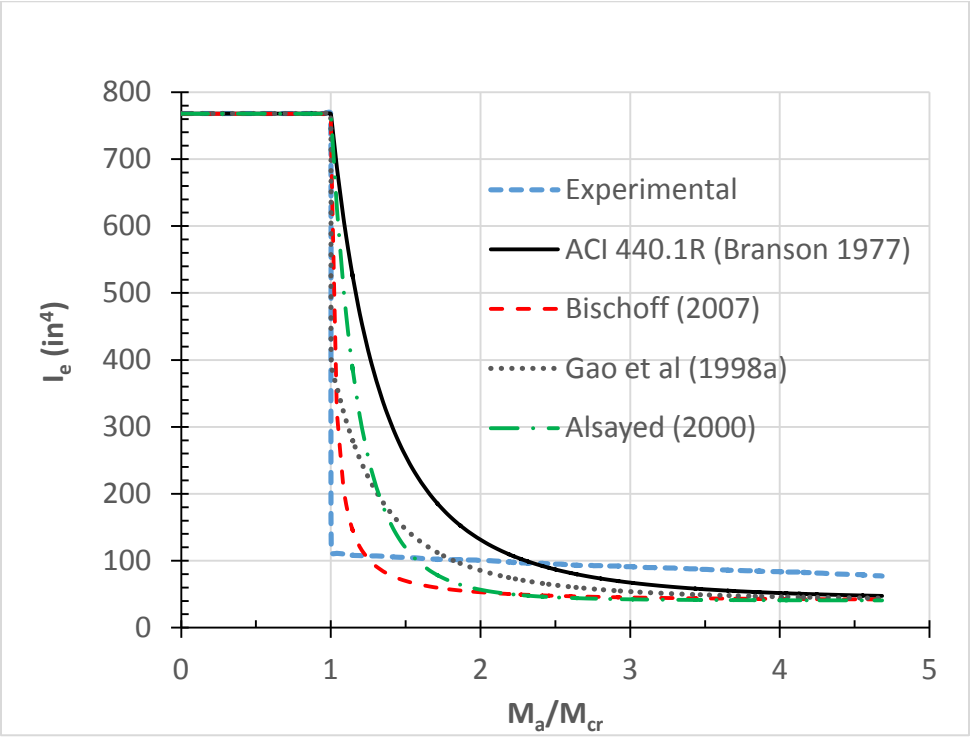

Figure 5.14. Effective Moment of Inertia vs. M_a / M_{cr} for Specimen SS4-CS2

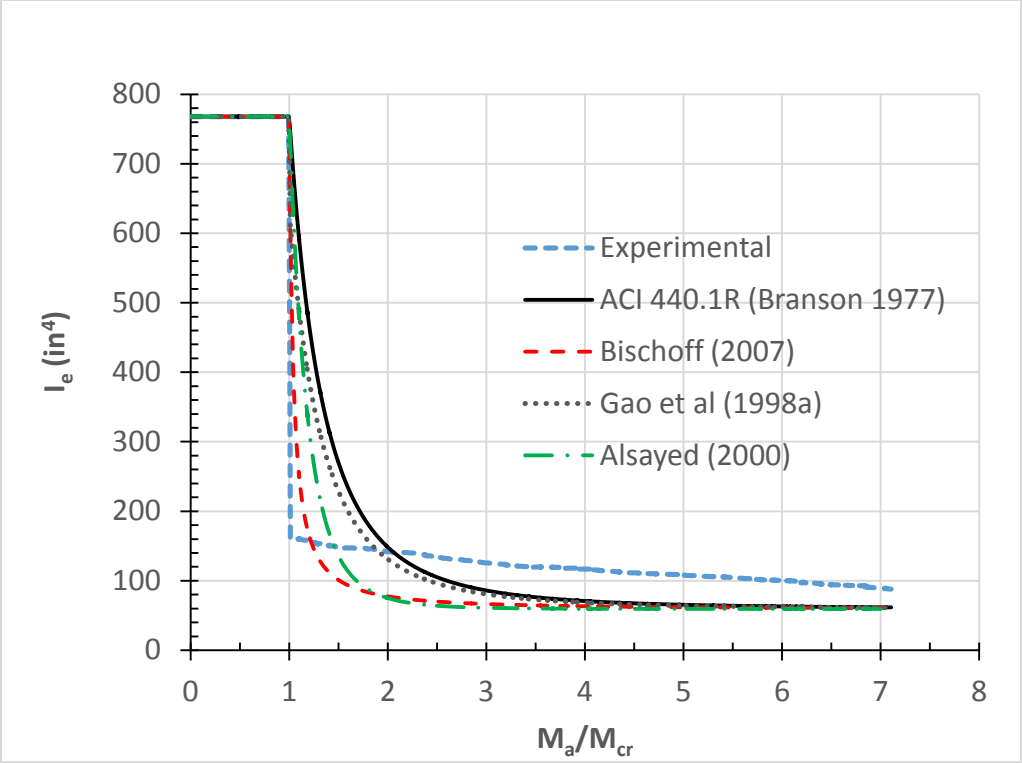

Figure 5.15. Effective Moment of Inertia vs. M_a / M_{cr} for Specimen SS5-CS1

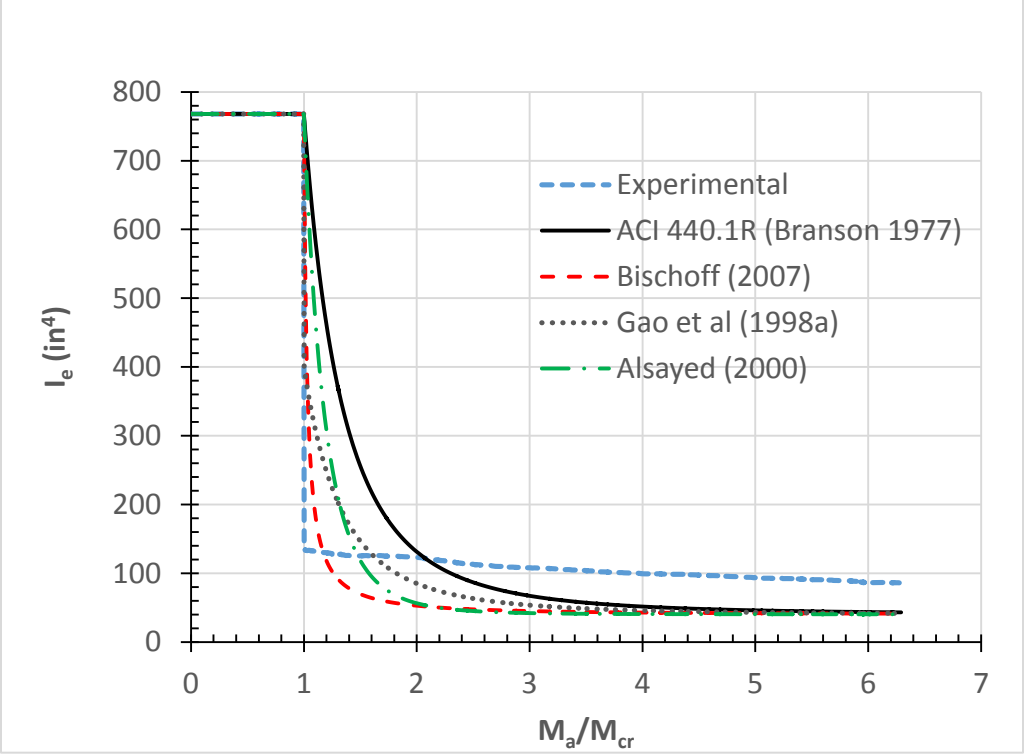

Figure 5.16 Effective Moment of Inertia vs. M_a / M_{cr} for Specimen SS6-CS2

CHAPTER 6
FINITE ELEMENT ANALYSIS

This chapter includes a brief description of the finite element model used to analyze the testing of the slabs by utilizing ANSYS Software (Release 11.0). At first, the purpose of this analysis was to predict the ultimate capacity and maximum deflection for the first tested slab, SS1. Then, the results were used to calibrate the models for the other slabs. The finite element results are compared with the experimental results of each specimen.

6.1. Materials

6.1.1. Concrete

SOLID65 element was used to simulate the concrete volume. The element is defined by eight nodes having three degrees of freedom at each node, translations in the nodal x, y, and z directions. Solid65 has capabilities of simulating cracking and crushing of concrete. A uniaxial multi-linear stress-strain data from cylinder test was used to define the concrete in compression. The compressive strength for concrete (f_c') was set to equal 6000 psi in order to calibrate the models.

The failure criteria of concrete (cracking and crushing) was defined by Willam and Warnke's five parameter model: uniaxial tensile cracking stress (f_t), uniaxial crushing stress (f_c'), Shear transfer coefficient for an open crack (β_t), Shear transfer coefficient for a closed crack (β_c), and Stiffness multiplier for cracked tensile condition (ANSYS 11.0 User's Manual).

The shear transfer coefficient, β_t, represents conditions of the crack face. The value of β_t ranges from 0.0 to 1.0, with 0.0 representing a smooth crack and 1.0 representing complete shear transfer. Shear transfer coefficient for a closed crack βc determines the amount of shear

transferred across the cracks and it varies from 0 to 1.0 (ANSYS 11.0 User's Manual). Kachlakev and McCurry (2000) reported that values of β_t less than 0.2 encountered divergence problems. In this study, a value of $\beta_t = 0.3$ was used for shear transfer coefficient for open crack and $\beta_c = 0.9$ was used for shear transfer coefficient for close crack. If both cracking and crushing capabilities are active in ANSYS software, fictitious crushing of concrete may be encountered due to excessive cracking strain to the orthogonal uncracked direction through Poisson's effect which leads to divergence problem (Zhou et al., 2004 and Si et al., 2008). They also stated that the crushing capability of concrete was turned off to avoid fictitious crushing. In this study, crushing capability of concrete was also ignored by setting uniaxial crushing stress $(f_c') = -1$. A value of 0.2 was used for Poisson's ratio of concrete.

6.1.2. BFRP Rebars

BFRP rebars were modeled using LINK8 element. The three-dimensional LINK8 element is a uniaxial tension-compression element with three degrees of freedom at each node: translations in the nodal x, y, and z directions. Basalt FRP material is assumed to be perfectly elastic material identical in both tension and compression with an elastic modulus equal to $7x10^6$ psi and a poisson's ratio of 0.3. The interface between concrete element and LINK8 element was assumed to be fully bonded.

6.2. Supports and Loading Plate

Both the support plate and loading plate were modeled using SOLID45 element. SOLID45 element is defined by eight nodes having three degrees of freedom at each node, i.e., translations in the nodal x, y, and z directions. Both support plate and loading plate were assumed to be perfectly elastic materials.

6.3. Loading and Boundary Conditions

The slabs are assumed to be fully rest on steel plates. Half and quarter symmetry boundary conditions were used to reduce the mesh volume and save computation time, as shown in Figures 6.1 and 6.2 for the simply supported and continuous slabs, respectively. The load was applied as pressure load on the 20 x 8 x 1.5 in. loading plate. The nonlinear finite element analysis is performed assigning both force and displacement tolerance criteria, defined as 0.5% for the force and 5% for the displacement.

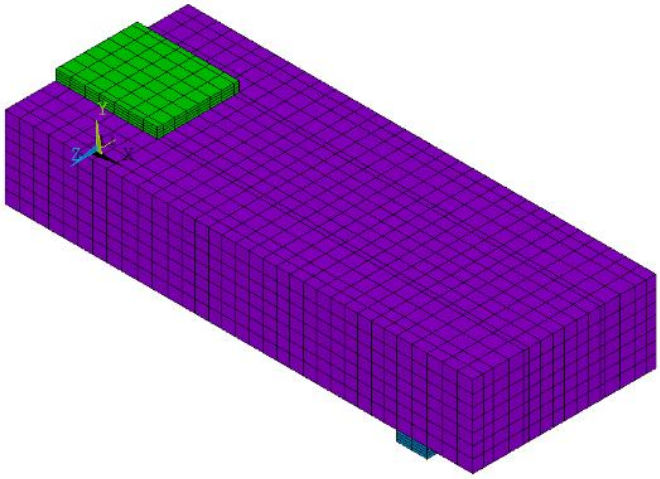

Figure 6. 1. Half Symmetry Model for Simply Supported Slabs

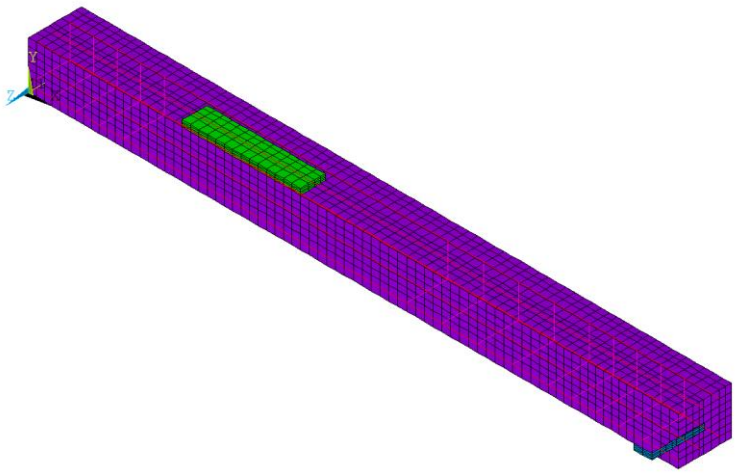

Figure 6. 2. Quarter Symmetry Model for Continuous Slabs

6.4. Finite Element Results

For each specimen, the experimental results of the deflection, strain in BFRP rebars in tension, strain of concrete in compression and tension were compared with those obtained from the finite element analysis. In general, the analytical results conformed to the experimental data.

6.4.1. Simply Supported Slabs SS1 and SS2

Finite element (FE) analysis was able to predict the deflection at ultimate load in high accuracy for both specimens SS1 and SS2. The ratio between finite element and experimental deflection was 88% and 97% for slabs SS1 and SS2, respectively (Figure 6.3). Similarly, the tensile strain in BFRP reinforcement is also well estimated by the FE analysis; 99% of the experimental value was predicted by the model of SS1, whereas the analysis for SS2 overestimated the experimental strain at ultimate load by only 7%, with high accuracy for the whole range of the testing load for both specimen as shown in Figure 6.4. Likewise, the FE results for the strain of concrete in compression were quite comparable with the experimental results as displayed in Figure 6.5; a slight overestimation of 5% for SS1 SS2 at ultimate loads. For the whole range of the load, the

maximum variation for SS2 was 18%. Moreover, the load at which the first crack occurs and the concrete tensile strain were predicted with high precision for both SS1 and SS2, as shown in Figure 6.6. The deflected shape and crack mapping for the two specimens are shown in Figures 6.7 to 6.10.

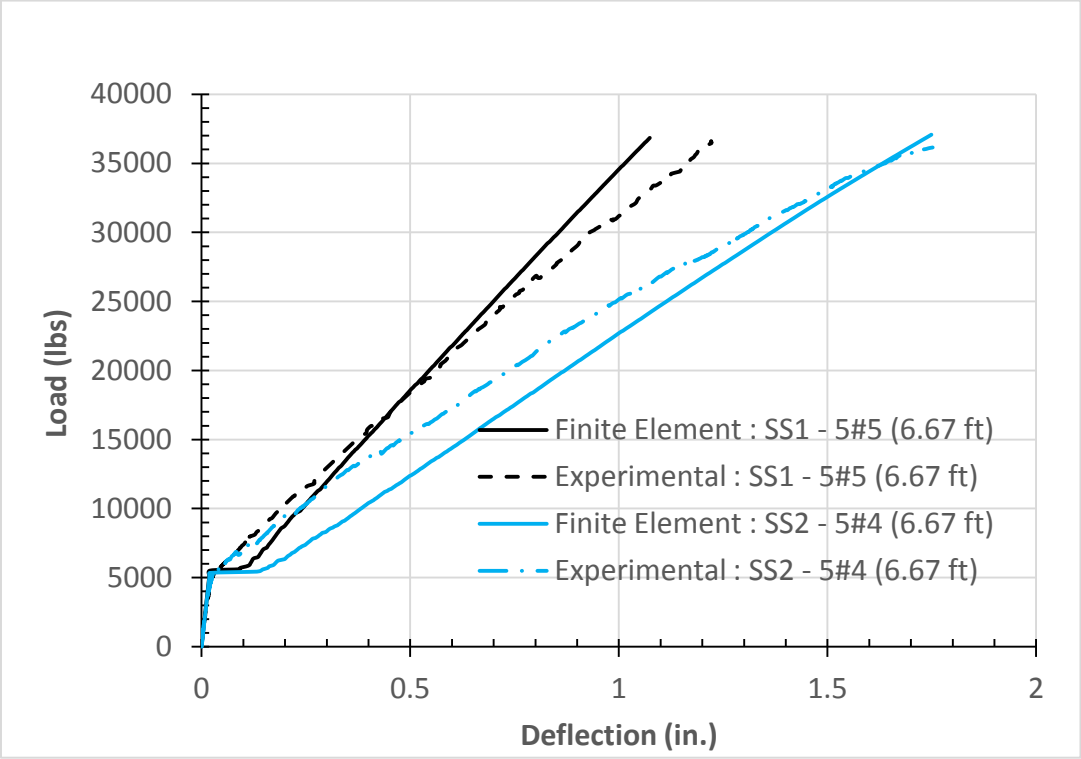

Figure 6.3. Load-Deflection Curve - SS1 & SS2 (Experimental vs. Finite Element)

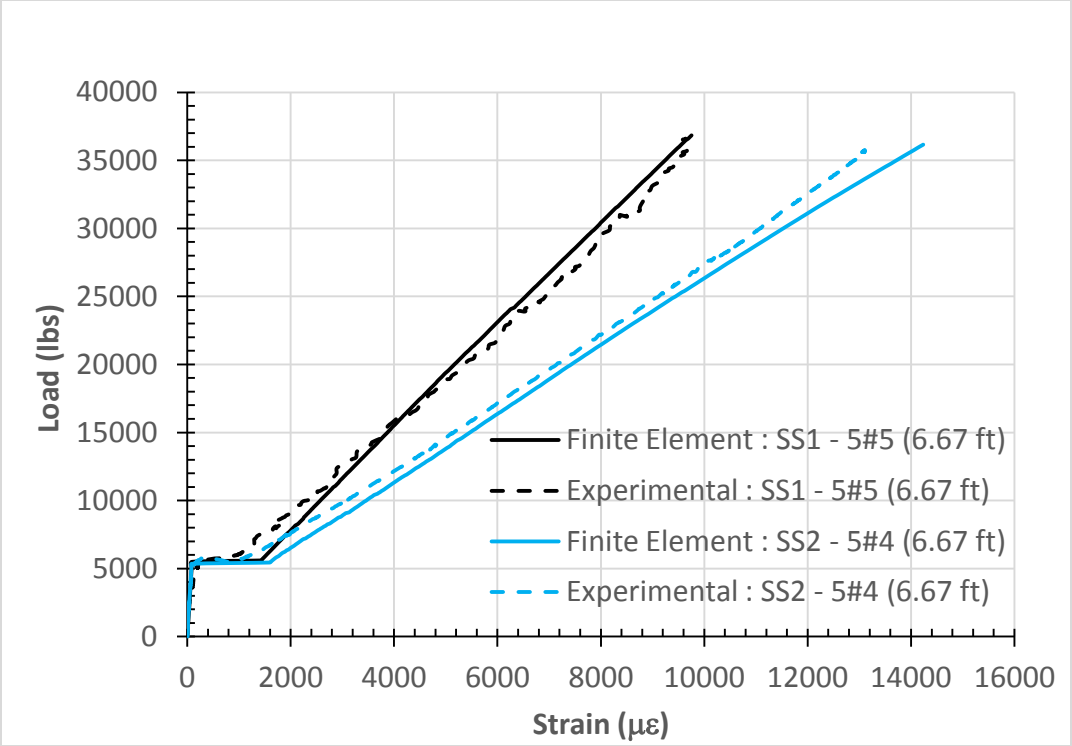

Figure 6.4. Load-Strain Curve for BFRP Rebars - SS1 & SS2 (Experimental vs. Finite Element

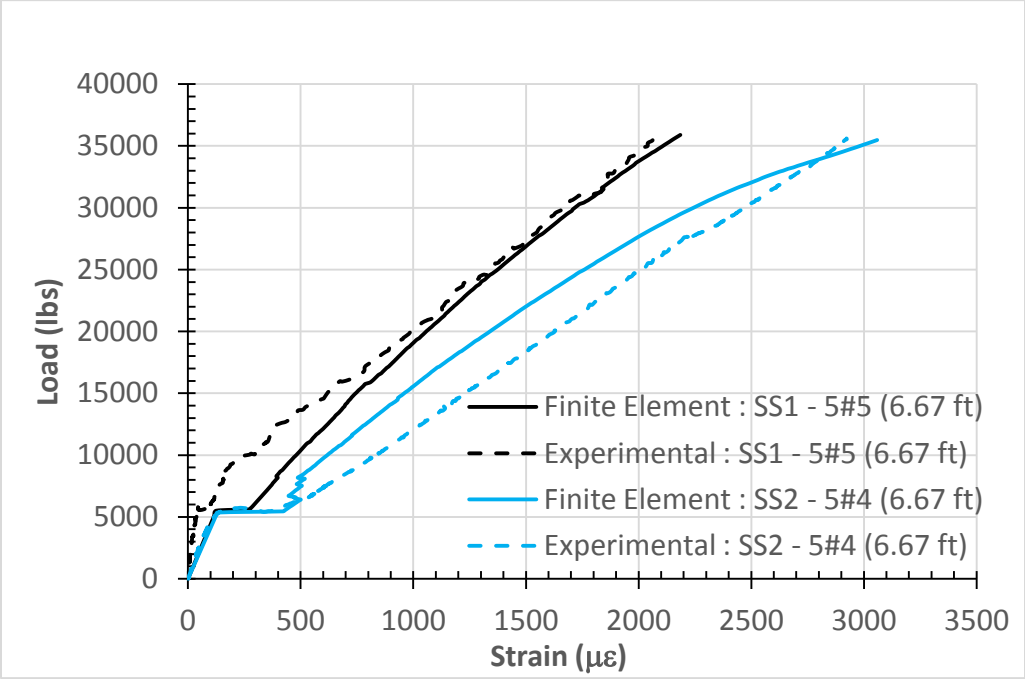

Figure 6.5. Load-Strain Curve for Concrete in Compression - SS1 & SS2 (Experimental vs. Finite Element)

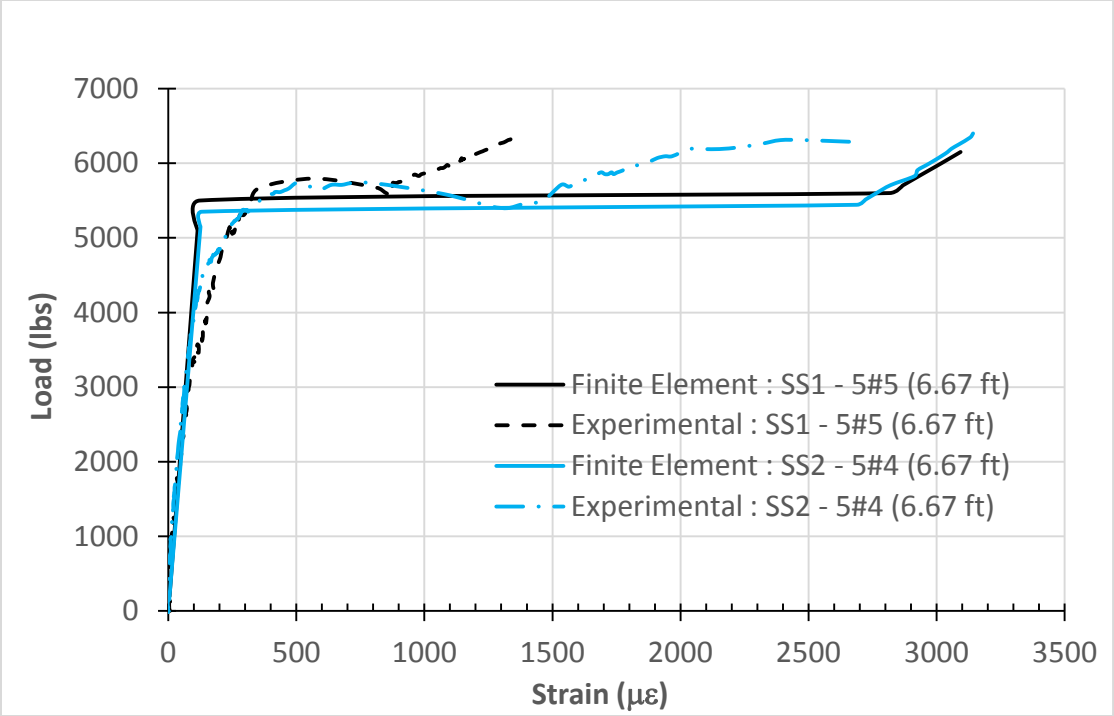

Figure 6.6. Load-Strain Curve for Concrete in Tension - SS1 & SS2 (Experimental vs. Finite Element)

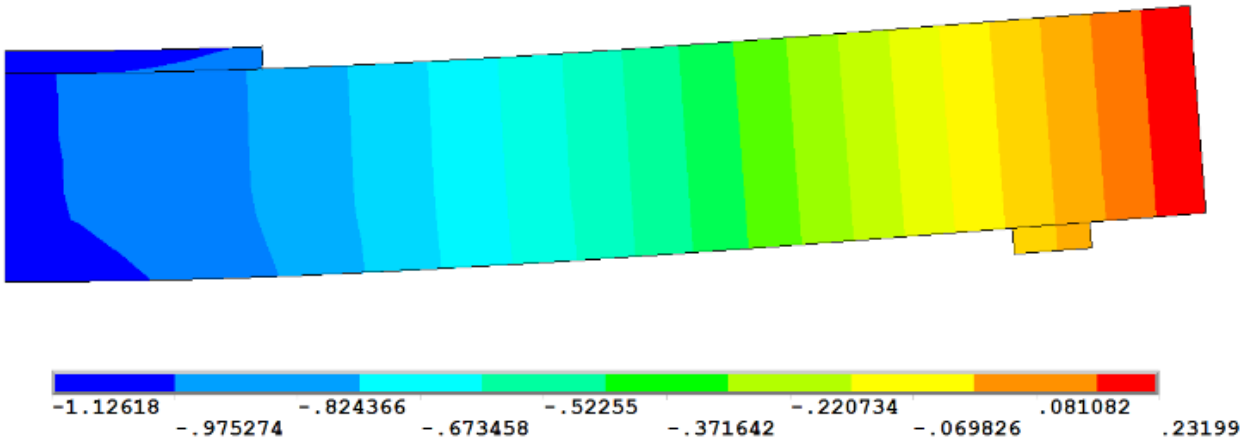

Figure 6.7. Deflection (in.) of Slab SS1 - Finite Element Analysis

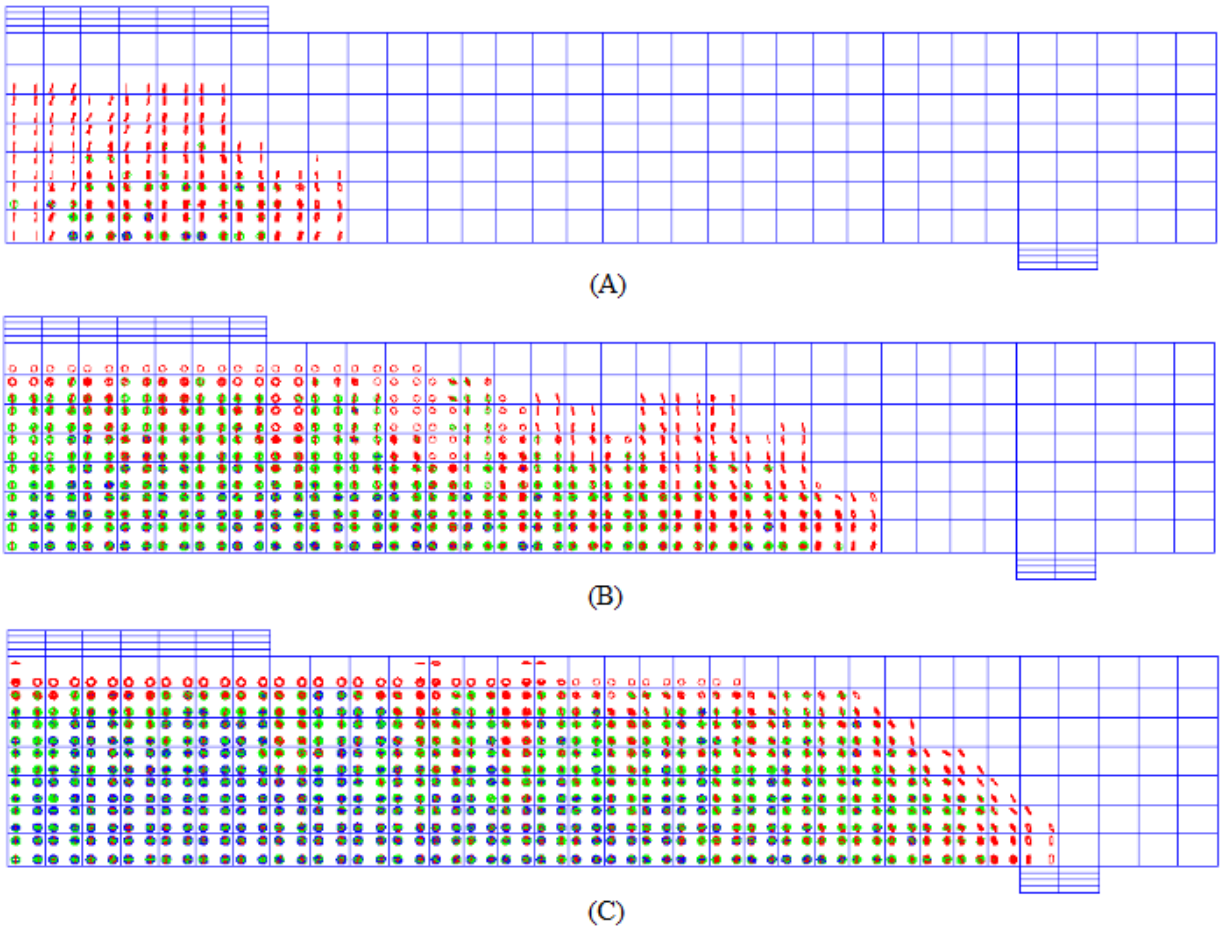

Figure 6.8. Cracking Map for Slab SS1 at (A) Crack Initiation (B) 50% Ultimate Load (C) Ultimate Load

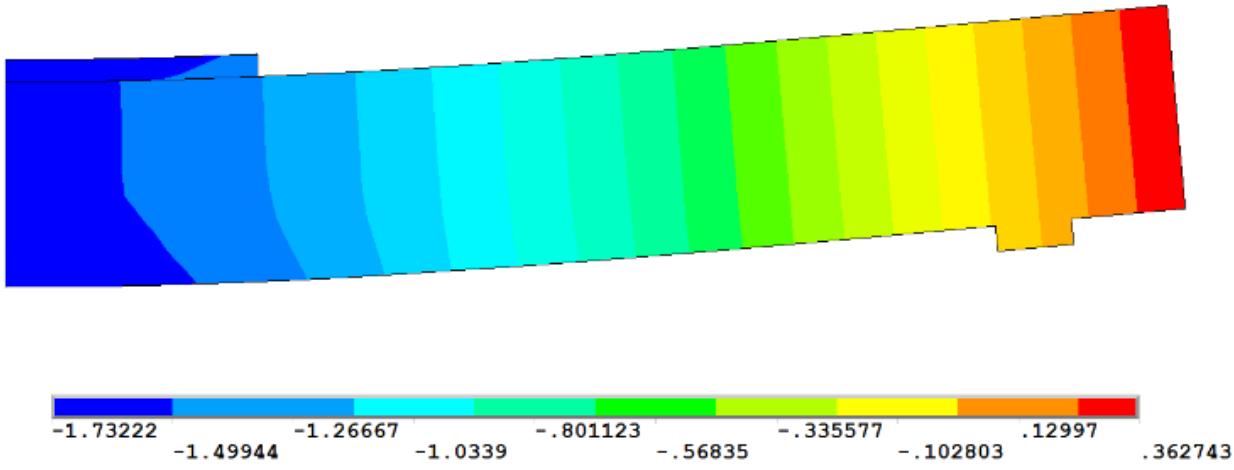

Figure 6.9. Deflection (in.) of Slab SS2 - Finite Element Analysis

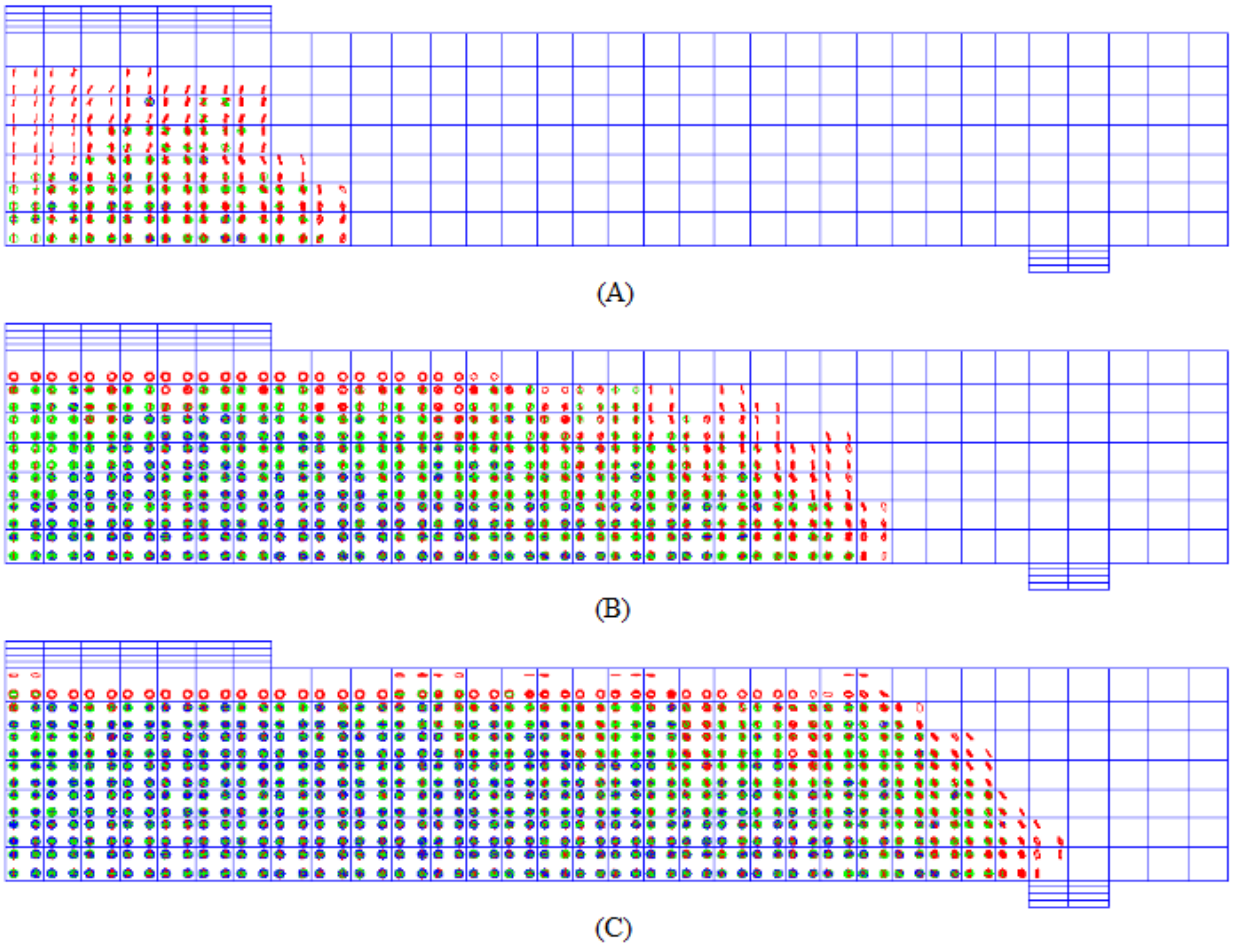

Figure 6.10. Cracking Map for Slab SS2 at (A) Crack Initiation (B) 50% Ultimate Load (C) Ultimate Load

6.4.2. Continuous Slabs CS1 and CS2

The experimental and finite element analysis load-deflection curves for the continuous specimens are shown in Figure 6.11. Slab CS1 failed prematurely, hence the curve stops at a lower load than Slab CS2. At the failure load of CS1, the finite element to the experimental deflection ratio is 94%. However, if the curve was to continue to higher loads, a trend line would reveal that the accuracy would be lower, such as the case for slab CS2. At the same load for CS2, the ratio of finite element model to experimental deflection is 98%, which is also a very accurate prediction. As the experimental load increases, the stiffness of the slab is reduced due to

excessive cracking, and the finite element model can no longer achieve that precision; the ratio drops to 79%.

The load-strain curve displayed in Figure 6.12 indicates that the models overestimated the strain in the BFRP reinforcement at ultimate load by 26% for CS1 and 15% for CS2, however the predicted values was more accurate at loads less than 50 kips for SS1 and 60 kips for SS2.

The estimated compressive strain in concrete by the FE analysis was also acceptable for specimen CS2; slightly overestimated until a load of 40 kips, and underestimated after that with an accuracy of 85% at ultimate load. As for CS1, the experimental results are suspected to be erroneous since they show unrealistically lower stiffness and higher concrete compressive strain compared to CS2, and as a result, the FE results do not fit in.

There were no distinctive cracking loads in the experimental results for both slabs to compare with the finite element model. Figure 6.14 shows that the stiffness (slope of the curve) of CS1 followed the model's slope only until a load value of 2 kips. The change in stiffness indicates an early beginning of unseen crack initiation. The stiffness of slab CS2 remained consistent with the model until a load value of 6 kips. The deflected shape and crack mapping for the two continuous slabs are shown in Figures 6.15 to 6.18.

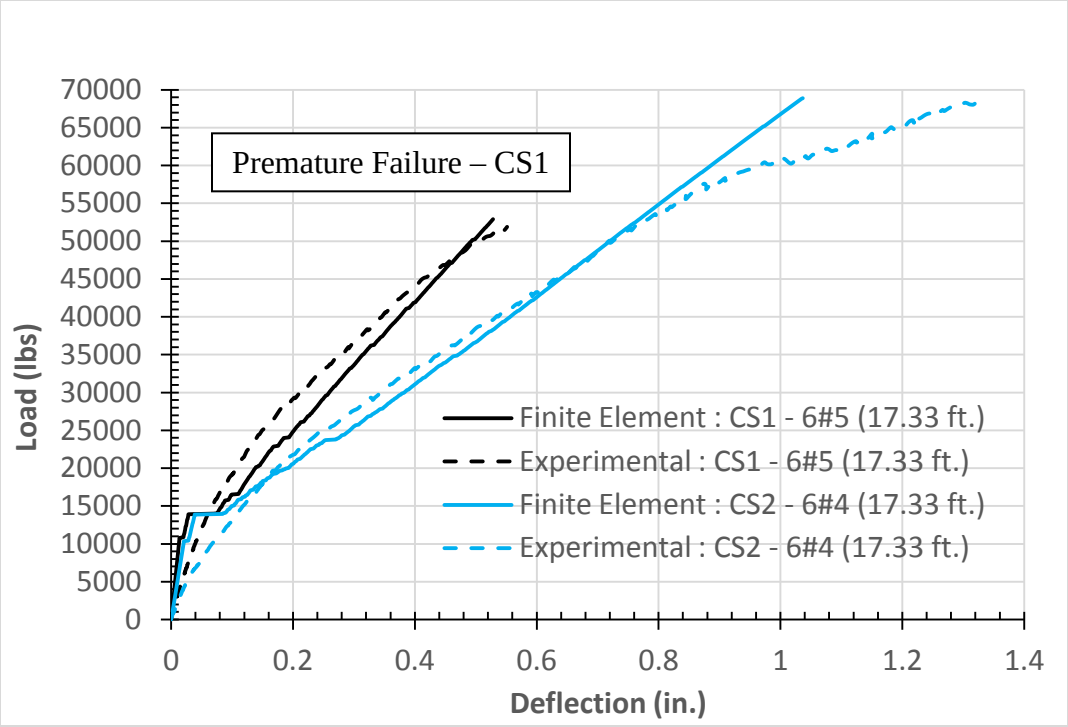

Figure 6.11. Load-Deflection Curve - CS1 & CS2 (Experimental vs. Finite Element)

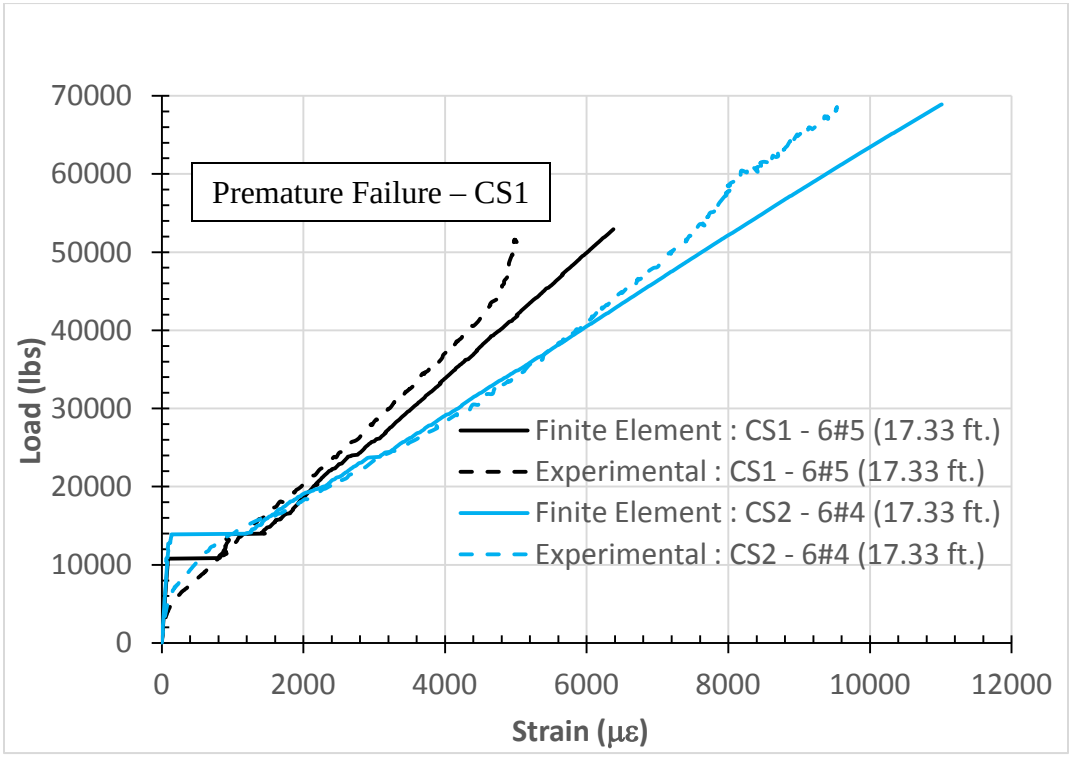

Figure 6.12. Load-Strain Curve for BFRP Rebars - CS1 & CS2 (Experimental vs. Finite Element)

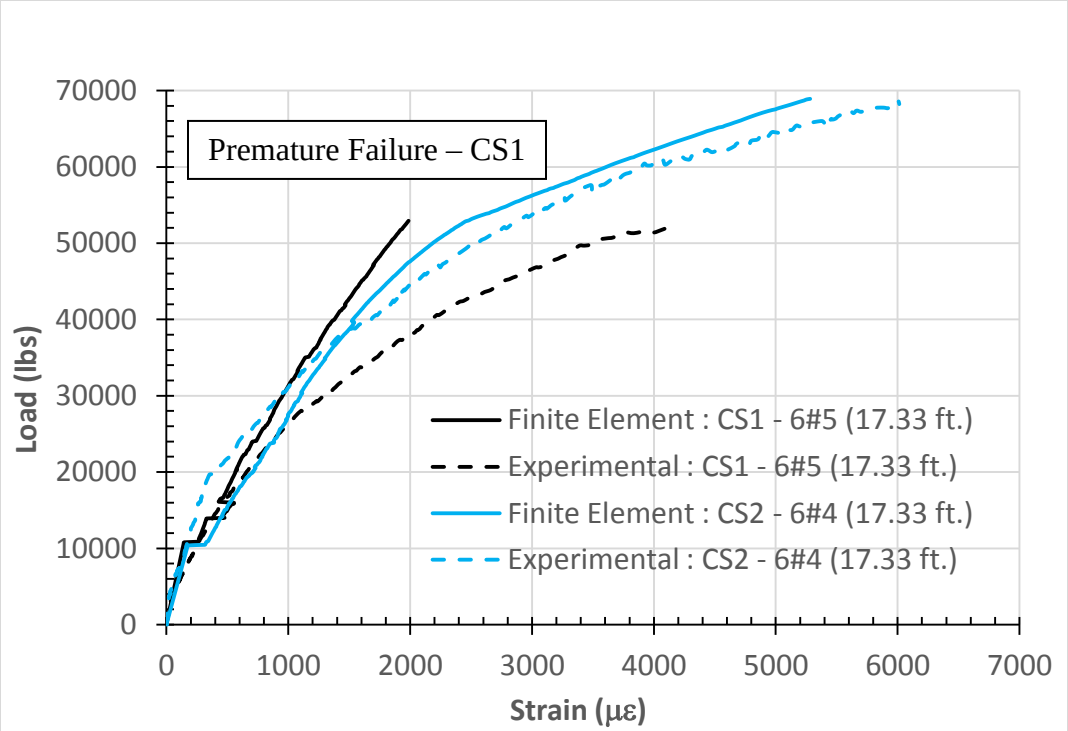

Figure 6.13. Load-Strain Curve for Concrete in Compression - CS1 & CS2 (Experimental vs. Finite Element)

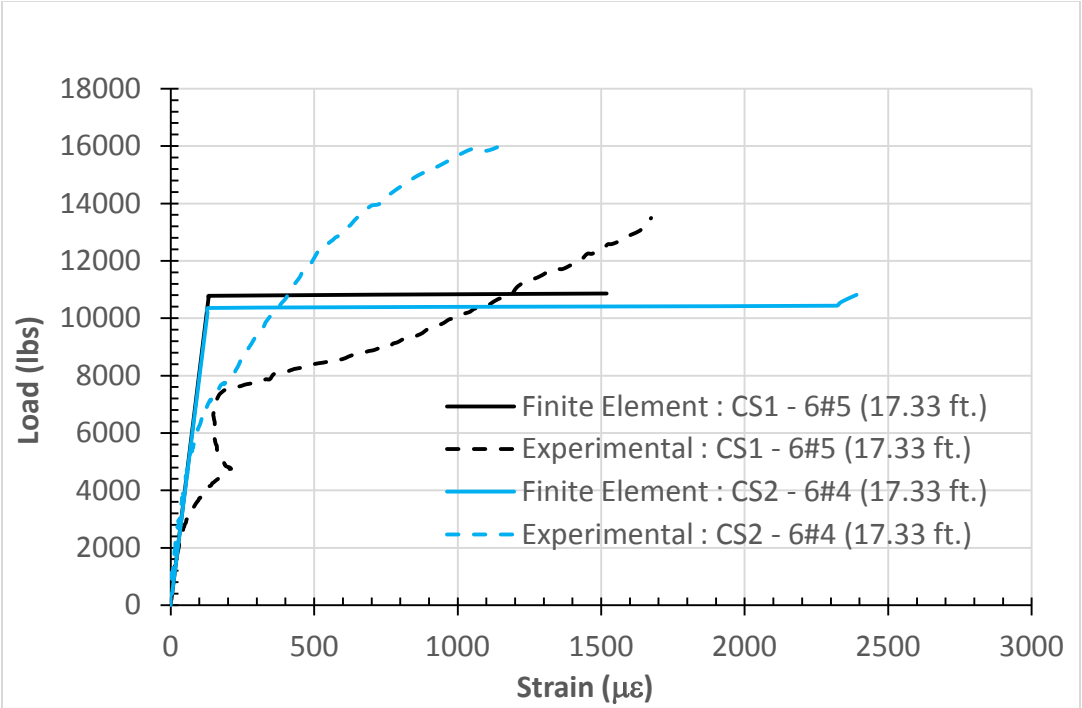

Figure 6.14. Load-Strain Curve for Concrete in Tension - CS1 & CS2 (Experimental vs. Finite Element)

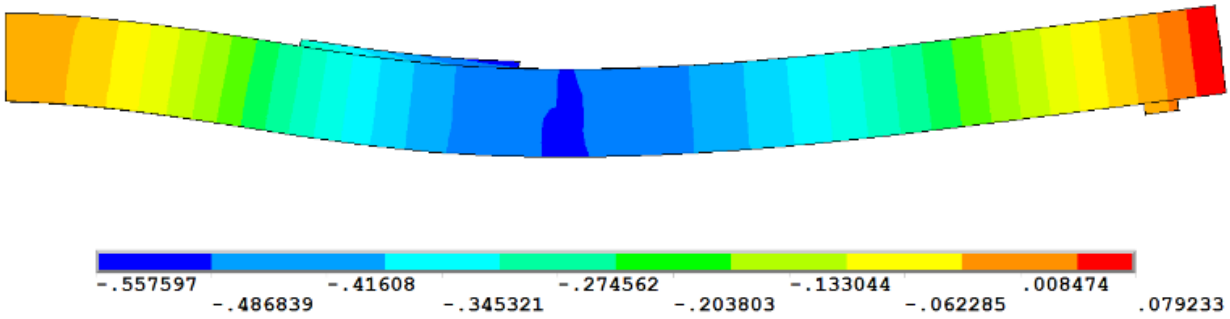

Figure 6.15. Deflection (in.) of Slab CS1 - Finite Element Analysis

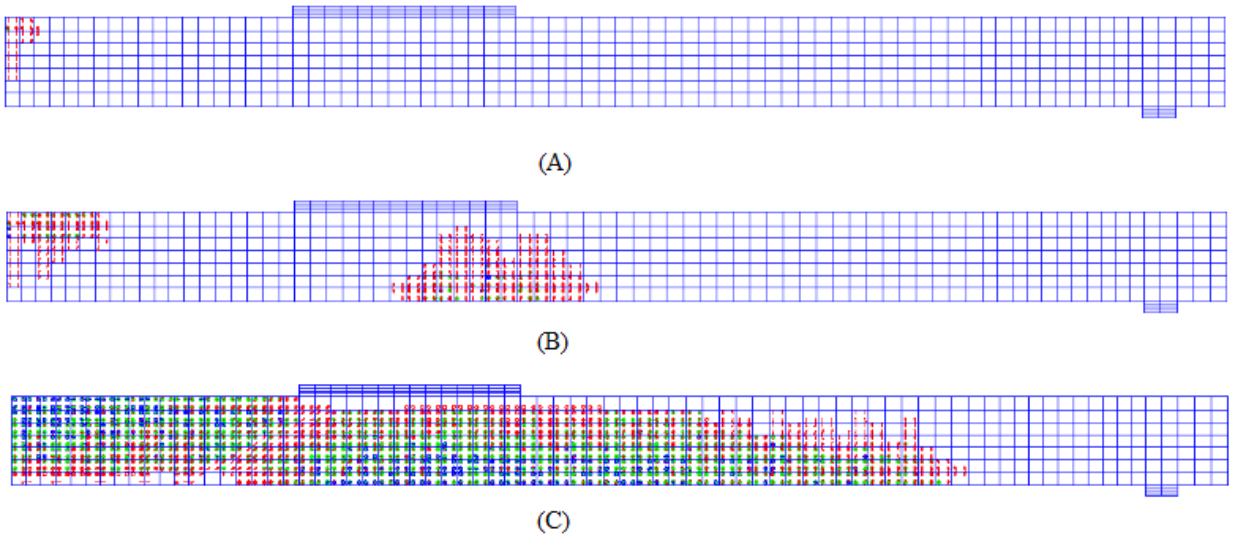

Figure 6.16. Cracking Map for Slab CS1 at (A) Crack Initiation (B) 50% Ultimate Load (C) Ultimate Load

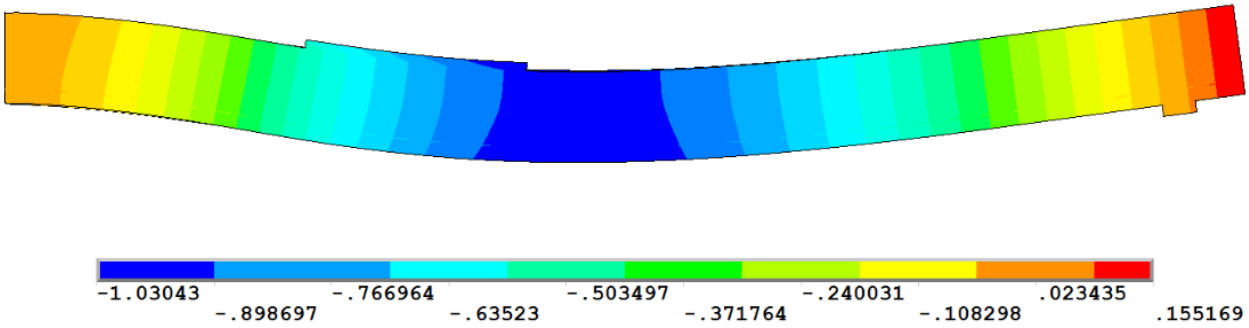

Figure 6. 17. Deflection (in.) of Slab CS2 - Finite Element Analysis

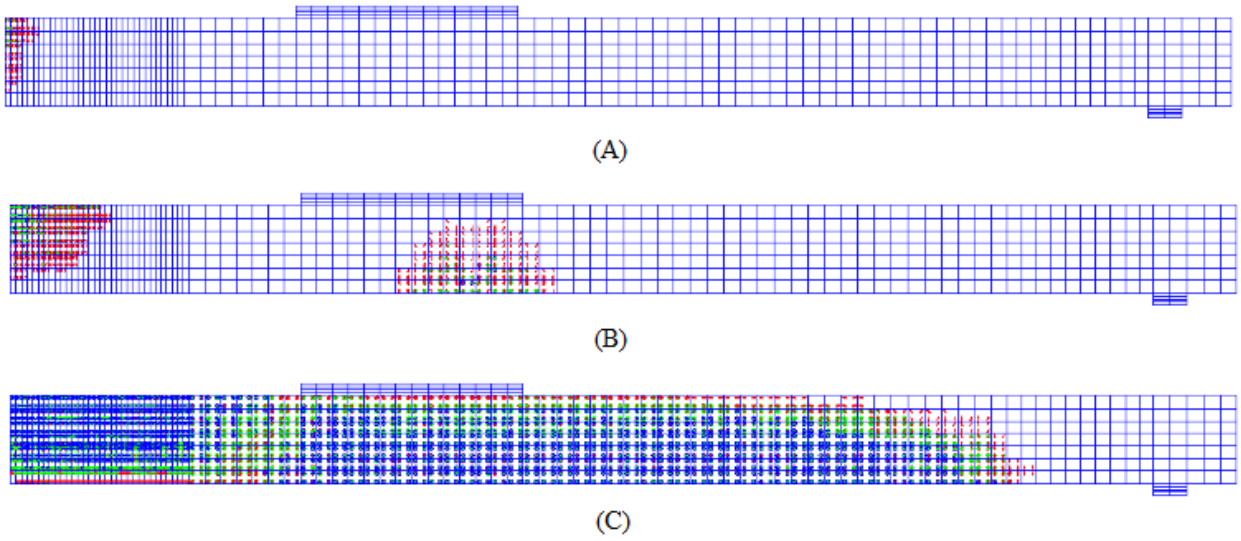

Figure 6.18. . Cracking Map for Slab CS1 at (A) Crack Initiation (B) 50% Ultimate Load (C) Ultimate Load

CHAPTER 7
SUMMARY AND CONCLUSION

A total of eight lightweight concrete slabs, 8-inch thick, reinforced with BFRP bars were tested with three different parameters; the reinforcement to the balanced reinforcement ratio (ρ_f/ρ_{fb}), length to height ratio (L/H) and supporting conditions (simply supported and continuously supported). The six simply supported slabs were divided into 3 sets of 2 specimens to compare (L/H) ratios equal to 9, 10 and 12, reinforced with (ρ_f/ρ_{fb}) ratio equal to 3.9 and 2.6. The two continuous slabs varied in (ρ_f/ρ_{fb}), with values equal to 5.1 and 3.2 for the reinforcement of the negative moment area, and 4.1 and 2.6 for the positive moment reinforcement, respectively.

The following can be concluded from the findings of this study:

1) The slabs were designed with (ρ_f/ρ_{fb}) > 1 to ensure that the failure doesn't occur by rupturing the BFRP reinforcement. As expected, none of the tested slabs failed by this mode of failure, instead, flexural shear failure governed.
2) The ultimate moment capacities predicted by ACI 440.1R (2006) for the slabs that experienced a flexural shear failure, were only 50-60% of the experimental capacities because of the conservative strength reduction factor used by the code (ϕ = 0.65). However, the nominal predicted capacities ranged between 75-90% of the experimental capacities. So it is safe to increase the strength reduction factor ϕ to 0.74 as recommended by Ovitigala and Issa (2012), who reported a similar range of 77-86% for the same comparison.
3) A decrease of 28-30% in the experimental deflection was observed when the area of BFRP reinforcement increased by 150%. Therefore, deflection requirements can be controlled by increasing the BFRP reinforcement area.

4) The experimental moment of inertia did not conform to any of the proposed models in the literature; its value was underestimated by all models especially after the applied moment exceeded 2.5 times the cracking moment. The slabs were over-reinforced whereas other models were considered under-reinforced sections.
5) Decreasing L/H ratio for the same reinforcement area proved to be very efficient in reducing deflection for simply supported BFRP reinforced slabs. Decreasing the span length by 25% decreased the deflection by 59-65%.
6) The results obtained by the finite element analysis for simply supported slabs were more accurate than those for continuous slabs, however both agreed with the experimental results. At ultimate loads, FE analysis was able to predict the deflection of the simply supported specimens within an accuracy of 88-97%, whereas this ratio drops to 79% for continuous slabs. At lower loads and up to 80% of the ultimate load, higher accuracy is achieved for continuous specimens and the maximum variation between the experimental and finite element deflection is 10%.
7) The future application of BFRP reinforced lightweight concrete bridge deck slabs supported on girders is feasible, especially that deflection in such type of bridges is not an issue when the deck is continuously supported over multiple girders.

REFERENCES

1- AASHTO LRFD, 2004, Bridge design specifications and commentary, 3rd Ed., Washington, D.C.

2- ACI Committee 318, 2011, "Building Code Requirements for Structural Concrete and Commentary", American Concrete Institute, Farmington Hills, Michigan

3- ACI Committee 440, Guide for the Design and Construction of Structural Concrete Reinforced with FRP Bars, 440.1R-06 A., American Concrete Institute, USA. 2006.

4- ACI Committee 440, Guide for the Design and Construction of Externally Bonded FRP Systems for Strengthening Concrete Structures, ACI 440.2R-08, American Concrete Institute, USA. 2008.

5- Adhikari, S., 2009, "Mechanical Properties and Flexural Applications of Basalt Fiber Reinforced Polymer (BFRP) Bars", MS thesis, Department of Civil Engineering, University of Akron, Ohio, USA.

6- Alsayed, S.H., Al-Salloum, Y.A., and Almusallam, T.H., 2000, "Performance of glass fiber reinforced plastic bars as a reinforcing material for concrete structures", Composites: Part B-engineering, Elsevier, V. 31, pp.555-567.

7- ANSYS User's Manual (Release 11.0 Documentation), ANSYS, Inc., Canonsburg, Pennsylvania, USA

8- ASTM Standard C39, 2014a, "Standard Test Method for Compressive Strength of Cylindrical Concrete Specimens", ASTM International, West Conshohocken, PA, 2014, DOI:10.1520/C0039_C0039M-14A., www.astm.org.ASTM

9- ASTM Standard C78, 2010, “Standard Test Method for Flexural Strength of Concrete (Using Simple Beam with Third-Point Loading)", ASTM International, West Conshohocken, PA, 2010, DOI:10.1520/C0078_C0078M-10., www.astm.org.

10- ASTM Standard C469, 2014, “Standard Test Method for Static Modulus of Elasticity and Poisson’s Ratio of Concrete in Compression", ASTM International, West Conshohocken, PA, 2014, DOI:10.1520/C0469_C0469M-14., www.astm.org.

11- ASTM Standard C496, 2011, “Standard Test Method for Splitting Tensile Strength of Cylindrical Concrete Specimens", ASTM International, West Conshohocken, PA, 2011, DOI:10.1520/C0469_C0469M-11., www.astm.org.

12- Bakis, C. E.; Freimanis, A. J.; Gremel, D.; and Nanni, A.,1998b, “Effect of Resin Material on Bond and Tensile Properties of Unconditioned and Conditioned FRP Reinforcement Rods,” *Proceedings of the First International Conference on Durability of Composites for Construction*, B. Benmokrane and H. Rahman, eds., Sherbrooke, Quebec, pp. 525-535.

13- Bischoff, P.H., 2005, “Re-evaluation of deflection prediction for concrete beams reinforced with steel and fiber reinforced polymer bars”, Journal of Structural Engineering, ASCE, V.131, No.5, pp.752-767.

14- Bischoff, P. H., 2007, “Rational Model for Calculating Deflection of Reinforced Concrete Beams and Slabs,” Canadian Journal of Civil Engineering, V. 34, No. 8, pp. 992-1002.

15- B.J. Si1, Z.G. Sun2, Q.H. Ai3, D.S. Wang4 and Q.X. Wang, “Experiments and simulation of flexural-shear dominated RC bridge piers under reversed cyclic

loading". The 14th World Conference on Earthquake Engineering October 12-17, 2008, Beijing, China

16- Calculated by Earth Policy Institute from United States Geological Survey, Mineral Commodity Summaries 2005 (Washington, DC: U.S. Government Printing Office, 2005).

17- C. Fang, K. Lundgren, L. Chen, C. Zhu, Corrosion influence on bond in reinforced concrete, Cem Concr Res, 34 (2004), pp. 2159‑2167

18- Daniel, Isaac M., and Ishai, Ori. , Engineering Mechanics of Composite Materials. New York: Oxford University Press, 1994. Print.

19- Epoxy-coated-rebar debate still going, Civil Engineering; Mar 1993; 63, 3; ABI/INFORM Global, pg. 22

20- J.G. Cabrera, Deterioration of concrete due to reinforcement steel corrosion, Cem Concr Compos, 18 (1996), pp. 47–59

21- Kaw, Autar K., Mechanics of Composite Materials. Florida: Taylor&Francis, 2006. Print.

22- Lim, H. S., Wee, T. H., Mansur, M. A ., and Kong, K. H., September 2006, "Flexural Behavior of Reinforced Lightweight Aggregate Concrete Beams," Proceedings of the 6th Asia-Pacific Structural Engineering and Construction Conference (APSEC 2006), Kuala Lumpur, Malaysia.

23- Lopresto V, Leone C, De Iorio I, Mechanical characterization of basalt fibre reinforced plastic, Composites Part B 42, 717–723 (2011)

24- L.C.Bank, Jhon Willey and son, 2006, Structural design with FRP materials, Composite for Construction.

25- Mallick, P. K., 1988, Fiber Reinforced Composites, Materials, Manufacturing, and Design, Marcell Dekker, Inc., New York, 469 pp.

26- National Transportation Safety Board, 2008, Collapse of I-35W Highway Bridge, Minneapolis, Minnesota, August 1, 2007. Highway Accident Report NTSB/HAR-08/03. Washington, DC. (http://www.dot.state.mn.us/i35wbridge/ntsb/finalreport.pdf)

27- National Association of Corrosion Engineers, 2002, The United States Cost of Corrosion Study (http://www.nace.org/uploadedFiles/Publications/cost_corrosion.ppt)

28- Nanni, A., and Dolan, C. W., eds., 1993, "Fiber-Reinforced- Plastic Reinforcement for Concrete Structures", International Symposium, SP-138, ACI, Farmington Hills, Michigan, pp.977

29- Ovitigala, T., Issa, M., 2012, "Flexural Behavior of Concrete Beams Reinforced with Basalt Fiber Reinforcement Polymer (BFRP) Bars

30- Patnaik A. , Applications of Basalt Fiber Reinforced Polymer (BFRP) Reinforcement for Transportation Infrastructure, Developing a Research Agenda for Transportation Infrastructure - TRB November 2009

31- Sim, J., Park, C., and Moon, D.Y., 2005, "Characteristics of basalt fiber as a strengthening material for concrete structures", Composites Part B-Engineering, V.36, pp.504-512

32- Wu, W. P., 1990, "Thermomechanical Properties of Fiber Reinforced Plastic (FRP) Bars," PhD dissertation, West Virginia University, Morgantown, W.Va., 292 pp.

33- Zhou S, Rizos D C and Petrou M F (2004), "Effects of Superstructure Flexibility on Strength of Reinforced Concrete Bridge Decks,"*Computers & Structures*, 82(1), pp. 13-23.

VITA
Fadi Alsharif

CAREER OBJECTIVE

To obtain a Structural Engineering position enabling me to utilize and expand on my education and experience

EDUCATION

- Master of Science in Structural Engineering, University of Illinois at Chicago, Expected August 2014. GPA 4.0/4.0

- Bachelor of Science in Civil Engineering (Major in Structural Engineering), University of Jordan, 2007. GPA of 3.32/4.0

PROFESSIONAL EXPERIENCE

HBM Engineering Group — Feb. 2014 - Present
Intern Engineer

- Support engineers in providing structural analysis and design, field inspection and CADD work.

University of Illinois at Chicago — Aug. 2013 - May 2014
Research Assistant at Civil Engineering Department

- Structural Behavior of Lightweight Concrete Bridge Deck Slabs Reinforced with Basalt FRP Bars

Teaching Assistant at Civil Engineering Department

- Advanced Design of Reinforced Concrete Structures (Fall 2013)
- Design of Reinforced Concrete Structures (Spring 2014)

Chicago Bridge and Iron (CBI)
Project Engineer — **2008 - 2012**

  - ***Water Storage Tanks, Thermal Energy Storage Tanks***
  - ***Diesel Storage Tanks, Misc. Atmospheric Tanks & Low Pressure Degassing Tanks, Dome Roof Tanks***
  - ***Double Wall Cryogenic Liquid Storage Tanks, Floating Roof Tanks, Nitrogen Breather Hemisphere Tanks***
  - ***Large Bore Pipes with Fittings***
- Assisted in monitoring and driving projects' progress
- Participated in developing and influencing the project strategy to improve project economics, schedule, safety and quality
- Monitored resources: equipment, materials, and personnel
- Supervised engineers and laborers during fabrication, inspection, supply and delivery to construction sites
- Ensured timely resolution to technical, quality, cost and schedules
- Prepared as-built drawings at the end of project
- Developed project-specific procedures for the assigned projects
- Maintained contractual variations during projects are maintained to support subsequent commercial claims
- Evaluated, organized, and prioritized work scopes and the overall project schedules
- Liaised and managed third party contractors' schedules and scope of works

2K Engineering Bureau **2007 - 2008**
Jr. Structural Engineer

- Assisted in providing software analysis and structural design of various concrete buildings
- Assisted in preparing structural details in AutoCAD

LICENSURE

Pursuing engineering licenses (FE & PE)

SKILLS

- MicroStation
- AutoCAD 2D, Microsoft Office Suite

AFFILIATIONS

- American Society of Civil Engineers – ASCE
- Arab American Association of Engineers and Architects – AAAEA

REFERENCES

Available upon request